On the uses of Atmospheric and Laser Plasmas for Biomedical Applications

A thesis submitted for the degree of

Doctor of Philosophy

Presented to:

The School of Physical Sciences, Faculty of Science and Health,

Dublin City University

Author:

James Connolly B.Sc.

Supervisor:

Dr. Jean-Paul Mosnier

December 2012

Declaration:

I hereby certify that this material, which I now submit for assessment on the programme of study leading to the award for Doctorate of Philosophy is entirely my own work that I have exercised reasonable care to ensure that the work is original, and does not to the best of my knowledge breach any law of copyright, and has not been taken from the work of others save and to the extent such that such work has been cited and acknowledged within the text of my work.

Signed:___________________

ID Number: 54466268

Date:________ /_____ /_____

Acknowledgements:

This thesis represents the culmination of work over several years. It has been a long road to get here, and there have been a few bumps along the way but, as journeys go, it's not one that I've minded taking at all. Credit for that lies with many other people who have supported me, materially and emotionally, in order that I could spend all my time tinkering with vacuum chambers and eccentric lasers. First and foremost, I owe a debt of thanks to my supervisor, Dr. Jean-Paul Mosnier for giving me the opportunity in the first place. He has also been free with advice and support. I would also like to express my gratitude to all the faculty of the DCU Physics department, who have always been a source of support and encouragement, and to my post docs, who have taken a lot of time from their own work to help me with mine.

I would like to express my thanks to those people with whom I started as an undergrad in DCU eight years ago and who have been with me the whole way, especially Éanna, with whom I have worked more closely for the last four years, the number of times we had to spend hours trying to adjust optics, fish fallen samples from the bottom of the chamber or repair an old pump; it has been a lot of fun and I wouldn't give up any of it. I would also like to thank all my fellow postgrads past and present; it has been a pleasure working beside all of you. I must also express gratitude to Pat Wogan, Des Lavelle, Ray Murphy, Lisa Peyton and Alan Hughes. It wouldn't be possible to do any of the research we do without them supporting us.

Finally, I want to thank my family for the support I have been given by them, mostly material but frequently a friendly ear and a kind word when I was discouraged by this or that. Mum and Dad; who cared enough to make sure I worked in school and drove me to music lessons. I couldn't have done it without you.

Contents:

Table of Figures:

AFM:	Atomic Force Microscopy
ALD:	Atomic LAyer Deposition
C_d:	Dielectric Capacitance
C_g:	Gas Capaciance
C_{tot}:	Total Capacitance
CVD:	Chemical Vapour Deposition
DBD:	Dielectric Barrier Discharge
EAB:	Elecroactive Biofilm
EET:	Extracellular Electron Transfer
ITO:	Indium Tin Oxide
K:	Kelvin
MFC:	Microbial Fuel Cell
mm:	millimetre
mTorr:	milliTorr
nm:	nanometre
PEM:	Proton Exchange Membrane
PET:	Poly (ethylene teaphthalate)
PLD:	Pulsed Laser Deposition
SEC:	Spectroelectrochemistry
SEM:	Scanning Electron Microscopy
TCO:	Transparent Conducting Oxide
U_d:	Discharge Voltage
U_{Max}:	Maximum Voltage
U_{Min}:	Breakdown Voltage
W:	Watt
XRD:	X-ray Diffraction
ZnO:	Zinc Oxide

Abstract:

This thesis describes work with different types of low temperature plasmas and their use in microbiological applications. Herein is described the development and results from a novel system for decontamination of packaged produce using a dielectric barrier discharge. It also describes the results of growth by pulsed laser deposition of nominally undoped and doped zinc oxide thin films at low temperature on plastic substrates. This work was carried out to develop transparent conducting electrodes for the growth of electroactive biofilms for microbial fuel cells.

The system described herein utilises a floating high voltage (±15 kV) that sustains an atmospheric plasma in a plastic bag between parallel plate electrodes. This is characterised using current, voltage and charge measurement and also emission spectroscopy over electrode separations from 30 to 100 mm. Results are analysed to unravel physical processes present in this plasma for optimisation as a method of food decontamination. Plasma parameters are measured by the interpretation of electrical measurements by the "capacitor-in-series" model. The power consumed by the discharge and the reduced field strength decrease quadratically from 12.0W to 4.5W and linearly from 140 Td to 50 Td, respectively, in this range. Spectroscopy reveals the presence of molecular nitrogen, oxygen, NO, OH and helium. Temperature estimates are made by comparing intensity calibrated spectra with plots generated by the SPECAIR program. At 40 mm, this comparison yielded electron, vibrational and translational (gas) temperatures of (4980 ± 100) K, (2700 ± 200) K and (300 ± 100) K, respectively. In conjunction with colleagues from the DIT School of Food Science and Environmental Health, the bacterial inactivation properties of the system were examined. A 1.5 log reduction in bacterial populations was achieved through indirect exposure to the plasma over a 5 minute treatment.

This work also presents the results of characterisation of zinc oxide and ZnO:Al (2%) thin films deposited at pressures of 1 to 300 mTorr in oxygen using several investigative techniques (AFM, XRD, contact profilometry, Van der Pauw and water contact angle). These investigate the effects of growth parameters on physical and electrical properties of thin films grown on amorphous substrates at low temperatures as a function of growth pressure, thickness and target doping. Films grown at 5,000 to 20,000 shots vary in thickness from 125 nm to 500 nm. Resistivity ranges from 10^{-2} to 10^{7} Ω cm, with low pressure films exhibiting the lowest resistivities. Crystal structure becomes apparent above 1 µm, the majority of films, which have thicknesses of 500 nm or less, exhibit no crystallinity. Water contact angle decreases with increasing deposition pressure. In conjunction with colleagues from the DCU School of Biotechnology, electroactive biofilms were grown on the thin films and their electrical behaviour measured with chronoamperometry and cyclic voltammetry.

The results outlined herein show the viability of non-equilibrium low temperature atmospheric plasma to decontaminate food inside a pre-sealed package, which is of use in the food industry. The results also show that zinc oxide thin films have potential as transparent conducting substrates for the growth of electroactive biofilms for use in microbial fuel cells.

List of Publications:

James Connolly, Dr. Anand Jain, Gabriele Pastorella, Satheesh Krishnamurthy, John-Paul Mosnier, Enrico Marsili, “Zinc oxide and indium tin oxide thin films for the growth and characterization of Shewanella loihica PV-4 electroactive biofilms” *Virulence*, 2, 479-482 (2011)

Dr. Anand Jain, Xiaoming Zhang, Gabriele Pastorella, James Connolly, Niamh Barry, Robert Woolley, Satheesh Krishnamurthy, Enrico Marsili, “Electron transfer mechanism in Shewanella loihica PV-4 biofilms formed at graphite electrode”, *Bioelectrochemistry*, 87, 28-32 (2012)

M Novotný, J Čížek, R Kužel, J Bulíř, J Lančok, J Connolly, E McCarthy, S Krishnamurthy, J-P Mosnier, W Anwand and G Brauer, Structural characterization of ZnO thin films grown on various substrates by pulsed laser deposition, *J. Phys. D: Appl Phys,* 45, (2012) doi: 10.1088/0022-3727/45/22/225101

J Connolly, V P Valdramidis, E Byrne, K A Karatzas, P J Cullen, K M Keener and J-P Mosnier, Characterization and antimicrobial efficacy against *E. coli* of a helium/air plasma at atmospheric pressure created in a plastic package, *J. Phys. D: Appl. Phys*., 46 (2013) 035401

Chapter I : Introduction and Motivation

I.1 Plasma Decontamination:

The disinfection of fresh produce is of great importance. Chlorine wash is the most widely used industrial washing method in the produce industry, due to its availability, low cost and ease of operation. Nevertheless, its efficacy has been questioned or appeared to be limited in some scientific studies. (Beuchet 1999, Hegenbart 2002, Li, et al. 2001, Zhang and Farber 1996) The use of chlorine has also been associated with health and environmental concerns due to the generation of chlorinated by-products with some carcinogenic properties, such as chloroform and trihalomethane (THM) when precursor organic compounds, such as humic and fulvic acids are present (Menzer and Nelson 2001, Richardson, et al. 1998). At the 33rd Codex Committee on Food Additives and Contaminants (CCFAC (2001)) the question of the safety of disinfection with chlorine compound was raised, while in some EU countries (Germany, the Netherlands, Switzerland and Belgium to name a few) its use is already prohibited on minimally processed foods (Carlin and Nguyen-the 1999). Alternative disinfection approaches investigated to date include chlorine dioxide organic acids, electrolyzed water, UV-C radiation, intense light pulses, hydrogen peroxide, indirect ozone, natural antimicrobials, electron beam processing, blanching with heat shock and calcium based treatments (Rico, et al. 2007, Artés, et al. 2009, Grasso, Uribe-Rendon and Lee 2011, Issa-Zacharia, et al. 2011). Each of these has advantages and disadvantages; chlorine dioxide (ClO_2) is a strong oxidant, less corrosive and toxic than chlorine, with a broad and high biocidal effectiveness. Another example is UV-C disinfection, which appears to be effective in reducing deterioration of produce by effectively reducing microbial populations (Allende and Artés 2003, Salinero, et al. 1998). However, it was found to increase the stress of the produce, respiration rate, and possibly induce a lignification-like process, changing the appearance of the product. These effects, and concerns about health risks associated with exposure to corrosive chemicals and ionising radiation spur the development of novel treatment methods.

Non-thermal atmospheric plasmas offer the potential of such a novel form of bacterial inactivation, demonstrated as early as 1996 by Laroussi (2002). These cold plasmas can be formed in a dielectric barrier discharge (DBD) at atmospheric pressure and have found applications in various fields (Kogelschatz and Eliasson 1999). In DBDs in particular, the formation of ozone is a feature (Kogelschatz and Eliasson 1988) and has been exploited by several authors for decontamination of various species contained inside sealed packages inflated with a gas in which a plasma is then generated (Lee, Yi, et al. 2001, Leipold, et al. 2011, Keener, et al. 2011). Several designs of system for generating DBDs are described in the literature; needle-electrode (pencil) (Laroussi, Tendero, et al. 2006, Moon and Choe 2003) or parallel-plate (Nesrsisyan and Graham 2004, Chiper, Chen, et al. 2011, Keener, et al. 2011, Eliasson, Kogelschatz and Hirth 1987) (Lee, Yi, et al. 2001). Experimental parameters (electrode separation, voltage and frequency) vary between systems; for the apparatus described in the papers cited above, values for electrode separation are typically a few mm, typical frequency values range from several kHz up to 1 MHz and typical voltages are in the kV range. Plasma inactivation techniques offer a number of advantages:

- They can be performed at atmospheric pressure.
- They do not require high temperatures, unlike autoclaving.
- They do not require harmful/corrosive substances, such as chlorine or ionising radiation.
- They have fewer adverse after effects on plastic, compared to corrosive chemicals or ionising radiation. This is important when the majority of medical equipment housings are plastic.
- They can be performed in a short amount of time and are cost effective.

However, there is uncertainty as to the mechanism responsible for decontamination. Several biocidal mechanisms have been proposed;

- The generation of ozone/radicals: When molecular oxygen is exposed to atmospheric plasma, it is broken apart into individual atoms that combine into ozone (O_3) as well as radicals such as OH and NO. When a liberated electron (e) strikes an O_2 molecule, the following reaction takes place (Poiata, et al. 2010):

$$e + O_2 \rightarrow e + e + O^{+} + O$$

The oxygen atoms can then combine to form ozone in the following manner:

$$O + O_2 + M \rightarrow O_3 + M$$

where M is an O atom, O_2 or O_3 molecule. A similar reaction involving nitrogen also generates excited species:

$$\begin{aligned} &N_2 + e \rightarrow N_2^* + e \\ &N_2^* + O_2 \rightarrow N_2 + 2O \\ &N_2^* + O_2 \rightarrow N_2O + O \end{aligned}$$

These are highly oxidising and according to Kahdre, Yousef and Kim (2006) "ozone attacks numerous cellular constituents, including proteins, unsaturated lipids and respiratory enzymes". When the cell is in contact with many ozone molecules, the damage soon becomes catastrophic; without the cell wall, the bacterium dies.

- Ultraviolet light: Helium and argon plasmas exhibit strong emission in the UV range of the electromagnetic spectrum. Ultraviolet light is composed of high energy, short wavelength photons, which can penetrate a cell and disrupt the chemical bonds in the cell DNA (Lorenzo-Lorenzo, et al. 1993). UV wavelengths less than 275 nm have sufficient energy to break the C-C or C-H bonds. Prolonged exposure to UV light does irreparable harm to the cell, which dies eventually.

- Charged particles/electrostatic forces: When a charged particle contacts the cell wall, it can bind with it, weakening the wall. Multiple such bindings will destroy the cell. It has been hypothesised that electrostatic forces can also damage the cell by overcoming the tensile strength of the cell wall, literally ripping it apart (M. Kong 2003).
- Etching: As microorganisms adsorb reactive species from the plasma, these species react chemically with the cell wall, which will release small molecules (such as CO_2 and H_2O) and undermine the structure of the wall. Over time the cell wall will degrade and the microorganism will die (Moisan, et al. 2002).

The role each mechanism plays, and to what extent, is currently under investigation. It is generally believed that a combination of these factors is responsible for the decontaminating effect. One major factor that governs which mechanisms are in play is the placement of the sample inside the plasma apparatus. Reports in the literature feature experiments in which the sample is placed directly in the path of the plasma, (Stoffels, Sakiyama and Graves 2008) where it will be exposed to UV and electrostatic forces in addition to excited oxygen species, and experiments where the plasma is not exposed to the plasma directly, but to the excited species only (Cvelbar, et al. 2009).

Plasma decontamination apparatus have several configurations, from large parallel plates that can generate large volumes of ionised gas to annular tube electrodes that emit a "jet" that can be precisely manipulated. Each has particular characteristics and applications. An intriguing idea is the treatment of pre-packaged produce while in a sealed bag. This would be advantageous in an industrial context, by sterilising produce once it has been sealed inside an airtight package; opportunity for re-contamination is eliminated. DBDs for decontamination in sealed packages is becoming the focus of research literature (Leipold, et al. 2011, Schwabedissen, et al. 2007, Chiper, Chen, et al. 2011), therefore this is an area that is ripe for investigation. The aims of this part of our research are:

- Construct a "proof of concept" apparatus for in-package decontamination, utilising existing "off the shelf" components.
- Characterise the DBD plasma using optical and electrical techniques.
- Investigate the effectiveness of the plasma for inactivation of microorganisms.
- From the above, possibly investigate and identify the main mechanism(s) of inactivation.

I.2 Microbial Fuel Cell:

The earliest demonstration of the microbial fuel cell (MFC) was by M.C. Potter in 1911 (Potter 1911), who observed a culture of *Saccharomyces cerevisiae* immersed in an unspecified nutrient solution, and reported that an electro-motive force was produced. In the same paper, Potter also reported on similar experiment undertaken with yeast in a sugar solution. In these experiments, the peak voltage recorded was approximately 0.4 V. Voltage would quickly (≈10 minutes) climb to this maximum value, and then fall off over the following 30-50 minutes.

Low voltage output meant that MFCs were not practical for electricity generation, and so were not the subject of widespread research. In the 1980s, it was discovered that electron mediators, when added to the nutrient solution, facilitated the electron transfer, increasing current output (Davis and Higson 2007). However, many mediators are synthetic compounds and are both toxic and unstable, limiting their usefulness.

Kim et al (1999) and Chaudhuri & Lovley (2003) observed microbes that transfer electrons to the anode directly with high columbic efficiency, without the need for a mediator. Amongst these bacteria is *Geobacter Sulfurreducens*, one of the strains used in our experiments.

A typical microbial fuel cell is illustrated in figure 1. It consists of an anode and cathode separated by a proton exchange membrane (PEM). Through a process of oxidation, a layer of microbes on the cathode, called an electroactive biofilm (EAB) convert the nutrient suspension in which they are immersed into electrons and protons, as well as CO_2. Since CO_2 is absorbed during photosynthesis by the renewable biomass, net CO_2 output is zero. Electrons are absorbed by the cathode and are transported, via an external circuit, to the anode. Protons pass through the PEM and combine with oxygen forming water. An electric current is generated because the microbes are isolated from any end terminal electron acceptor other than the cathode; there is no place for the electrons to go except into the external circuit as current. A typical reaction is the following (Du, Li and Gu 2007):

Cathodic Reaction: $CH_3COO^- + 2H_2O \rightarrow 2CO_2 + 7H^+ + 8e^-$

Anodic Reaction: $O_2 + 4e^- + 4H^+ \rightarrow 2H_2O$

Energy is converted directly from chemical to electrical, without an interim conversion to thermal, so an MFC can theoretically be very efficient. Efficiencies of greater than 70% have been reported (Chaudhuri and Lovley 2003, Rabaey, et al. 2003). However, the absolute amount of electricity generated by each cell is very small, on the order of mA of current. For the foreseeable future, MFCs are unsuited to large scale electricity generation. However, there are a number of applications where a low maintenance, low output power source would be ideal, for example, in remote sensors (Donovan, et al. 2008).

Since they can use many human waste products as their nutrient source, MFCs can be used to treat waste water. The electricity they generate can contribute towards the treatment process, potentially providing half the electricity required (Du, Li and Gu 2007). Waste water treated with MFCs also has between 50-90% fewer solids compared with conventional treatment methods (Holzman 2005).

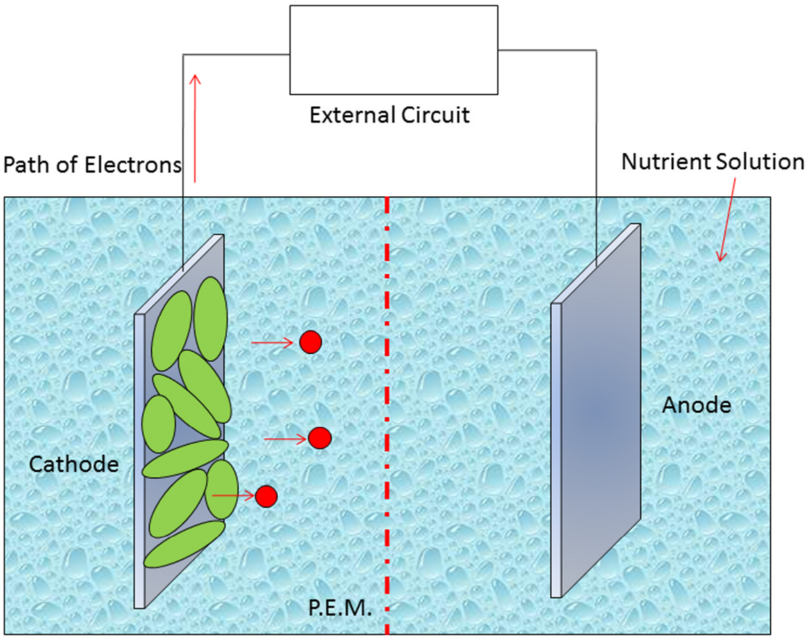

Figure 1: Diagram of principle of microbial fuel cell

A key factor in the design of an efficient MFC is the cathode; it must offer a surface to which bacteria will adhere easily and which can conduct the electrons they produce to an external circuit. Several materials are used as MFC cathodes, including carbon in the form of paper or cloth and graphite as a weave, as granules or as brushes (Logan 2008). In many cases, these carbon electrodes are infused with platinum as a catalyst (Logan 2008). It is important, when optimising the design of MFCs, to be able to quantify the characteristics of the microbial film. This can be done with biological and electrochemical methods, however biological methods give no insight into the biophysical properties of the biomolecules that are involved in the extracellular electron transfer (EET) process and electrochemistry is not sufficient to investigate the complex activity of the EAB/electrode interface (Jain, Gazzola, et al. 2011). Combining spectroscopy with direct electrochemistry, termed spectroelectrochemistry (SEC), overcomes these limitations. SEC has seen use in organic chemistry for several years (Borloo, et al. 2007, Bancroft, Sidwell and Blount 1981).

However, since SEC involves measuring the absorption of light as it passes through the biofilm, electrode material must be optically transparent, making materials such as carbon and graphite unsuitable. For this reason, transition metal oxides have been utilised to grow thin film electrodes with the necessary characteristics. Indium tin oxide (ITO) has proven extremely suitable for this application.

Zinc oxide (ZnO) is a material with interesting and useful properties. While it is already used in bulk form in various applications (in medications, as a food additive, and as a pigment), its semiconductor properties, particularly is wide, direct band gap, are recognised as useful in the development of short wavelength optoelectronic devices. ZnO is an n-type semiconductor with a direct band gap of ≈3.3 eV at 300 K. It has a hexagonal wurtzite crystal structure and is part of the II – VI semiconductor group (its component elements zinc and oxygen belong to the second and sixth groups of the periodic table). The crystal structure of zinc oxide is illustrated in figure 2.

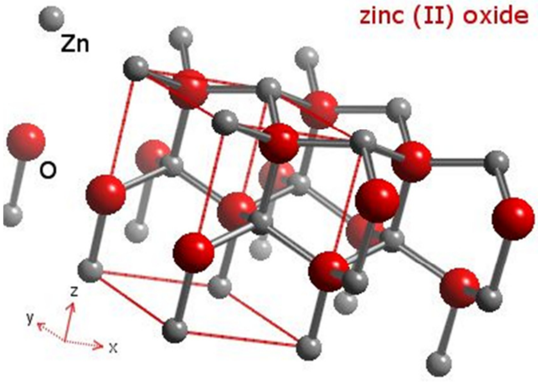

Figure 2: Crystalline structure of zinc oxide **(Winter 2012)**

Each oxygen atom is surrounded by four zinc atoms in the shape of a tetrahedron (one at each end of an imaginary triangular pyramid) that are, in turn, also surrounded by four oxygen atoms. A band gap of 3.3 eV corresponds to an emission wavelength of 370 nm, slightly below the upper limit of UV light (380 nm). This makes ZnO an ideal candidate for the fabrication of UV wavelength LEDs, laser diodes and photodiodes. This has spurred research into the development of ZnO thin films using several deposition methods. Pil *et al* investigated aluminium doped ZnO thin films formed by pulsed laser deposition (PLD) on fused quartz, polyethylene terephthalate (PET) and polyester (PES) substrates, using X-ray diffraction (XRD), scanning electron microscopy (SEM), atomic force microscopy (AFM), X-ray photoelectron spectroscopy (XPS) and other measurements (Kim, et al. 2008). They concluded that the thin film transmitted 90% of the incident light, and measured resistivity values on the order of $1\times10^{-4}\ \Omega\ cm$. Comparable results for electrical resistivity and crystallinity as measured by XRD were reported by Yamada *et al* for thin ZnO films grown on Corning glass using a modified chemical vapour deposition (CVD) technique known as atomic layer deposition (ALD) (Yamada, Sang and Konagi 1997). ALD was also the focus of experiments by Kim *et al*; comparing the characteristics of ZnO films when deposited by thermal ALD and plasma enhanced ALD on silicon and Corning glass (2011). Clearly, there is a great deal of interest in the characteristics of ZnO films, what should be noted is the developing interest in thin films grown on amorphous substrates (glass, PET, PES), fuelled by a need to develop transparent conducting films for flat panel and flexible displays. Use of these materials places limitations on certain growth conditions, most notably temperature, since many plastics will lost their structural properties at temperatures far in excess of 100^{o}C. This presents a challenge, since higher growth temperatures should improve material properties in general. However, it is possible to gain improvement through the use of doping and other innovative methods (Kim, Piqué, et al. 2000).

ZnO possesses certain other useful qualities. It has been used for many years in medicine; because of its antibacterial and astringent properties, it is used as a topical treatment for mild skin conditions (eczema, sunburn rashes etc.). Because of its optical properties, it is used as the active UV absorbing agent in sun creams. When used in this fashion, ZnO is not absorbed into the skin, and is therefore non-allergenic. ZnO is also added to processed foods as a nutrient, and can be consumed safely in small quantities. For these reasons, ZnO has potential as a substitute for ITO as a transparent conducting oxide. One of its primary advantages is the ability to create optically transparent, electrically conductive films through PLD. This would allow films to be created that would be ideal for serving as a cathode in an MFC, and enable SEC characterisation to be carried out. Several parameters can be controlled during PLD, allowing the characteristics of the film to be altered in several ways. This allows the ZnO thin film to be optimised to ensure the best performance from the MFC.

The focus of this work is the growth of doped and undoped zinc oxide thin films using PLD and their optimisation for use as a transparent electrode in microbial fuel cells. The aims of this part of our research were to:

- Grow high quality doped and undoped zinc oxide thin films
- Grow said films on amorphous substrates, notably plastics such as Perspex and Kapton.
- Characterise said films using a wide array of investigative techniques such as AFM, XRD, Van der Pauw and water contact angle.
- Through collaboration with colleagues in the DCU School of biotechnology, grow electroactive biofilms on ZnO thin films and compare their electrical output with commercially available ITO films which represent the “state of the art”.

I.3 PLD on Plastic:

There has recently been a great deal of interest in the development of the next generation of flat video display. Improving performance, lowering power consumption and creating screens that are ever more portable is of paramount concern. One area of development receiving widespread attention is in the manufacture of the first generation of flexible screens (Crawford 2005). Light weight and durable, these promise a whole new level of possibility in many applications.

Central to the design of flexible electronics is layering electronic circuits on a flexible substrate. The key to such developments lies in the availability of transparent conducting oxides (TCO). These are already utilised fabricating flat panel displays and solar panels and have suitable optical and electrical characteristics to develop new energy efficient displays.

The suitability of these substances to various forms of growth and deposition also promise new possibilities realized through a “bottom up” method of manufacture, where components can be grown directly on the substrate. There have been several works published that use PLD to deposit oxide films on flexible substrates (Kim, et al. 2001, Nomura, et al. 2004, Izumi, et al. 2002). The focus of this work is the growth and characterisation on Perspex and Kapton substrates of pure and doped zinc oxide thin films under a variety of pressures, temperatures and to a range of film thicknesses and the characterisation of said films using Van der Pauw electrical resistance measurement, AFM and XRD.

Chapter II: Plasma Parameters and diagnostic Methods:

II.1: Essential Plasma Features

Plasma is a collection of ionised particles that react strongly and collectively to electromagnetic fields. As energy is added to a gas, electrons are liberated from atoms. When enough atoms are ionised, the "sea" of electrons allows for electrical characteristics distinct from a neutral gas[1]. For this reason, plasma is often referred to as "the fourth state of matter". It is essentially a volume of gas which exhibits such a degree of ionisation that its dynamics are dominated by electromagnetic forces (Boyd and Sanderson 2003).

By both mass and volume, plasma is the most abundant state of matter in the universe. Stars are plasma and since our sun makes up over 99% of the visible mass of our solar system, it is reasonable to infer a similar proportion for other star systems. Even on Earth, there are several natural plasmas, including lightning and the polar aurorae, and of course man made plasmas which are common in many applications. In heavy industry, plasma torches are used in metal fabrication. Dielectric barrier discharge (DBD) plasma is used to generate ozone, for example to sterilise air in large scale ventilation systems (Kogelschatz 2003,). Even in leisure and entertainment, plasmas are becoming ubiquitous, since they are the mechanism by which an image is generated in a plasma screen display. The utility of plasma treatment of surfaces and plasma coating is perhaps only now becoming fully realised in areas related to biology and medicine. Breakthroughs are being made depositing biocompatible materials with plasma processes (Xie, et al. 2009, Cheruthazhekatt, et al. 2010, Weltmann, et al. 2010) allowing biocompatible coatings to be deposited on implants such as pacemakers, catheters or stents, improving adhesion or reducing the chances of rejection. Exposure to plasma is also being used to aid wound cleaning and healing (Cheruthazhekatt, et al. 2010, Fridman, et al. 2008). Plasma modified polymers may provide a method to allow the controlled release of drugs into a patient's bloodstream; the medication adheres to the modified surface and as the bindings slowly decay, is released to be absorbed by the body (Yooq, Kim and Park 2009).

---

[1] The term "plasma" was coined by the scientist Irving Langmuir, who was one of the first scientists to study plasmas, having begun to notice similarities in the structures of various mercury vapour discharges that he was observing. Langmuir believed, incorrectly, that the ionised particles would be constrained by some fluid-like medium, comparable to the clear fluid component of blood that is also called plasma.

II.1.a Debye Shielding/Plasma Sheath:

A phenomenon which differentiates the behaviour of plasma from a gas is its ability to remain in a neutrally charged state. The influence of the electrostatic field for a given particle does not extend over the volume of the plasma. Should an imbalance in charge occur, this fact combined with low electron mass ensures that a rapid flow of electrons will re-establish neutrality.

Consider a hypothetical plasma which is has a finite temperature, whose length in any direction is much greater than the inter-atomic distance and in which the electrons and ions are uniformly spaced and of equal density. If one were to insert a "test" particle with an electric charge into it, interaction of the ions and electrons with it would cause them to perturb; particles with similar charge will be repelled and, conversely, those with opposite charge will be attracted. The net result will be a "cloud" of particles of opposite charge surrounding the test particle, the potential of which will partially screen out the test charge potential. Figure 3 illustrates this shielding effect.

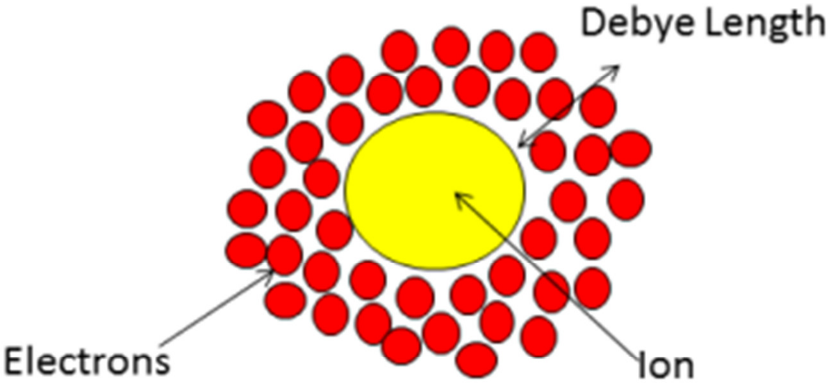

Figure 3 : Debye Shielding

The test particle's energy, kinetic and potential, is written as

$$w_r = \frac{mv^2}{2} + qV \qquad \textbf{(2. 1)}$$

where "q" is the charge on the particle. For an electron, q would equal to $-e$, an ion of charge Z would equal to $+Ze$. The Boltzmann factor would become

$$e^{-\left(\frac{mv^2}{2}+qV\right)\Big/k_BT} \tag{2. 2}$$

the probability of a particle having a given energy is dependent on its position, r. If the distribution function is integrated over the velocity space then

$$n \propto e^{-qV/T} \tag{2. 3}$$

inferring that particles will tend to coalesce around charges of opposite polarity, and will shield the charge from the electric field. The length of the Debye Screening effect can be calculated for an idealised system; it is assumed that ions carry a charge of Ze and that the ion and electron densities are $n_e = Zn_i \equiv n_\infty$. It is also assumed that $V=0$ when $r = \infty$. From the Boltzmann factor

$$n_e(x) = n_{e\infty} e^{eV/T_e} \tag{2. 4}$$

and

$$Zn_i(x) = n_{e\infty} e^{-eZ_iV/T_i} \tag{2. 5}$$

electrons and ions are in thermal equilibrium, but the electron temperature and ion temperature are not equal. This can be the case because electron-electron collisions and ion-ion collisions happen much faster than electron-ion collisions due to the discrepancy in their masses. The Poisson equation for this system is

$$\varepsilon_0 \frac{d^2V}{dr^2} = e(n_e - Zn_i) = en_\infty\left[e^{eV/T_e} - e^{-eZV/T_e}\right] \tag{2. 6}$$

In a region far from the electrode, where eV/T_e is small, the Poisson equation can be re-written as:

$$\varepsilon_0 \frac{d^2V}{dx^2} \approx en_{e\infty}\left(eV/T_e + eZV/T_i\right) \;\Rightarrow\; \frac{d^2V}{dx^2} \approx \frac{e^2 n_{e\infty}\left(1+ZT_e/T_i\right)}{\varepsilon_0 T_e}V \tag{2. 7}$$

The solution yields the characteristic exponential reduction rate

$$V \propto e^{(-r/\lambda_D)} \tag{2. 8}$$

where

$$\lambda_D = \left(\frac{\varepsilon_0 T_e}{n_e e^2 \left(1 + ZT_e/T_i\right)} \right) \tag{2. 9}$$

The term λ_D is the "Debye length"[2]. One of the two defining characteristics of plasma is the Debye length should be much smaller than the size of the plasma. The second is that there must be many particles within the "Debye sphere", an imaginary sphere with a radius of one Debye length (Goldston and Rutherford 1995). The number of particles within the Debye sphere can be calculated in the following manner.

$$N_D = n\frac{4}{3}\pi\lambda_D^3 \tag{2. 10}$$

In order for collective behaviour to be observed, $N_D >> 1$. (Chen 1984)

II.1.b Plasma Frequency:

The electrostatic forces that propel the electrons to maintain overall neutrality form oscillations about the equilibrium position. If a charge is inserted into the plasma, it will give rise to an electric field, to which electrons will react more quickly (due to their lesser mass). The potential energy will be transformed to kinetic energy that will drive the electrons beyond the equilibrium position. When this occurs, an electric field is again set up by the charge imbalance, retarding the motion of the electrons until all the kinetic energy is converted into potential energy. The electrons are now accelerated back towards the equilibrium position, in the opposite direction to the one in which they were previously travelling. These plasma oscillations occur at a characteristic frequency (the plasma frequency). Since the imbalance occurs over the Debye length, and since the electron thermal speed can be expressed as $(kT_e/m_e)^{1/2}$ the electron plasma frequency can be expressed as

---

[2] In honour of Dutch physicist Peter Debye

$$\omega_{pe} = \frac{\left(kT_e/m_e\right)^{1/2}}{\lambda_D} = \left(\frac{n_e e^2}{m_e \varepsilon_0}\right)^{1/2} \tag{2. 11}$$

Similarly, the ion plasma frequency is

$$\omega_{pe} = \left(\frac{n_e (Ze)^2}{m_i \varepsilon_0}\right)^{1/2} \tag{2. 12}$$

II.1.c Plasma Parameters:

Plasmas can be characterised by three main parameters:

- Various relevant temperatures (T_i, T_e, T_{rot}, T_{trans}).
- Particle densities (n_i, n_e).
- Steady-state magnetic field (B).

Each of these can vary by orders of magnitude, so plasmas exist in an enormous variety, from the "solar wind" of charged particles that emanates from our Sun (T≈10^5 K, n≈10^o cm^{-3}) to the ultra-dense and ultra-hot fusion plasma that are generated inside a Tokomak (T≈10^7 K, n≈10^{12} cm^{-3}) (Smirnov 2001).

Temperature is a measure of the range of velocities of the electrons, ions and neutral particles in the plasma, assuming that they adhere to the Maxwell-Boltzmann distribution of velocity:

$$E = \frac{3}{2} k_B T \tag{2. 13}$$

Although the SI unit of temperature is the Kelvin (K) used in equation (1.15), electron temperatures are often quoted in electronvolts (eV) (1 K = 8.617×10^{-5} eV). The electron temperature of a plasma is frequently much higher (by many orders of magnitude) than the ion temperature. This is due to their differing masses and thus, kinetic energies. Particle number density is the number of species (electrons, ions and neutrals) occupying a particular volume, measured in units of m^{-3}.

The steady state magnetic field is not a feature found in naturally occurring plasmas, since there is no externally imposed magnetic field, nor do they tend to generate large magnetic fields themselves. However the use of plasmas to generate useable energy by nuclear fusion requires external magnetic fields to confine and channel the plasma in a useful manner (Bellan 2006). Table 1 shows the parameters for a variety of naturally occurring and man-made plasmas and figure 4 shows various kinds of plasma as a function of temperature and particle density.

Table 1: Parameters of various plasmas

	Length (m)	**Density (m^{-3})**	**Electron Temp. (eV)**	**Magnetic Field (T)**
Interstellar Medium	10^{16}	10^{6}	1	10^{-1o}
Solar Wind	10^{1o}	10^{7}	10	10^{-8}
Van Allen Belts	10^{6}	10^{9}	10^{2}	10^{-6}
Earth's Ionosphere	10^{5}	10^{11}	10^{-1}	3×10^{-5}
Solar Corona	10^{8}	10^{13}	10^{2}	10^{-9}
Gas Discharges	10^{-2}	10^{18}	2	-
Fusion Experiment	1	$10^{19} – 10^{2o}$	$10^{3} – 10^{4}$	5
Fusion Reactor	2	10^{2o}	10^{4}	5

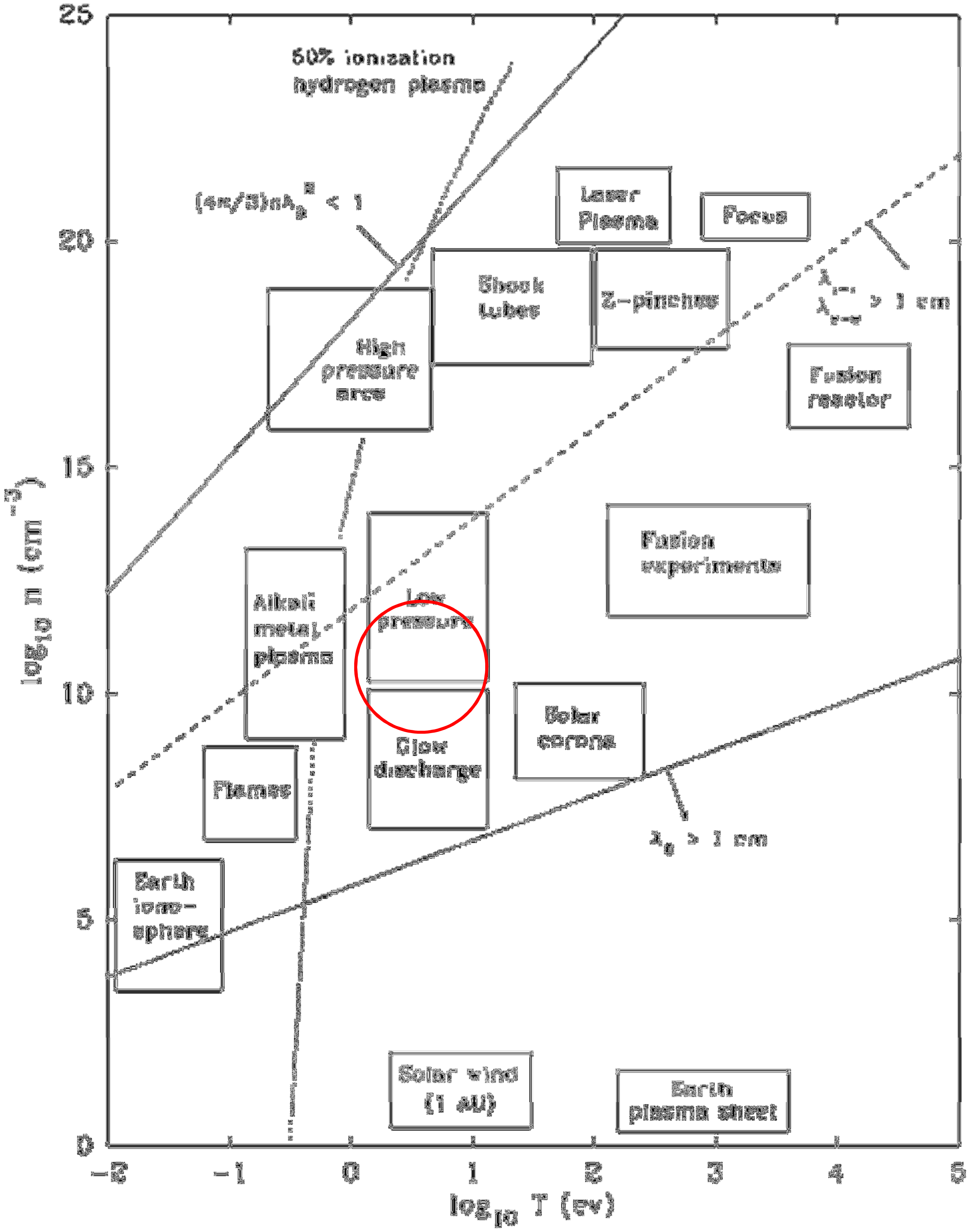

Figure 4: Log-log plot of Density vs Temperature showing various plamsa regimes (Huba 2011)

II.2 Plasma Types:

II.2.a Laser:

The ability of a laser beam to deliver a highly energised, tightly focussed pulse of energy to an area makes it ideal for the creation of highly controllable plasmas. By firing a pulse of laser light at a suitable target material, the material absorbs the photons, forming plasma. The resultant pressure gradient is such that the ionised material is propelled mechanically from the surface of the target (ablation). Laser plasmas have temperatures in the range $10^3 – 10^4$ K and particle densities of 10^{18} cm^{-3}. Laser plasmas have a variety of uses. Pulsed laser deposition (PLD) is an application that will be examined in more detail herein.

II.2.b Glow/Arc Discharge:

Discharge plasmas are common man made plasmas and were the subject of the initial investigations of scientists such as Crookes, who observed them in their vacuum tubes (1879). Although the equipment required to produce discharge plasma is quite straightforward to set up, the dynamics governing the formation and behaviour of the discharge is complex. There are several "regimes" in which a discharge can exist, distinguished by particular current and voltage characteristics. A useful method of classifying these regimes is by their voltage and current levels, illustrated in figure 5.

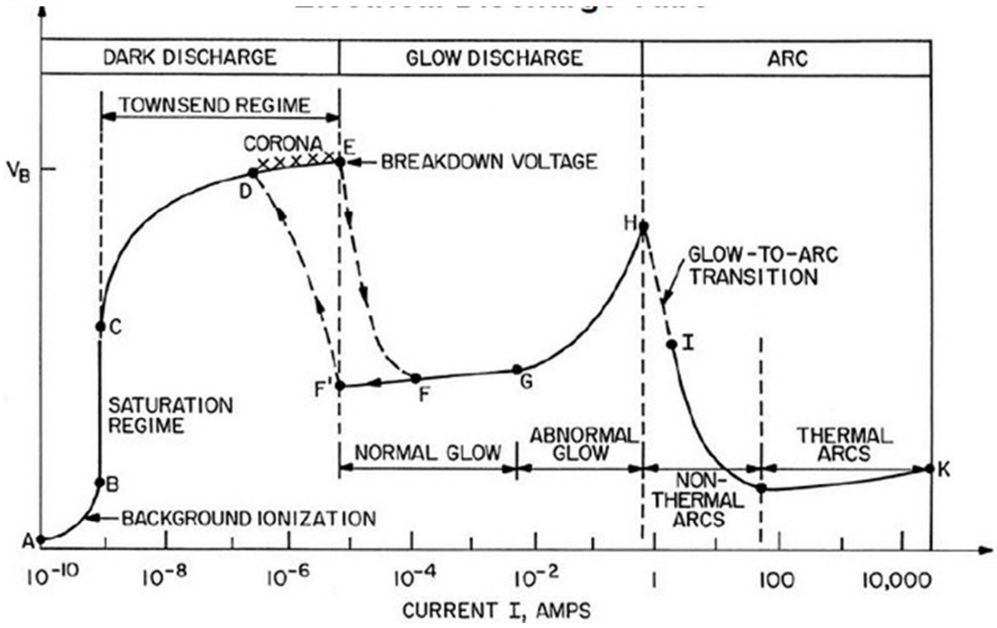

Figure 5: Voltage vs. Current for a discharge plasma (Roth 1995)

The discharge plasma that is the subject of this thesis exhibits complex behaviour, governed by a number of conditions. A comprehensive explanation of the formation of a discharge plasma can be found in the thesis of Niall O 'Connor (2011) . The situation that is considered is two parallel plates of area A, separated by a distance d which is filled with an ideal gas. Without a potential difference across the plates, the gas is electrically neutral; but a small number of "seed" electrons will be present, created by background ionisation processes such as cosmic radiation. When a potential difference is applied, seed electrons will accelerate towards the anode, with a net velocity (the "drift velocity") found by:

$$\upsilon_{drift} = \mu E \tag{2. 14}$$

where μ is the electron mobility and E is the applied electric field. At some point, the voltage will be sufficient to accelerate all available seed electrons and ions, and the current will not increase as voltage increases (the saturation region B - C). As seed electrons are accelerated towards the anode, they collide with neutral gas atoms. If they have sufficient kinetic energy, they ionise these atoms, liberating another electron, which will themselves be accelerated by the potential difference, and will collide with more neutral atoms, repeating the process. This leads to an *electron avalanche* or *Townsend Breakdown*. This is shown at point C in figure 5 and illustrated in figure 6.

If successive avalanches lead to sufficient production of secondary electrons to perpetuate the discharge, it will adhere to the Paschen breakdown law (Palmer 1974)

$$Pd = \frac{1}{(\alpha/P)} \ln\left(1 + \frac{1}{\gamma}\right) \tag{2. 15}$$

where P is the pressure, d is electrode distance, γ is the Townsend gas ionisation coefficient and α is the Townsend second ionisation coefficient for the cathode surface.

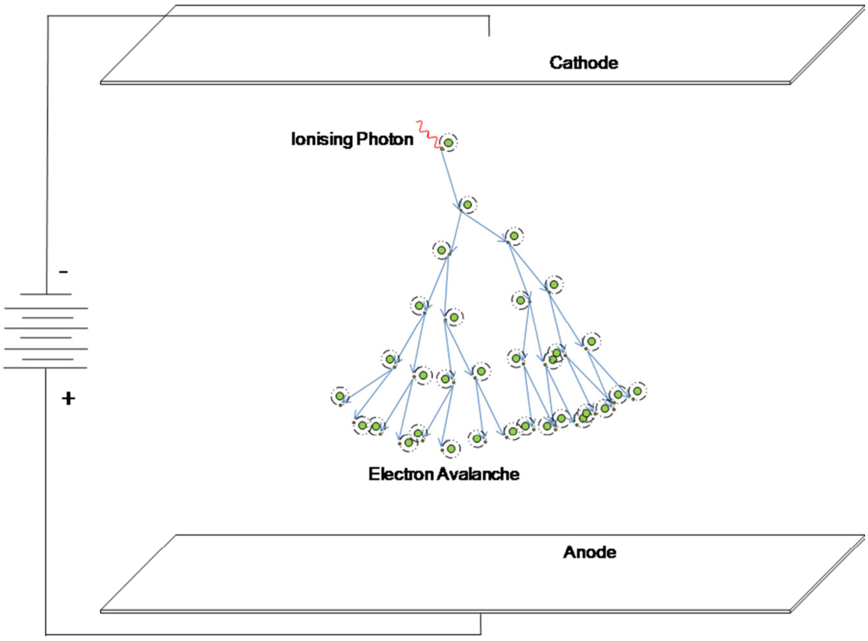

Figure 6: Avalanche Breakdown

Past the breakdown voltage, there will be a noticeable voltage drop, since there are enough charged particles to sustain the conducting channel (point E in figure 5). At lower currents, this is called the corona regime (point D on figure 5). As current increases, an observer will note that the volume of gas becomes luminous. Ions gain kinetic energy from the potential and accelerate towards the cathode. Kinetic energy is transferred to the cathode, either through the ions striking it directly, or indirectly by their collisions with the more numerous neutral atoms that gain kinetic energy and strike the cathode themselves. This energy causes atoms to be ejected from the cathode (sputtering). When excited by collisions with electrons, these atoms decay quickly and emit photons, which cause the glow visible to an observer (Mehta 2005).

If Pd in the Paschen Breakdown Law is so large that the space charge field of an individual avalanche becomes comparable to the applied field, another mechanism, streamer breakdown, occurs (Palmer 1974). Secondary avalanches (created by photo-ionisation by stray photons passing through the plasma) are attracted towards the electric field of the primary avalanche (it is comparable in magnitude to the applied field and offers a similar level of attraction). The individual currents from these multiple avalanches combine, forming a highly conductive channel, known as a “leader”. A spark will often form along the leader. The streamer breakdown condition, that the space charge field is equivalent to the applied field, is commonly known as Raether's breakdown criterion (Palmer 1974) and can be found with

$$\left(\frac{\alpha}{P}\right)Pd = 20 + \ln(d) \qquad \textbf{\textit{(2. 16)}}$$

II.3 Dielectric Barrier Discharge:

Dielectric Barrier Discharge (DBD) is a form of discharge plasma. While DBDs adhere to the same Paschen Law governing breakdown between metal electrodes (as discussed above), it is distinct from other discharges due to the placement of a dielectric material on the surface of one or both electrodes. A consequence of the use of dielectric barriers is a DC current cannot drive a DBD due to capacitive coupling (Kogelschatz 2000), rendering DBD a distinct form of discharge plasma. Figure 7 shows the most common DBD configurations; parallel plate (figure 7 (a), (b) and (c)), concentric cylindrical (d) and pin to plate electrodes (e). Placement of the dielectric layer can also vary; over one or both electrodes, or with a small gap between the electrode surface and the dielectric. Since a parallel plate configuration was utilised in our experiments, this will be the configuration described in the experimental section of this work.

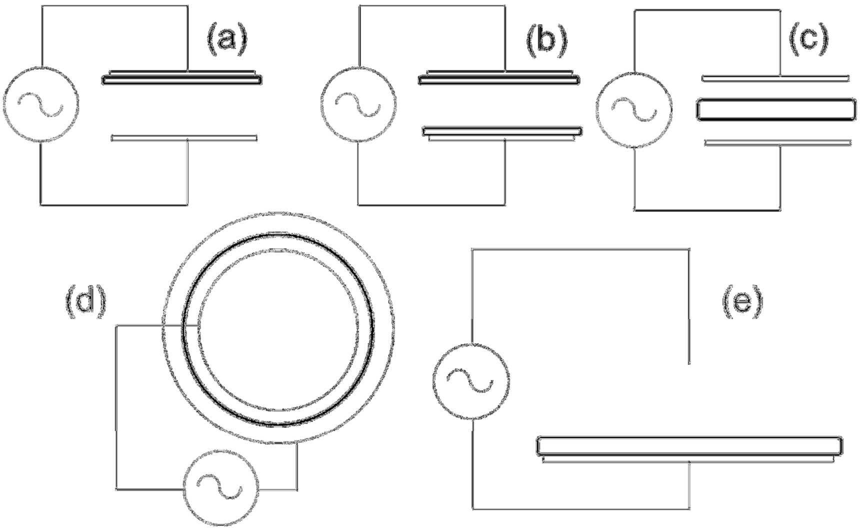

Figure 7: Common DBD Configurations

II.3.a Dielectric Barrier Discharge Formation:

When a voltage is applied across the electrodes at pressures in the range of atmospheric pressure (Kogelschatz 1997), the dielectric forces the build-up of greater amounts of charge than would otherwise occur and inhibits the arc formation between electrodes. Instead charge is transferred via short lived filaments or streamers. At the surface of the dielectric layer, filament channels spread out into surface discharges with a much larger diameter than the original channel (Kogelschatz 2000). Individual filaments have the properties of short lived, high pressure, weakly ionised glow discharges. Each filament is of cylindrical shape, with a radius of ≈100 µm and a short lifespan, on the order of several ns before a build-up of charge at its location collapses the electric field. During that time, electron densities are on the order of $10^{2o} – 10^{21}$ m^{-3} and current densities of 100 – 100 A cm^{-2} are reached (Kogelschatz 2003). Because of the short discharge filament lifetimes, only a small amount of charge is transferred by any one filament (≈100 pC) (Kogelschatz 2003), therefore little gas heating occurs. The build-up of charge discourages further filaments from forming at the same location while the voltage is rising. When the voltage is in the opposite direction, discharges tend to form at the site of previous filaments. This “memory voltage” effect is a characteristic of DBDs. Operation at high voltages and low frequencies encourage the spread of filaments over the dielectric surface. The formation of plasma is restricted to the microdischarge filament; the gas outside of the channel remains un-ionised and can absorb the dissipated energy and transport long lived gas species.

II.3.b Dielectric Barrier Discharge Applications:

The fact that DBD plasma is “cold” plasma, and that it can be generated at atmospheric pressure are its advantages over other discharges and make it suitable for several applications. DBDs were initially used on a large scale for the manufacture of ozone (O_3) (Manley 1943). By channelling air through tubes of borosilicate glass and subjecting them to a varying electric field, molecular oxygen is ionised and forms ozone molecules. Ozone has been in use for years as a steriliser and disinfectant in large ventilation systems (Kogelschatz and Eliasson 1988, Manley 1943). The ability to form plasma at low temperatures and high pressures also makes DBDs ideal to form the gain medium in high power CO_2 lasers. A combination of carbon dioxide (10 – 20%), nitrogen (10 – 20%), hydrogen (1 – 3%) and helium (60 – 80%) are excited by an AC voltage. The energy level diagram for a CO_2 laser is shown in figure 8.

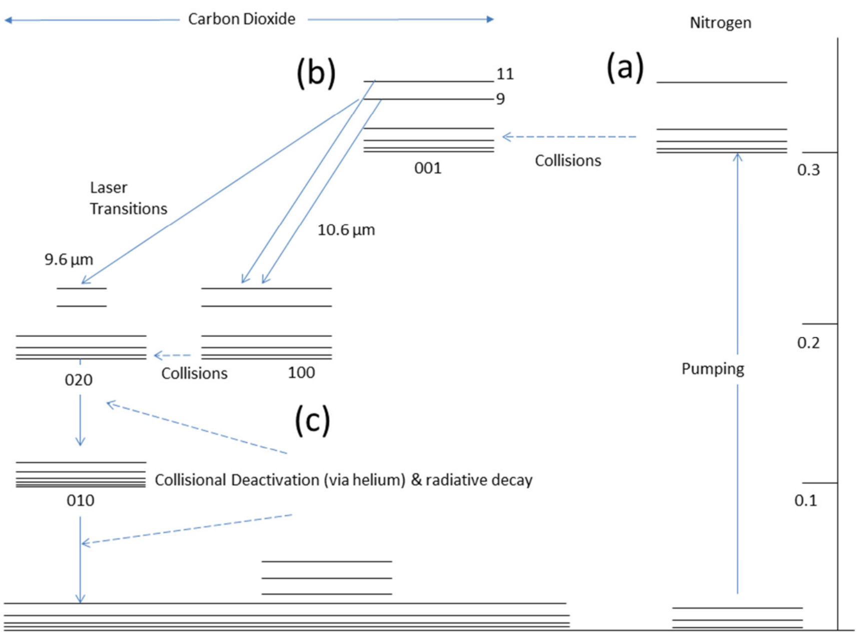

Figure 8: Energy level diagram of a Co_2 laser

Molecular nitrogen is excited vibrationally by electron impact and these vibrational states are metastable (figure 8 (a)). Collisions between excited molecular nitrogen and carbon dioxide excite the carbon dioxide, causing a population inversion (figure 8 (b)). Nitrogen molecules lose some energy, but are still in an excited state. The nitrogen molecules lose their remaining energy via collisions with helium atoms (figure 8 (c)) (Duley 1976).

Since the ozone generating properties of DBDs are well documented, and ozone is a known antibacterial agent, it is logical to expect that exposure to DBD plasma would be damaging to bacteria and single celled organisms. This has led a variety of researchers to examine the usefulness of various DBD configurations to antibacterial uses and related biomedical applications, see for example (Ries, et al. 2011, Kong, et al. 2009, Chiang, et al. 2010) and references therein.

II.3.c Diagnostic Methods:

Emission Spectroscopy:

Emission Spectroscopy is a powerful tool. By analysing the light emitted from an object, its structure, temperature and composition are revealed. Different chemical structures will emit light of characteristic wavelengths, so the chemical composition of a sample can be deduced. Atomic spectra are composed of sharply defined peaks, corresponding to particular energy transitions of electrons in atomic orbitals. Molecular spectroscopy is more complex, both the vibrational and rotational nature of a molecule affects the emission spectrum, as well as electronic transitions. Molecular emission patterns feature broad bands rather than discrete peaks. The presence of certain emission bands infers the presence of their associated species.

The plasma temperature can be estimated from an intensity calibrated emission spectrum. The intensity of the emitted light is proportional to the amount of energy within the plasma. Radiant spectral intensity will thus increase with temperature. The relative intensity between certain pairs of emission bands will also change with temperature.

Electrical Characterisation:

There are several important electrical parameters of DBDs that are necessary to characterise the system: discharge voltage, discharge current, charge transferred, power and reduced field strength. These parameters can be measured by a combination of voltage, current and charge measurement. The plasma regime can be inferred from observation of the voltage and current patterns over a cycle, as recorded on an oscilloscope. Plasma in the glow regime will exhibit a single current peak per half cycle; in contrast filamentary plasma will display a large number of short lived microdischarges. These microdischarges are illustrated schematically in figure 9 and appear in phase with the rising edge of the applied voltage signal U.

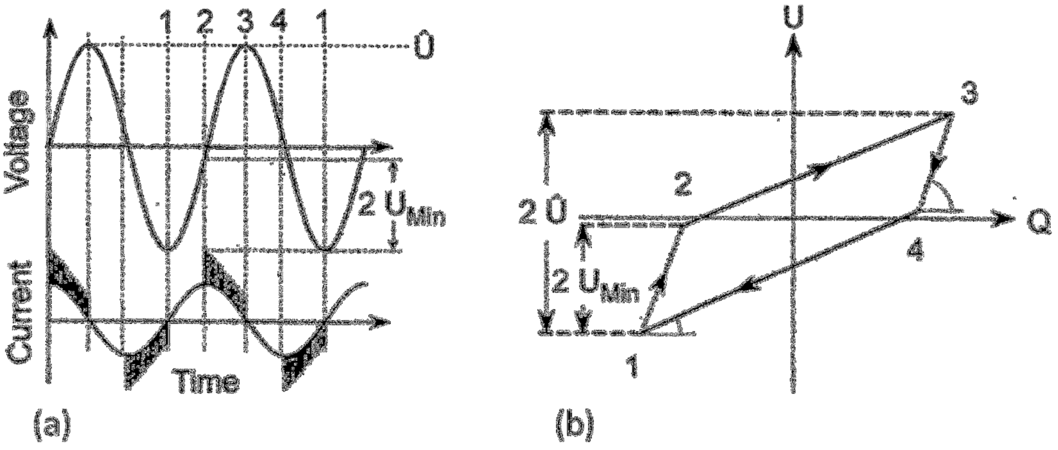

Figure 9: (a) Schematic I-V trace showing filamentary plasma microdischarge behaviour (b) Schematic Q-V plot with major features highlighted. Corresponding points on both graphs numbered 1 to 4 (Kogelschatz 2003)

The microdischarge duration can be measured from the current signal plotted in this manner. By measuring the duration for which microdischarges are occurring, the duty cycle can be calculated.

Several parameters can be measured from Q-V plots. A typical Q-V plot of a DBD will trace a parallelogram shape as illustrated in figure 9 (with major features highlighted). Models established in many previous works e.g. Manley (1943), Falkenstein & Coogan (1997) , Yehia & Mizuno (2005), Zhang et al (2010) and references therein treat the device like a gap capacitance C_g and a dielectric capacitance C_d placed in series. The discharge voltage U_d will remain approximately constant during microdischarge activity. The corresponding Q-V graph will provide characteristic values for $C_{tot} = (C_g^{-1} + C_d^{-1})^{-1}$ and C_d (from the slopes of the parallelogram straight sections), the electric power P consumed by the discharge per cycle, the discharge voltage U_d and the average reduced field strength, respectively. The breakdown voltage (U_b) can be found by measuring the horizontal distance between the "sides" of the parallelogram ($2U_b$). The maximum applied voltage (U_{Max}) can be found by measuring the horizontal distance between the opposite corners ($2U_{Max}$). The power consumed by the system is represented by the area enclosed by the figure, regardless of the shape of the plot; since the area of the figure is equivalent to the integration of the total current per cycle (the charge q) multiplied by the voltage. The temporally averaged reduced field strength, a measure of the ratio of electric field to the neutral particle density (E/n) can be calculated by dividing the breakdown voltage by the product of the pressure and electrode distance $\langle E/p \rangle = U_{Min}/pd$.

II.4 Laser Plasma

By focusing a beam of laser radiation onto a suitable target material, a plume of ionised particles will be produced. Such a plasma will have temperatures in the range $10^3 - 10^4$ K and particle densities of 10^{18} cm^{-3}. The characteristics of a laser plasma are governed by the laser pulse duration, laser power, wavelength and irradiance, which will be described in greater detail herein.

The earliest forays into laser generated plasmas utilised CW lasers. However, with the advent of electronic Q switching in the mid-1960s, it became possible to concentrate a large amount of energy into a short pulse, minimising loss through heat conduction into the volume of the target, widening the scope of target materials (Chrisey and Hubler 1994).

II.4.a Pulsed Laser Deposition

Pulsed laser deposition (PLD) is a process in which a laser generated plasma is incident upon a given sample in order to alter the characteristics of its surface or to deposit material upon it, illustrated in figure 10. PLD is a versatile deposition technique:

- It is possible to grow microstructured films at relatively low temperature
- Multi-component thin films can be grown by the appropriate use of targets
- Films have the same stoichiometry as the targets used to grow them

However, it has certain disadvantages:

- Thin films can be grown only on small areas, large scale PLD is difficult and time consuming.
- It is difficult to ensure uniformity of films and nanostructures.

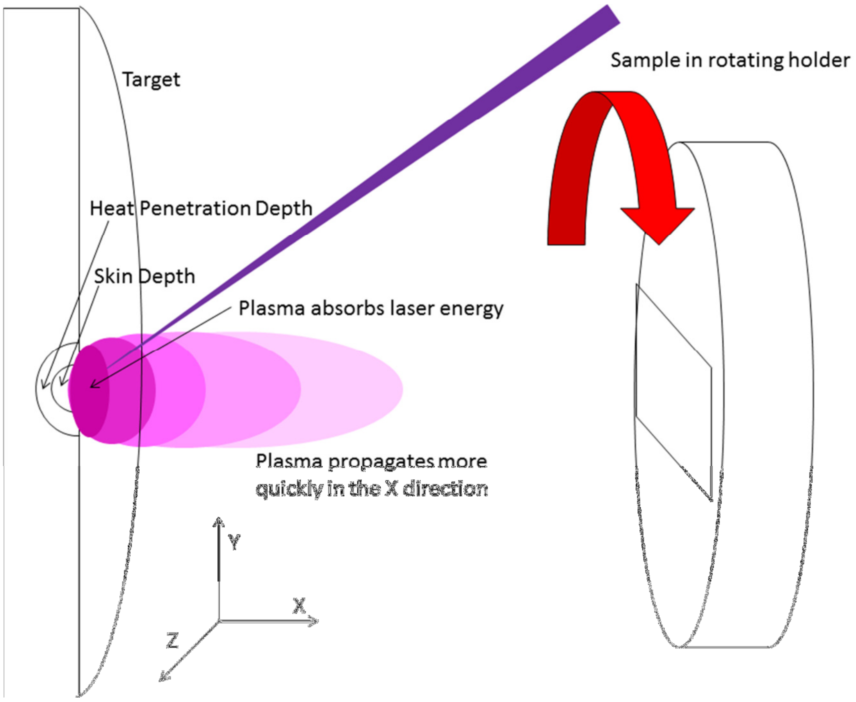

Figure 10: Diagram o f PLD plasma formation and propagation

The PLD process is complex, consisting of interaction between the laser and target surface, propagation of the plasma plume and interaction between the plasma and the substrate surface. A comprehensive explanation is found in the Ph. D thesis of Richard O Haire (2009). To simplify analysis, the *adiabatic limiting case* of the PLD process is useful; by making the assumption that the time taken for the target to heat and plasma to form is much less than the time taken for the plasma plume to propagate outwards, the process can be divided into two distinct stages (Amoruso, et al. 1999)

1. Interaction of the laser with the target: heating, vaporisation and plasma formation
2. Plume expansion in vacuum or background gas.

When laser light is incident upon the target surface, some fraction is reflected. The rest is absorbed by the target material. This energy will penetrate the surface of the material to a certain depth, the "skin depth", in which the electrons absorb the energy and are excited to higher energies. The material is quickly heated to vaporisation point, and the sudden change in pressure gradient causes mechanical shock, ablating material from the target surface. The skin depth (δ) to which a laser pulse will penetrate can be calculated in the following manner

$$\delta = \sqrt{\frac{2}{\omega\mu\sigma}} \tag{2. 17}$$

where ω is the angular frequency of the light, μ is the magnetic permeability of the target material and σ is the conductivity of the target material.

However, not all the absorbed laser energy is absorbed within the skin depth, heat is transferred to the material immediately surrounding it (the heat penetration depth L_{heat}). The depth to which heat is transferred is a function of the mass density of the material (ρ), the thermal conductivity of the material (k), the speed of light (c) and the pulse width of the laser (t_{pulse}).

$$L_{heat} = \sqrt{\frac{2kt_{pulse}}{\rho\, c}} \tag{2. 18}$$

When dealing with nanosecond laser pulses, the pulse duration is sufficient for heat to build up within the target to this depth. Metals need a great deal more energy to be vaporised than to simply melt, therefore vaporisation (and hence, ablation) will occur only if the latent heat of vaporisation per unit volume is exceeded by the energy that is absorbed (Amoruso, et al. 1999).

$$F_{laser} \geq F_{threshold} \exp(\alpha z) \tag{2. 19}$$

The ablation depth will be governed by the ratio of the laser fluence to the latent heat of the target

$$z_{ablation} \approx \alpha^{-1} \ln\left(\frac{F_{laser}}{F_{threshold}} \right) \tag{2. 20}$$

$$F_{threshold} = \frac{\rho\, L_{t\arg et}}{\alpha\, A} \tag{2. 21}$$

The depth of material that will become ablated ($z_{ablation}$) can thus be calculated as a function of the fluence of the laser (F_{laser}), the area of the target that is irradiated (A_{target}), the latent heat per unit mass of the target (L_{target}) and the fluence threshold for vaporisation ($F_{threshold}$).

$$z_{ablation} = \frac{A(F_{laser} - F_{threshold})}{\rho \; L_{t\arg et}} \qquad \textbf{\textit{(2. 22)}}$$

When ablated material impinges upon the substrate, Van der Waals forces will cause it to condense on the surface. When a particle impinges upon the substrate, it will feel an attraction or repulsion that is a function of the distance between them. This is the Lennard Jones (L-J) potential, and is represented by

$$V_{L-J} = 4\varepsilon\left[\left(\frac{\sigma}{r}\right)^{12} - \left(\frac{\sigma}{r}\right)^{6}\right] \qquad \textbf{\textit{(2. 23)}}$$

where ε is the depth of the potential well σ is the finite distance at which the inter-particle potential is zero, r is the inter particle distance. The L-J potential can also be written in the following manner

$$V_{L-J} = \varepsilon\left[\left(\frac{r_{\min}}{r}\right)^{12} - 2\left(\frac{r_{\min}}{r}\right)^{6}\right] \qquad \textbf{\textit{(2. 24)}}$$

where r_{min} is the distance at which the potential is at a minimum. At distances greater than r_{min} the particle will be adsorbed, otherwise it will be repelled. Under these conditions, the atoms/molecules will adhere to the surface, whether by a physical or chemical mechanism and begin to arrange themselves. When atoms are absorbed onto the substrate, they become adatoms (adsorbed atoms) and have positive adsorption energy E_a relative to the vapour. Depending on the surface energy of the substrate ($\delta_{subinstrate}$), the surface energy of the film (δ_{film}) and the energy of the substrate film interface (δ_{sf}), this can happen in several ways, illustrated in figure 11:

- Layer by layer growth, also known as Frank Van der Merwe growth, occurs when $\delta_{substrate} > \delta_{film} + \delta_{sf}$. Material attaches in even layers across the substrate surface, and grows in a homogeneous fashion. New layers only begin to form when the previous layer is complete. Van der Merwe growth can lead to high quality epitaxial films.

- 3D Islands (Volmer Weber growth) occurs when $\delta_{substrate} < \delta_{film} + \delta_{sf.}$ Material nucleates and forms “islands” which grow both upwards from the substrate and outward, toward each other. Volmer Weber growth can lead to polycrystalline films.
- Stranski Krastanov growth is an intermediate stage between Van der Merwe and Volmer Weber growth. It is observed that films will begin with uniform layers, laid sequentially, which are then succeeded by the growth of 3D islands.

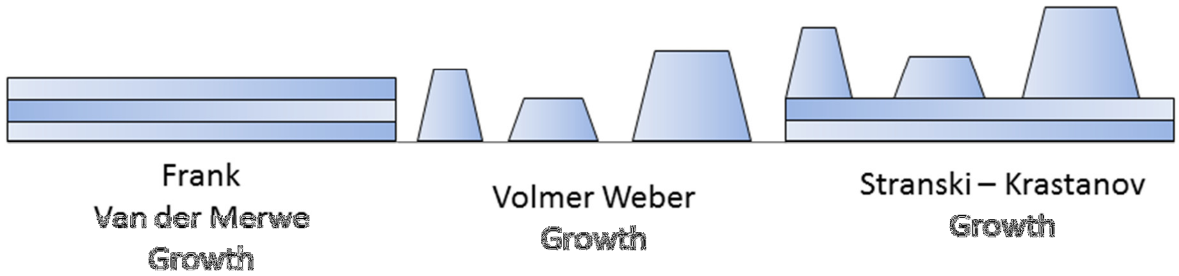

Figure 11: Thin film Growth Modes

When an atom is adsorbed, it finds itself in a small potential well. Due to its internal energy, the atom will attempt to surmount the mitigation barrier. The probability that it does so successfully is the product of the number of attempts it makes per second (ν_d) and the probability that it will surmount the barrier in each attempt

$$\nu_d \ e^{-(E_d / kT)} \tag{2. 25}$$

From this, the adatom diffusion coefficient (D) can be calculated

$$D = \nu_d \, l^2 \, e^{-(E_d / kT)} \tag{2. 26}$$

The diffusion coefficient can be interpreted as the number of unit cells through which the adatom passes per unit time. The desorption time is

$$\tau_a = \nu_a^{-1} \, e^{(E_a / kT)} \tag{2. 27}$$

The distance that the adatom can move can be found using

$$L = \sqrt{D \tau_a} \tag{2. 28}$$

The adatom is weakly bonded to the substrate surface, but can move along its surface, and may encounter another adatom, a step/ledge (two or more adatoms already joined), a kink (a corner formed by two steps), a terrace (a gap surrounded on 3 sides) or a hole in the surface. If it does so it will attempt to occupy whatever state has the lowest energy that is available.

II.4.b Thin Film Characterisation:

Films grown using PLD are characterised using the following techniques, to establish structure and morphology and electrical characteristics.

Atomic Force Microscopy:

The surface structure of a thin film can be investigated using atomic force microscopy (AFM). A small tip is brought into close proximity of the surface, and interactions between the tip and the surface due to Van der Waals forces cause it to deflect, enabling accurate scans of surface structure, roughness and morphology. In this work, it was used to image the film surface structure and to quantify surface roughness. The effects on surface morphology and roughness of growth pressure, deposition temperature and film thickness were investigated.

Van der Pauw measurement:

The interest in the growth of transparent conducting oxides is due to their useful electrical properties, which would make them ideal for applications as diverse as flat panel displays and as substrates in microbial fuel cells. The conductivity of such films needs to be measured and controlled precisely. Van der Pauw measurement is a method of electrical resistance measurement. It is suited to the measurement of resistivity of thin films. The Van der Pauw method can be used to measure a sample's sheet resistance, carrier concentration and doping type. In this work, it was used predominantly to measure the undoped and aluminium doped zinc oxide. In order to function efficiently as substrates for microbial fuel cells, these films must have good conductivity. By measuring the sheet resistance, resistivity can be calculated. This in turn can be used to calculate conductivity. One of the aims of this work is to investigate the effects of pressure, growth temperature and doping on the resistivity of thin films.

X-ray Diffraction:

X-ray diffraction is used to investigate the crystal structure of samples. Thin films grown on crystal substrates will form crystal structures. Films grown on amorphous substrates will initially be amorphous, but exhibit greater crystal structure as thickness increases. This will manifest by the appearance of diffraction peaks at certain wavelengths. Crystal structure will affect the structural and electrical properties of the film. One of the aims of this work is to investigate the effects of pressure, growth temperature and doping on the crystallinity of thin films deposited on amorphous substrates.

Profilometry:

In order to make accurate calculations of resistivity, the film thickness must be known. Contact profilometry is a method to measure film thickness. Profilometry allows the film thickness to be measured with and nm accuracy and, by measuring film thickness as a function of the number of laser shots used to deposit the film, it is possible to estimate the mean thickness of films per shot.

Water Contact Angle Measurement:

The hydrophobicity of a thin film is important when growing microbial films. Bacteria require films that are slightly hydrophilic (with contact angle less than 90^{o}) to adhere. However, they will not pack in a dense fashion on an extremely hydrophilic surface. This lowers current density output. One of the aims of this work is to determine the effects of film thickness, doping, growth pressure, growth temperature and crystal structure on the hydrophobicity of thin films.

Bacterial Electrical Characterisation:

The investigation of the electrical output of the microbial films grown as part of this work is of central importance. What is of interest to researchers is not just the total power output, but also the change in current density over time, and with respect to different applied potentials. These changes can indicate changes in the bacterial population or exhaustion of their nutrient source. When performing chronoamperometry (CA), the current density of the microbial films is measured under a constant voltage as a function of time. CA is a useful analytical tool for determining initial information about nucleation and growth mechanism in a system (Avci 2007, 32). The recorded current can be analysed and its nature can be identified from the variations with time. CA provides a measure of extracellular electron transfer (EET) in electroactive biofilms. Higher current density (at the same applied potential) indicate a faster EET rate, thus the system biofilm/electrode is capable of oxidizing the carbon source and transfer the electrons to the electrode. Cyclic voltammetry (CV) is performed by applying a time varying voltage and measuring the current density. CV is the main method in modern electrochemistry. Using CV, it is possible to learn information on the type of reactions that occur in the system and the potentials at which they occur. CV gives an indication about the concentration of electroactive species, their peak potential and the time constant of the various simultaneous EET process. Schematic diagrams of a typical CA and CV graph are illustrated in figure 12 (E. Marsili, J. R. Rollefson, et al. 2008).

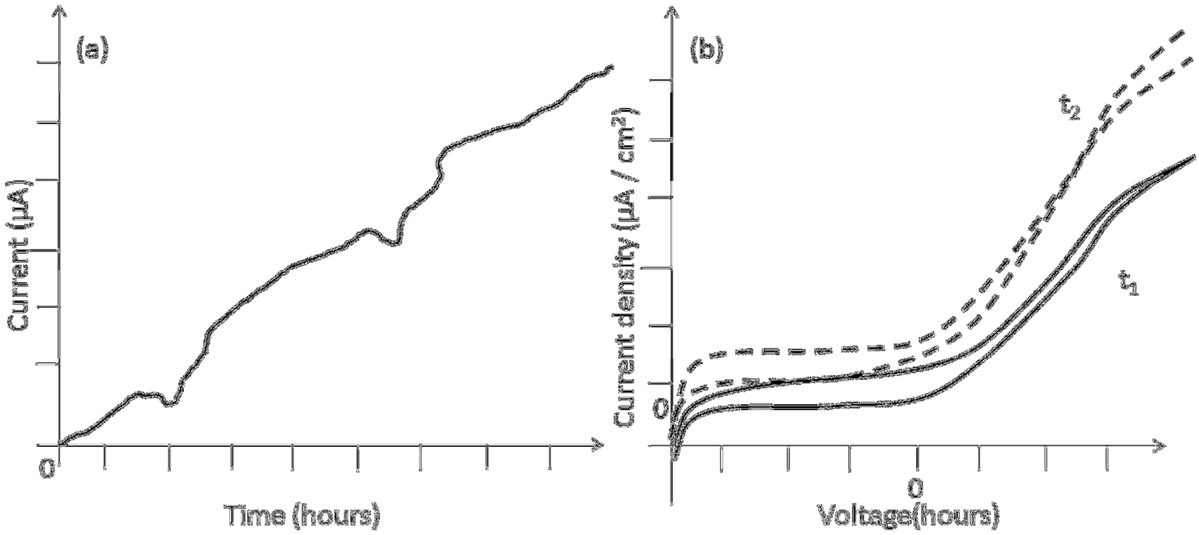

Figure 12: Schematic diagram of (a) CA graph and (b) CV graph

Chapter III: Experimental Methods and Background

This section will introduce the various apparatus that were utilised in the course of this research; the experimental setups constructed for this work will be described in detail, as will the equipment used to perform characterisation, along with a brief background explanation of the characterisation methods.

III.1: Dielectric Barrier Discharge Experiment

III.1.a: DBD Setup:

The apparatus for creating a DBD consists of a transformer to convert from 240 V to 110 V. This is necessary as the high voltage transformer required for this apparatus is manufactured in the United States. This is connected to a high voltage transformer that converts mains voltage to a rated output of 15 kV and 30 mA. This transformer is “floating”, thus the peak potential difference between the electrodes is approximately 30 kV. To this transformer are connected a pair of electrodes via high voltage cable. Electrodes are made from single core wire with a total thickness of 3 mm (core diameter 2 mm, insulating sheath 0.5 mm) wrapped around 4 mm thick wooden formers. The electrodes have a surface area of 10 cm × 10 cm,

The electrodes are mounted on threaded nylon bars and separated by nylon nuts, allowing the electrode separation to be precisely controlled. The electrode separation is measured using a ruler. Plate separations were between 30 and 100 mm. The entire apparatus was placed on a laboratory jack to allow height adjustment of the apparatus with respect to the (fixed) position of the optical fibre. The electrode gap was changed by adjusting the position of the upper electrode with respect to the “fixed” lower electrode, the entire system was then moved vertically to align the optical fibre tip with the centre of the electrode gap, measured with a ruler with an accuracy of 0.5 mm. The set-up is illustrated in figure 13.

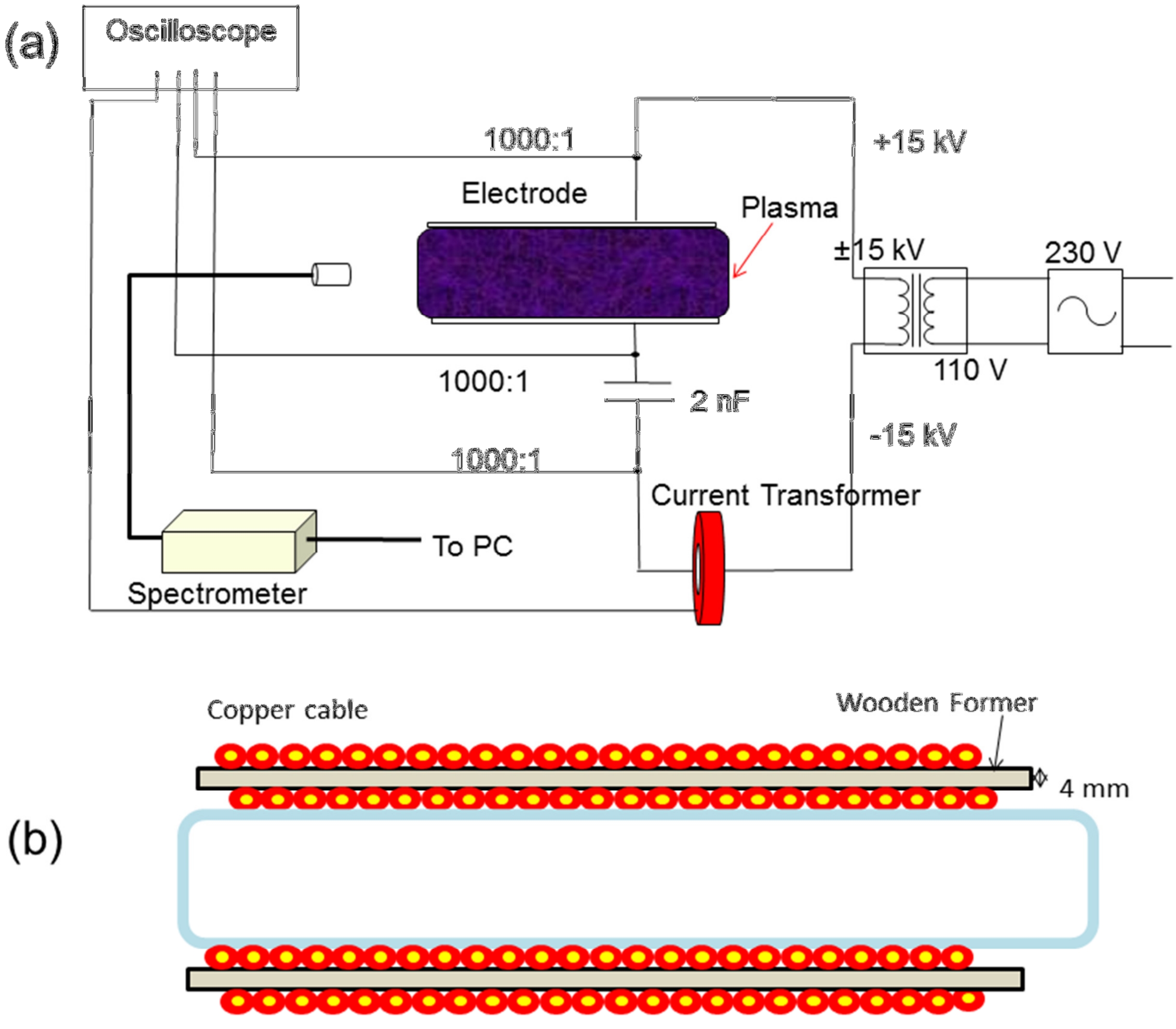

Figure 13: (a) Schematic diagram of DBD setup (b) Cross section of electrode

III.1.b: Leak Rate Estimation:

A 5 litre polythene zip lock sandwich bag, filled with helium is placed between the electrodes. The bag is flattened, and all gas expelled. A 6 mm polythene tube is inserted through the zip lock seal and an airtight seal formed around it by finger pressure. The presence of air in the plastic bag plays an important role in the dielectric barrier discharge. The zip lock permits some gas exchange. Being able to quantify the ratio of helium and air inside the bag is important. To estimate the leak rate of the bag, the rate of change of its mass was measured over time. The bag was filled to capacity with helium gas and placed on a scale of 0.001 g accuracy. Thirty seconds was allowed for the mass to settle, and a reading taken. The mass of the bag and gas was recorded at intervals of two minutes for a period of 40 minutes. The results are shown in table 2 and illustrated in figure 14. The initial error bar represents the variation in the starting mass of the bag, the error bars on subsequent data pints represents the error of the weighing scale. Bags were used for 5 to 7 experiments before being discarded. During this period of time, no damage (burning, scorching, tearing) was ever observed.

Table 2: Bag leak rate

Time (minutes)	**Weight (g)**	**Time (minutes)**	**Weight (g)**	**Time (minutes)**	**Weight (g)**	**Time (minutes)**	**Weight (g)**
0	6.686	10	6.723	20	6.752	30	6.78
2	6.7	12	6.73	22	6.756	32	6.786
4	6.707	14	6.735	24	6.763	34	6.8
6	6.713	16	6.741	26	6.768	36	6.794
8	6.717	18	6.745	28	6.774	38	6.806
						40	6.812

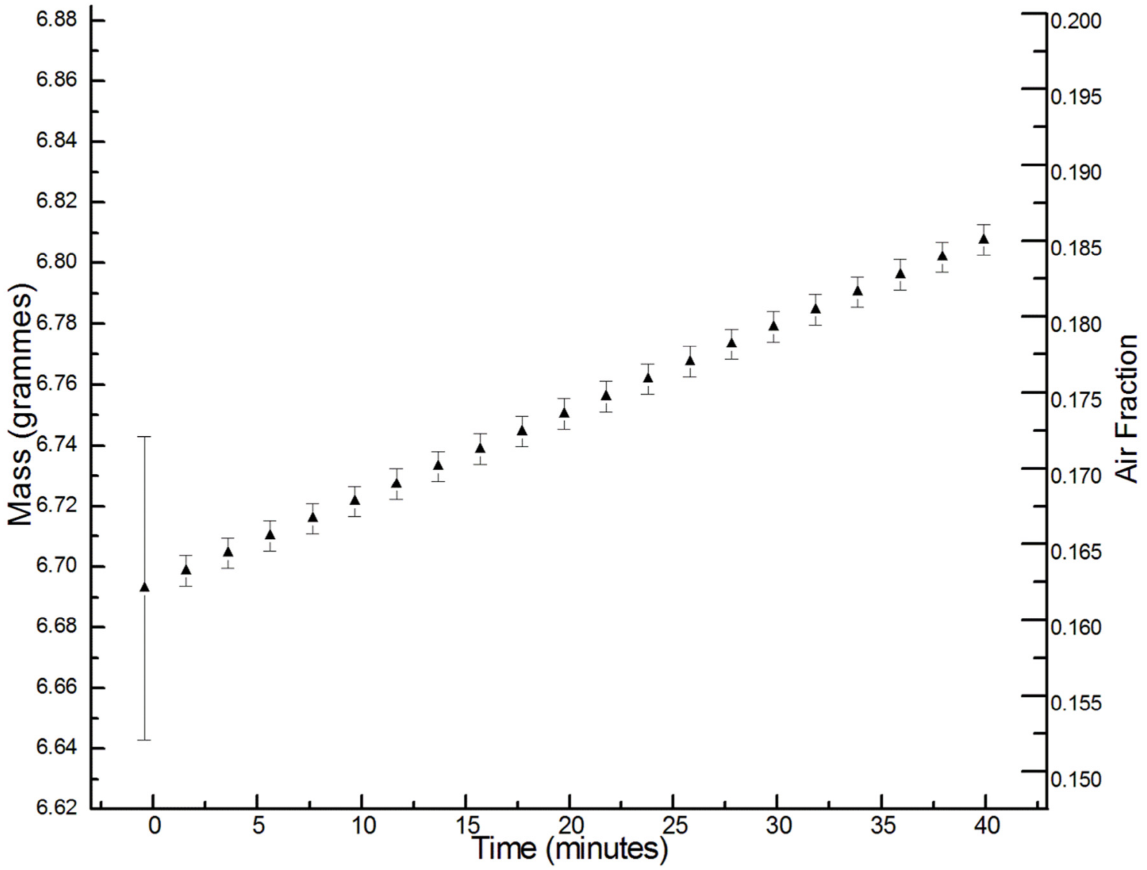

Figure 14: Graph of bag leak rate

The air fraction in the bag was estimated by estimating the weight of a bag with 100 % helium using the molar volume and molar mass of helium.

$$\frac{5}{24.04}\times 4 = 0.83g \tag{3. 1}$$

The buoyant effect of the helium was estimated, it is equal to the weight of the displaced air

$$5\times 1.2043 \; = 6.0215 \; g \tag{3. 2}$$

The value given for the density of helium at atmospheric pressure at 20^0 C is 0.1785 g/L. The value given for the density of air at atmospheric pressure at 20^0 C is 1.2043 g/L. To estimate the initial gas composition, we estimate the mass of pure helium that would produce the first reading (6.686 g) and compare it with the measured value using

$$V_{molar} = 0.08206\times T \tag{3.3}$$

where "T" is temperature in Kelvin. At atmospheric pressure and 20^0 C, the molar volume of helium is 24.04 L. Since the molar mass of helium is 4 g, then 24.04 L of helium has a mass of 4 g, therefore the mass of 5 L of helium will be

$$\frac{5}{24.04}\times 4 = 0.83g \tag{3.4}$$

We must also take into account the buoyant effect of the helium, which is equal in weight to the displaced mass of air.

$$5\times 1.2043 \; = 6.0215 \; g \tag{3.5}$$

Therefore, the reading on the scale pan will be due to the mass of the bag, the mass of the helium and the buoyant force of the helium.

$$R_{He} = 11.03 + 0.83 - 6.02 = 5.84g \tag{3.6}$$

Since the reading on the scale is 6.686 g, the difference in these masses can only be accounted for by some presence of the helium in the bag by air. The difference in mass is 0.85 g. If one lets "x" be the fraction of air in the bag.

$$x = 1 - \frac{10.655}{V} + \frac{0.966}{V}R \tag{3.7}$$

This gives the fraction of air. The bag has a stated volume of 5 L, and when fully inflated, was measured and its dimensions multiplied to calculate a volume of 4.5 L. The difference was split, and a mean value of 4.75 L ± 0.25 L was used. The mean percentage was 11.4 % ± 4.7 %.

The contribution of the differing rates of permeation of various gases through the polyethylene wall of the bag was also assessed. Permeability is defined as the volume of gas, in cm^3, that would pass through a cm thickness of the bag material (low density polyethylene) which has an area of 1 cm^2 per second per 1 Pa of pressure difference. Permeability rates for oxygen, nitrogen and water vapour were obtained from the website for Goodfellow, a company that caters for the material needs of the research and industrial community (Goodfellow.com) and are listed in table 3.

Table 3: Permeability of various gases

Gas:	**Permeability at 25^O C ($\times 10^{-13}$ $cm^3.cm.cm^{-2}s^{-1}Pa^{-1}$)**
Carbon Dioxide	10
Hydrogen	8
Nitrogen	0.7
Oxygen	2
Water	70

The bag was calculated to have a surface area of 1.49×10^3 cm^2 and a thickness of 50×10^{-4} cm. Using the Ideal gas Law, the mass of 1 cm^3 of the above gases was calculated and diffusion rates were calculated. Using the permeability figures listed in table 3, the diffusion rates of various gases were calculated in this manner and given in table 4.

Table 4: Diffusion rates of various gases through polyethylene film

Gas	**Diffusion rate ($g\ s^{-1}\ Pa^{-1}$)**
CO_2	5.85×10^{-8}
H	2.15×10^{-9}
N	2.61×10^{-9}
O	8.52×10^{-9}
H_2O	6.53×10^{-7}

From these figures, it was concluded that air intake is primarily through the zip lock of the bag and not by diffusion through the bag material.

III.1.c: Bacterial Preparation:

Bacterial samples were prepared by colleagues from the DIT School of Food Science and Environmental Health. Δ*soxR*, Δ*soxS*, Δ*oxyR*, Δ*rpoS*, Δ*dnaK* mutants and their isogenic parent *E. coli* K12 were obtained from the National Bio-Resource Project, Japan (NIG, Japan). These mutants have had certain genes deleted, which are mainly transcriptional regulators (*soxR*, *soxS, oxyR* and *rpoS*) capable of responding to, amongst others, hydrogen peroxide and superoxide radicals and thereby can serve as markers of the generation of these species in our plasma (Baba, et al. 2006). Cells were grown in 10 mL of TSB-G, incubated for 18 hours, harvested by centrifugation at 10,700 rpm for 10 min at 4 ^{o}C and washed with sterile phosphate buffered saline. A model system of agar-agar gel was used to assess the efficacy of plasma treatments on microbial inactivation. 1 mL of the washed culture was spread onto each of the agar-agar plates. After a drying period of approximately 30 minutes the plates (without the lid) were placed into the bags previously mentioned and then between the two electrodes, ensuring that the petri dish was not in the direct path of the plasma stream. A 40 mm electrode gap was used during the plasma processing. The treatment was carried out for 5 minutes at 22 ^{0}C. Each sealed bag was then stored at room temperature for 1.5, 3, 18, 21 and 24 hours, respectively. Experiments were conducted in triplicate i.e., three separate plasma treatments of the same prepared inoculum. Colony forming units (CFU per cm^{2}) were obtained after

(i) Stomaching of the (treated) agar-agar samples in Maximum Recovery Diluent (MRD),
(ii) Performing appropriate dilutions in MRD,
(iii) Plating 0.1 mL of the diluted sample in TSA plates and
(iv) Incubating the plates at 37oC for 48 hours.

The bacterial population was measured by colleagues from the DIT School of Food Science and Environmental Health.

III.1.d: Emission Spectroscopy:

To perform ES, light emitted from the sample under investigation is captured and passed through a dispersive optical system; a prism or, more commonly, a diffraction grating. The light is dispersed into its component wavelengths and is allowed to fall onto a light sensitive surface; a photographic film, or a charge coupled device (CCD). The intensity is then recorded as a function of wavelength, creating an emission spectrum. The angle by which light is dispersed is a function of its wavelength and is governed by the grating equation

$$m\lambda = d\left(\sin(\theta_i) - \sin(\theta_m)\right) \tag{3. 8}$$

where λ is the wavelength of the light, d is the width of the slit in the grating, m is the order and θ_i is the angle of incidence and θ_m is the angle of diffraction. A schematic of a grating with the major features highlighted is illustrated in figure 15.

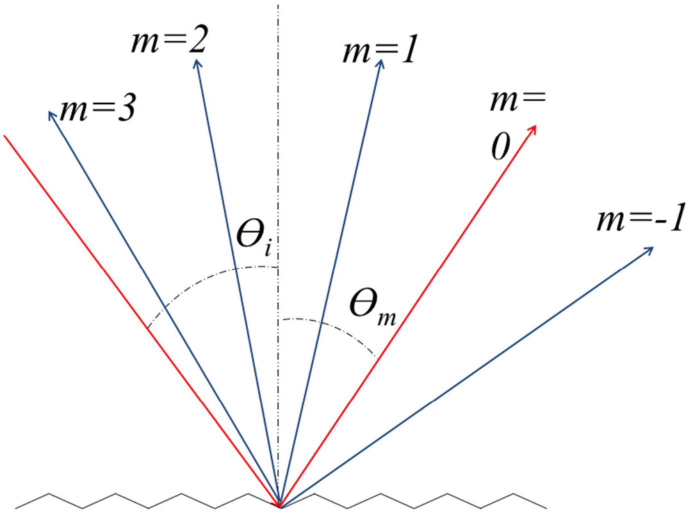

Figure 15: Grating Equation Diagram

A Stellarnet EPP 2000C-25 optical spectrometer that couples light from the plasma onto a curved diffraction grating via an optical fibre was utilised. The fibre is optimised for use in the ultraviolet and visible portion of the spectrum. The diffraction grating has a radius of curvature of 40 mm, 590 grooves per mm and the spectrometer entrance slit width is 25 µm. The spectrometer wavelength range is 190 nm to 850 nm. The tip of the optical fibre was mounted on an optical rail to facilitate focussing and maximising light collection. The spectrometer is connected by a USB cable to a PC with Stellarnet "SpectraWiz" software. This program interprets the signal from the spectrometer and displays the emission spectrum.

It is important to collect as much light as is possible by exposing the CCD for as long as possible (the integration time). Any background light or stray photons will also be detected as noise. As exposure time increases, photons absorbed across all wavelengths increases, so noise will increase by the same proportion as the signal. With an intense light source the number of photons collected from the source will far exceed the background noise. But if the light source is not intense, the number of photons from the source may be comparable with the background noise, making extraction of the signal difficult. To minimise noise, the signal is averaged over successive exposures. Random noise averages out to zero over time, while the average signal intensity will remain the same. Experiments were integrated over 5 seconds and averaged over 5 samples.

The emission spectroscopy experiments performed are concerned with the emission from diatomic molecules. The electronic potential energy of a diatomic molecule is represented schematically as a function of internuclear distance in figure 16. Consider two atoms approaching each other, at a minimum distance, the attractive and repulsive forces of electrons and nuclei balance each other out. This diatomic molecule can be represented in a useful way by graphing the potential energy as a function of internuclear distance. As the distance decreases, the repulsive forces of the nuclei dominate, and the potential energy curve rises steeply. As the internuclear distance grows, the potential energy reaches a minimum before rising again as the attractive forces begin to dominate. Beyond a certain distance, these forces lose their effect and the potential energy levels off, the atoms are dissociated.

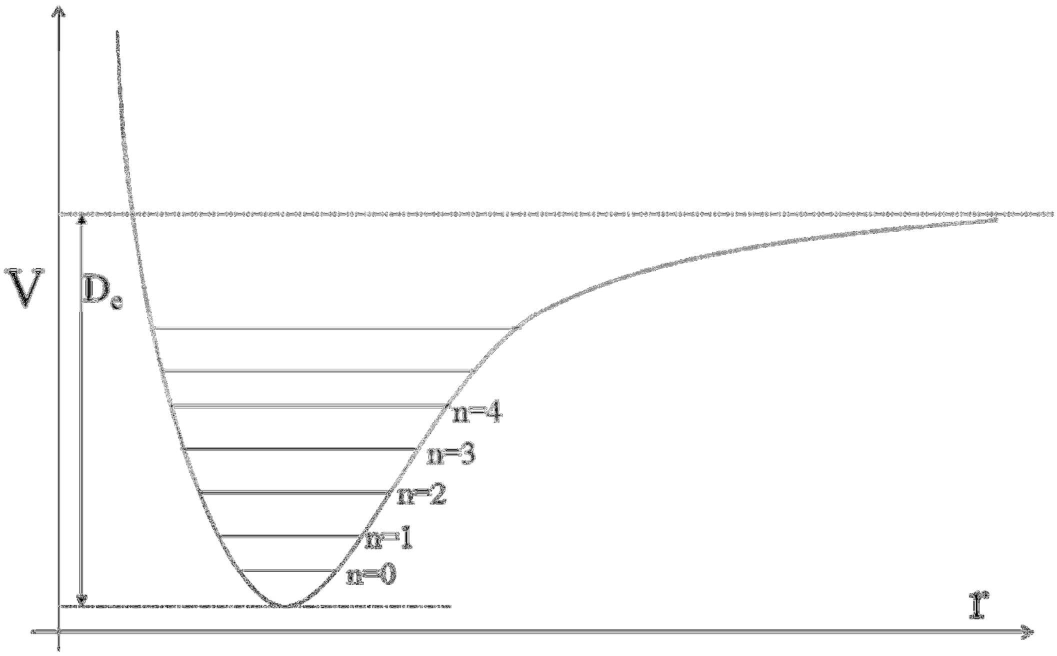

Figure 16: Schematic diatomic molecule energy level diagram

Two atoms approach until all their kinetic energy will be converted into potential energy. They will then reverse direction and travel apart. Due to loss of energy through collisions, the atoms become trapped in the potential energy well. The kinetic energy is at a maximum when the potential energy is a minimum, at the bottom of the potential well. It is about this point that the nuclei will oscillate. The behaviour of a diatomic molecule can be accounted for by splitting the total energy into electronic, vibrational and rotational energies (the Borm-Oppenheimer approximation). A diatomic molecule can be thought to obey Hooke's Law, in which case the restoring force (F) for two nuclei separated by a distance r is

$$-F = \frac{dV}{dR} = k(r) \qquad \textbf{(3. 9)}$$

And the potential energy V is

$$V = \frac{1}{2}k(r)^2 \qquad \textbf{(3. 10)}$$

This equation holds true for small r, however as internuclear distance increases, the shape of the potential well is more accurately described by the Morse function

$$V = D_e(1 - \exp[-\beta(r)])^2 \qquad \textbf{(3. 11)}$$

Where D_e is the bond dissociation energy. The term β is given by

$$\beta = 1.2177 \times 10^{-7}\, h v_0 \sqrt{\mu / D_e} \tag{3. 12}$$

where v_0 is the classical frequency and μ is the reduced mass of the molecule.

$$\mu = \frac{m_1}{m_1 + m_2} r \tag{3. 13}$$

Classically, if the nuclei have no kinetic energy, they will be at rest at the bottom of the potential well. If they have some kinetic energy, they will oscillate between two points higher on the well. This vibrational energy is quantised; the vibrational energy level is given by

$$E_v = h v_0 (v + 1/2) \tag{3. 14}$$

Where v is the vibrational quantum number (v = 0, 1 2…). The vibrational energy levels are represented graphically by horizontal lines across the potential well, illustrated in figure 16. The diatomic molecule also possesses rotational energy. The molecule is treated as a rigid rotator, rotating about its centre of mass. The rotational energy is given by

$$E_r = \frac{1}{2I} J(J+1) \left(\frac{h}{2\pi} \right)^2 \tag{3. 15}$$

Where I is the moment of inertia and J is the rotational quantum number. When a molecule absorbs energy it transitions from the ground state to an excited state. An excited state will have a different minimum potential energy and internuclear distance. The asymptote of the Morse curve will be higher than the ground state molecule. Similarly, the electronic energy is represented by placing the minimum of the potential energy well above the ground state molecule. The bond dissociation energy and the internuclear distance will also be different for a molecule with an excited atom. Electronic transitions may occur between excited and ground state molecules under certain conditions. Firstly, at T = 300K nearly all molecules have v = 0, so transitions occur from near the bottom of the potential well. Secondly, since harmonic oscillators are found most often near their turning points (except for v = 0 which has one central probability maximum), transitions can be thought of as occurring from on the ground state potential energy curve. Thirdly, because the time of a transition is much shorter than that of a vibration, transitions can be thought of as occurring vertically on a potential energy diagram (the Franck – Condon principle). If the excitation energy is less than the dissociation energy, the observed spectrum will be discrete. If it is greater, a continuum spectrum will be observed. The Franck – Condon principle is illustrated in figure 17.

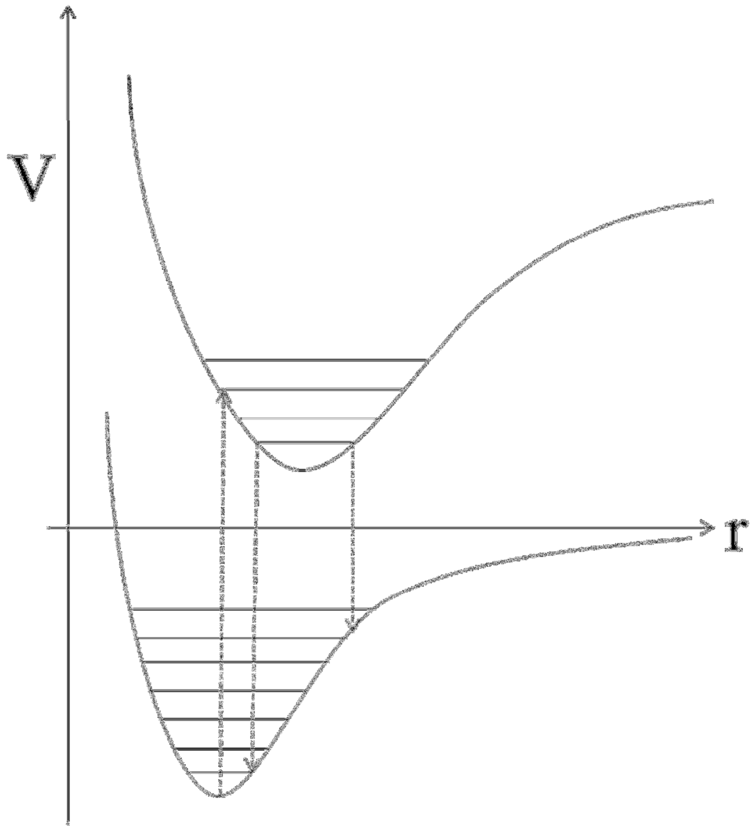

Figure 17: Franck - Condon principle

When a molecule decays to the ground state, it will emit light with energy of

$$E = hcv_{mn} \tag{3. 16}$$

v_{mn} is the wave number of the photon emitted in the transition m to n. Plasma is composed of many such molecules (amongst other species). At a given moment, a certain percentage of those will be in an excited state, governed by Maxwell Boltzmann statistics.

$$\frac{N_m}{N} = \frac{g_m exp[-E_m/kT]}{\sum_j g_j exp[-E_j/kT]} \tag{3. 17}$$

Where m is an excited state, g_m is the degeneracy of the state and T is the equilibrium temperature of the system. Assuming that light emitted from the plasma is not reabsorbed, the intensity of a spectral emission line (I_{em}) is defined as the energy emitted by the source each second. If N_n is the number of atoms in the initial state n and if A_{nm} is the fraction of those atoms that are carrying out the transition every second from n to an excited state m, then the intensity is

$$I_{em} = N_n hc v_{nm} A_{nm} \tag{3. 18}$$

where A_{nm} is the Einstein transition probability. The intensity will be proportional to N_m, while N_m is proportional to $exp[-E_m/kT]$, therefore

$$I_{nm} \propto \exp[-E_m/kT] \times A_{nm} \times \frac{hc}{\lambda_{nm}} \tag{3. 19}$$

As stated previously, the probability of emission is governed by Maxwell Boltzmann statistics. According to the Born-Oppenheimer approximation, the energy of a molecule can be represented by an electronic energy, a vibrational energy and a rotational energy

$$E_{total} = E_{rot} + E_{vib} + E_{elec} \tag{3. 20}$$

Therefore Maxwell Boltzmann statistics can be used to calculate the number of molecules in given electronic, vibrational and rotational energy levels. This is a useful tool, since the intensity of emission lines is proportional to the temperature; it is possible to estimate temperature from emission intensity. From this, an estimate of vibrational temperature has been made, due to a well resolved series of vibrational bands (the second positive system of N_2)

$$\frac{N_{v'}}{N_T} = \frac{\exp[-E_{v'}/kT_{vib}]}{q(T_{vib})} \rightarrow I_{v'v''} \propto \exp[-E_{v'}/kT_{vib}] \times A_{v'v''} \times \frac{hc}{\lambda_{v'v''}} \tag{3. 21}$$

$$\left(\frac{\lambda_{v'v''} \times I_{v'v''}}{A_{v'v''}}\right) \propto \exp[-E_{v'}/kT_{vib}] \rightarrow \ln\left(\frac{\lambda_{v'v''} \times I_{v'v''}}{A_{v'v''}}\right) \propto [-E_{v'}/kT_{vib}] \tag{3. 22}$$

By plotting a graph of $ln\left(\frac{\lambda_{v\prime v"}\times I_{v\prime v"}}{A_{v\prime v"}}\right)$ against $-E_{v'}$, one will return a straight line, the slope of which is equal to $-1/kT_{vib}$.

In theory, emission lines are often treated as being "monochromatic"; infinitely thin and having only one wavelength. Due to a number of effects, of the source and the instrument, emission lines are spread over a range of wavelengths ("broadening"). Some broadening occurs naturally. The lifetime of an excited state is governed by the uncertainty principle and is related to its energy uncertainty and therefore there is a range of emission energies. Pressure will also cause line broadening; collisions between particles will interrupt the emission process and increase the uncertainty of the emission energy, increasing the range of emission wavelengths. Broadening is also caused by instrumental effects. In order to be diffracted, light must interact with the electric and magnetic field of the optical medium. If a light source emits a perfectly monochromatic light source and if it were analysed by a "perfect" spectrometer, the output would precisely match the input. Of course, no spectrometer is perfect and thus each one will produce an apparently broadened spectral signal. The infinitely thin line will now have a finite width; this is known as the "instrumental line profile". Since any spectral structure may be considered a sum of an infinite number of single monochromatic lines at various wavelengths, there is a relationship between the instrumental line profile $P(\lambda)$, the real spectrum $B(\lambda)$, and the recorded spectrum $F(\lambda)$. The recorded spectrum is found by convolving the real spectrum with the instrumental line profile as illustrated in figure 18.

$$F = B * P \qquad \textbf{\textit{(3. 23)}}$$

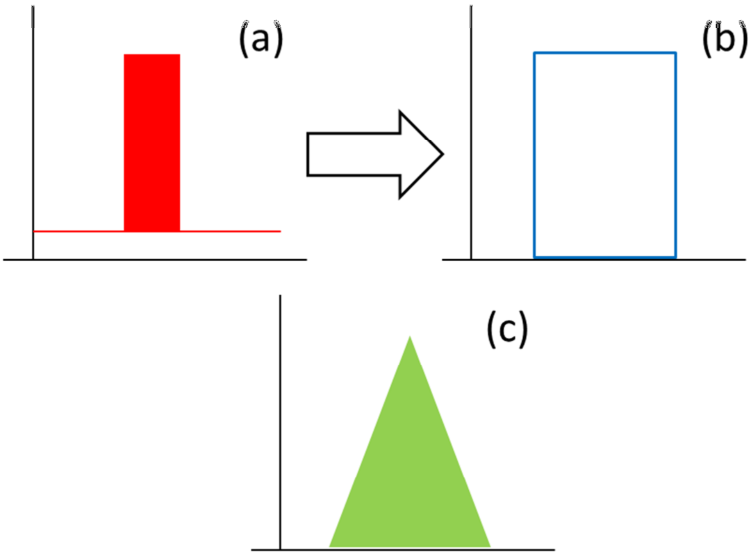

Figure 18: Convolution (a) light source (b) spectrometer instrument function (c) broadened output

The nature of a spectrometer's instrumental line function is due to several parameters including:

- The width of entrance and exit slits. In the case of this spectrometer, instead of an exit slit, the width of one pixel of the CCD detector.
- The quality of the components of the optical system and their alignment.
- Various optical aberrations and diffraction phenomena.

Each of these parameters will contribute to the instrumental line function. The overall instrumental line profile will be a convolution of the profiles of the individual terms.

$$P(\lambda) = P_1(\lambda) * P_2(\lambda) * P_3(\lambda) \ldots * P_n(\lambda) \qquad \textbf{\textit{(3. 24)}}$$

By using a sufficiently monochromatic light source (e.g. a laser or vapour lamp of known wavelength range) and comparing the output with the input, it is possible to quantify the effect of the instrumental broadening. The bandpass of the spectrometer is defined as the Full Width Half Maximum (FWHM) of this output, which the manufacturers quote as the resolution of the spectrometer. The manufacturer of the spectrometer gives a resolution of

1.5 nm for this spectrometer. Illustrated in figure 19 is the emission from a hydrogen lamp. This lamp was used to measure the bandpass of this spectrometer as 2 nm.

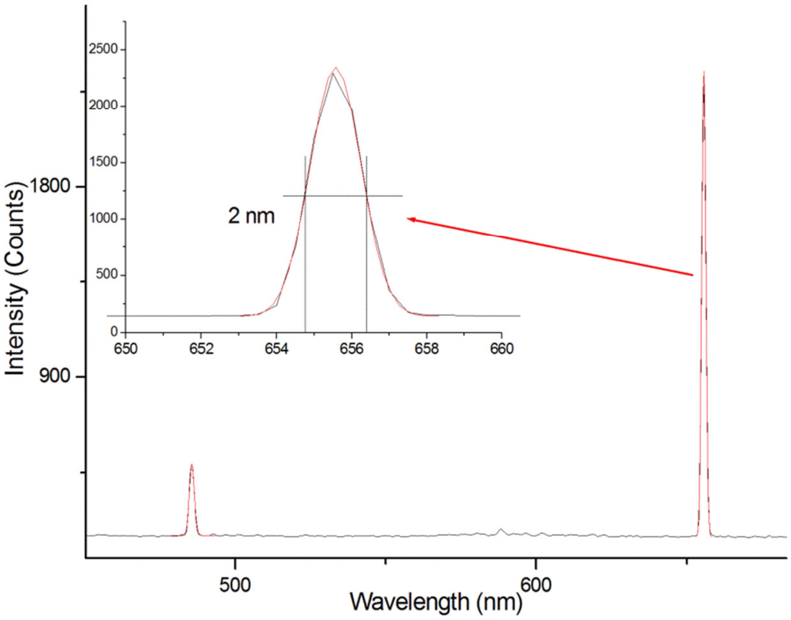

Figure 19: Gaussian fit of hydrogen lamp emission spectrum with FWHM highlighted

By measuring emission spectra with a calibrated intensity, it becomes possible to make estimates of the various temperatures of the observed plasma. To do so requires the calibration of the spectrometer against a light source of known irradiance, defined as the power of electromagnetic radiation incident upon a unit area of a surface and is measured in units of W/m^2. Irradiance should not be confused with *radiance*, a measurement of the amount of EM radiation passing through a given area and falling within a solid angle in a given direction that is measured in units of W/m^2/sr. Consider a light source that is radiating equally in all directions. It can be imagined that the radiation, as it propagates outward, passes through the surface of an imaginary sphere of a given radius. A certain amount of the power radiated from the source will pass through each unit area of the surface of the sphere. If the radius of the imaginary sphere is reduced, its surface area will also reduce; the same amount of radiation will pass through an area that is a larger proportion of the surface area of the sphere. Since the size of the detector aperture is fixed, the distance between the light source and the detector will affect the intensity of the collected light. However, if the light source - detector distance and the detector aperture area are known, it is possible to calculate the absolute intensity of the signal, if the intensity response of the spectrometer is known. Therefore, in order to calibrate the spectrometer, a light source of known irradiance is required.

A Heraeus tungsten halogen lamp with a measured irradiance profile was acquired. The irradiance profile showed the irradiance of the lamp from 250 nm to 1700 nm when operated at a voltage of 16.51 V, a current of 6.60 A in an ambient temperature of 25 ^{0}C and measured at a distance of 700 mm. This profile is illustrated in figure 20. A pinhole with an area calculated to be 2.46×10^{-7} m^2 was placed in front of the lamp to reduce the amount of light sufficiently to prevent the spectrometer from saturating. The pinhole was drilled in a piece of Teflon 5 mm thick. This meant that only light rays directly parallel with the hole passed through it, producing a collimated beam.

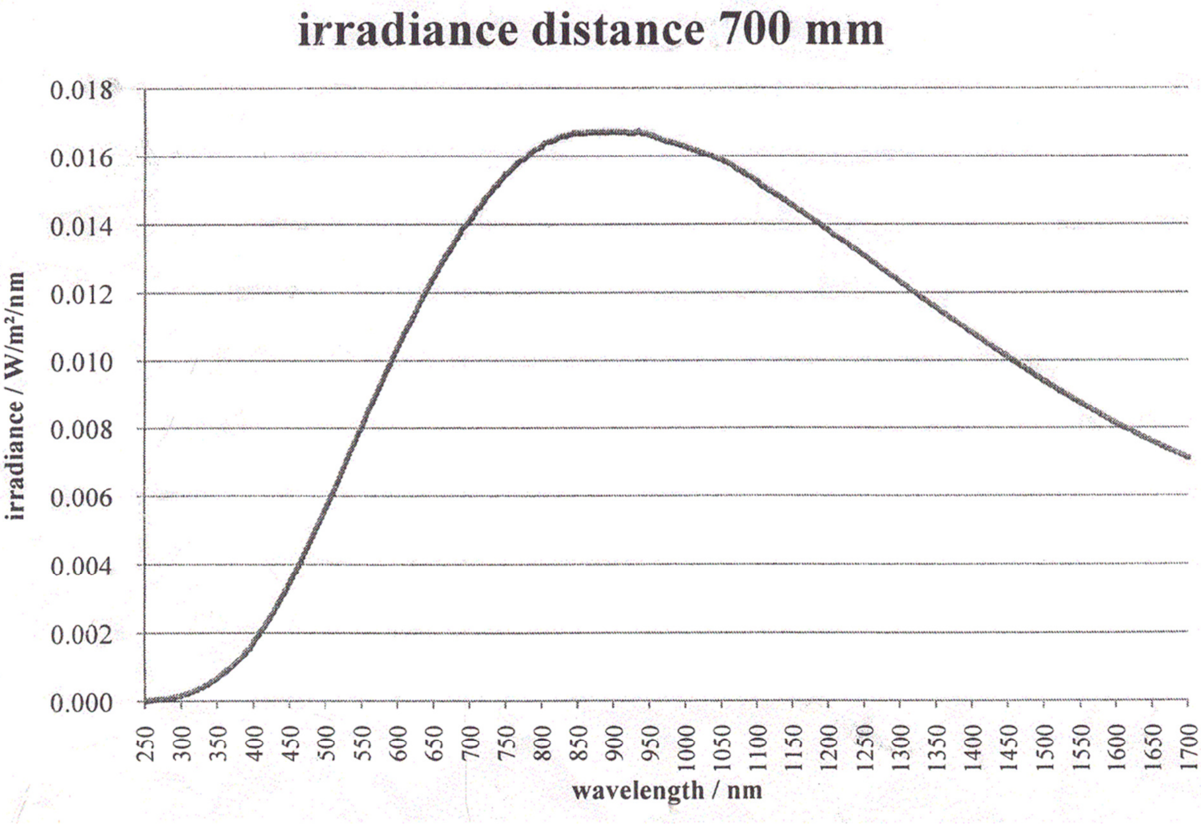

Figure 20: Intensity profile of tungsten lamp

For the purposes of analysis, some simplifying assumptions were made. The filament of the lamp was wound in the form of a thin cuboid; however it was assumed that light was emitted equally in all directions as if from a spherical source. Secondly, the material was placed immediately in front of the lamp's glass envelope and the assumption was made that the light passing through the pinhole came only from the part of the filament directly parallel with and from an area equal to that of the pinhole. Assuming that the light is emitted evenly in all directions, any point at a given distance would receive an equal amount of light. Since all the light emitted by the lamp is emitted from the surface of the filament, and since the assumption is made that only the area of the filament in direct line of sight with the pinhole and the spectrometer will be detected, it is possible to estimate the amount of energy being detected by the spectrometer. A schematic diagram of the experimental setup is illustrated in figure 21.

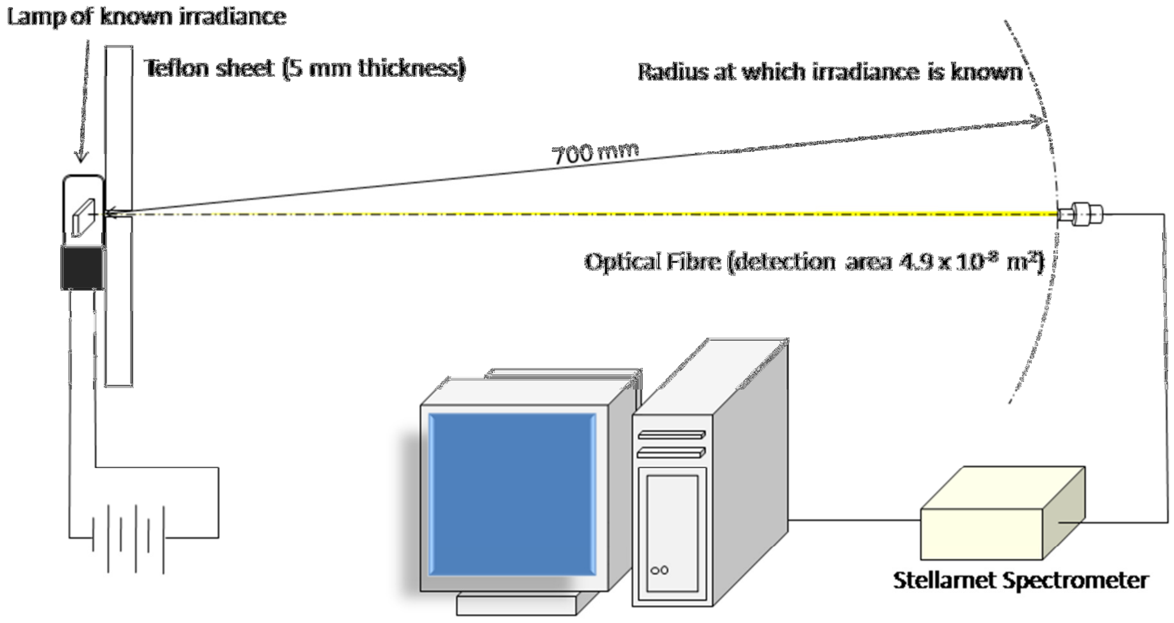

Figure 21: Diagram of setup to intensity calibrate spectrometer

It was assumed that light was emitted equally in all directions and light passing through the pinhole only came from the part of the filament directly parallel with and an area equal to that of the pinhole. If light is emitted evenly in all directions, any point at a given distance would receive an equal amount of light. Under these conditions, it is possible to estimate the amount of energy being detected by the spectrometer.

A spectrum from the lamp was captured, arbitrary units ("counts"). The result was then divided by the area of the detector (the core of the optical fibre, 4.9×10^{-8} m^2) in order to calculate the number of counts per m^2. The irradiance of the lamp was multiplied by the band pass of the spectrometer (2nm) It was then possible to draw a direct comparison between the irradiance of the lamp (in J/s/m^2) and the signal detected by the spectrometer (counts/s/m^2) and, thus, calibrate the intensity scale of the spectrometer. The irradiance of the lamp is given as a function of wavelength, since the lamp does not emit equally at all frequencies. However, the range in which the most notable featured occurred was 300 to 400 nm, and the lamp did not exhibit massive variation in this range. The response of the spectrometer at wavelength increments of 50 nm from 350 nm to 600 nm was calculated. The response in this range was found to be reasonably stable. An average was calculated from 350 nm to 600 nm. It was found that one "count" of the spectrometer was equal to an average value of $1.89\times10^{-14} \pm 0.42\times10^{-14}$ J. This is the conversion factor that was used for intensity calibrated spectrometry measurements.

The SPECAIR program outputs its results in units of mW/cm^2/sr. The steradian is the SI unit of solid angle, one steradian of a sphere of radius r is the solid angle which covers an outer surface area of r^2. In order to measure spectra in terms of steradians, one must know the area of the optical detector and the distance between the light source and the detector. In order to calculate the size of a solid angle in steradians, one uses the following formula:

$$\Omega = \frac{S}{r^2} \qquad \textbf{\textit{(3. 25)}}$$

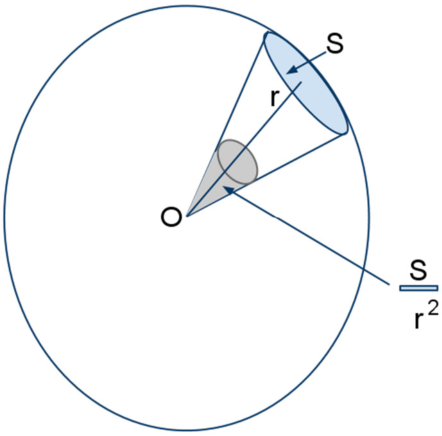

Figure 22: Diagram of Steradian

where Ω is the solid angle in steradians, S is the area enclosed by the angle and r is the radius of the sphere. To perform intensity calibrated spectroscopy, the fibre tip was placed 5 mm from the plasma. At this distance, the area of collection for the fibre (N.A. 0.22) was calculated to be 3.8×10^{-6} m. Emission spectra were recorded and imported into Origin 6.0, where the intensity scale was converted to $mW/cm^2/sr$. The intensity calibrated spectra were imported into the SPECAIR program, and visual best fit was achieved by trial and error.

III.1.e: Electrical Characterisation:

The electrical behaviour of a discharge can reveal many details as to the plasma structure and its various characteristics. This is especially true of a DBD, which has to be driven by an AC voltage signal. Observing the waveforms for voltage and current, and how they change as a function of electrode distance is a key way of determining characteristics such as the energy coupled in the plasma, charge transferred per cycle and breakdown voltage.

In order to measure voltage, a high voltage probe is utilised. High voltage probes are constructed from insulating material and feature a large resistance (several mega-Ohms) in series with the probe. Care is taken to select a suitable combination of resistances such that the probe will behave as a voltage divider. High voltage probes will have a known attenuation, for example 1000:1. Figure 23 illustrates a typical circuit set up for measurement with a high voltage probe. High Voltage probes can be designed for use with either a multimeter or an oscilloscope. A probe designed for multimeter use will be configured to return the RMS voltage, rather than the peak voltage. This should be taken into account when choosing what probe to use in a given application.

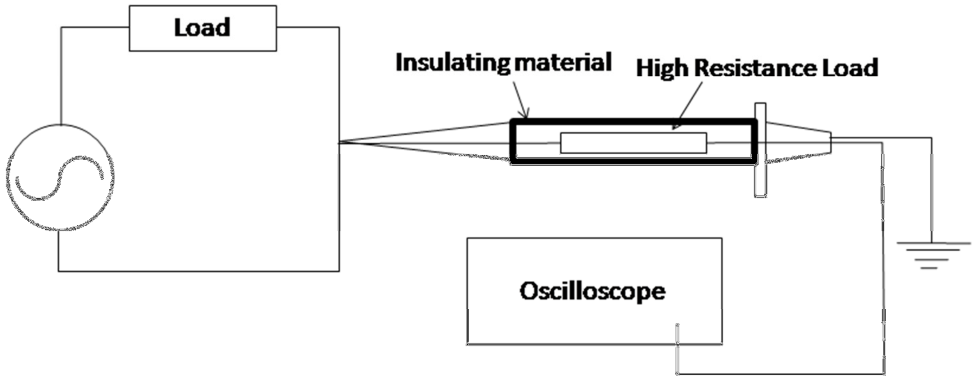

Figure 23: High Voltage Probe

Voltage was measured on circuit using Tektronix 15 kV high voltage probes. Since the system is not connected to ground, simultaneous measurements were made at both electrodes, and the difference between the voltages calculated.

In order to measure current, a current monitor is used. Current measurement can be performed using a known resistor and measuring the voltage drop across it, however, this requires inserting the resistor into the circuit and altering it. An alternate method is a current transformer, which consists of a magnetic core and secondary winding. A current carrying wire acts as the transformer's primary. The secondary is attached to an oscilloscope. As the current through the wire changes, it induces a magnetic field in the core, inducing a voltage in the secondary winding that is proportional to the primary and displayed on the oscilloscope. Figure 24 is an example of a typical current transformer set up.

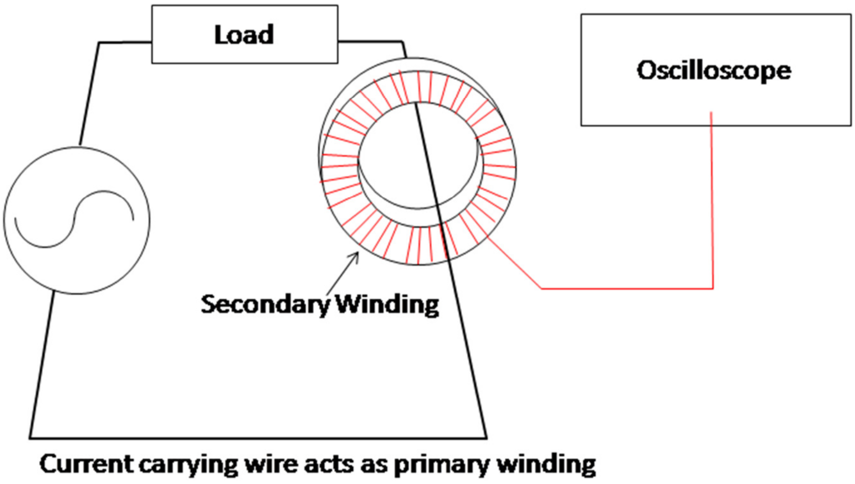

Figure 24: Current Transformer

Current measurements were performed using a Bergoz CT-E 1.0-S current monitor placed around the cable between the "bottom" electrode and the transformer.

Capacitance, the ratio of charge to voltage, requires knowledge of the charge coupled through the electrodes per cycle. It is possible to measure the charge that passes between the electrodes in a cycle, by placing a capacitor in series with the electrodes. By doing so, the capacitor stores the charge accumulated during one half cycle, and discharges it in the following half cycle. The capacitor behaves as an integrator of current. By measuring the voltage drop across the capacitor, and dividing by the capacitance, the result will be the charge that passes through the capacitor in a cycle. Figure 25 is an example of a typical charge measurement set up while figure 26 illustrates a typical Q-V plot.

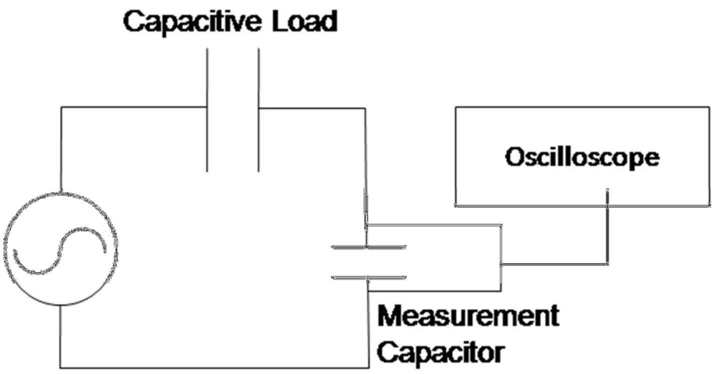

Figure 25: Charge Measurement Set up

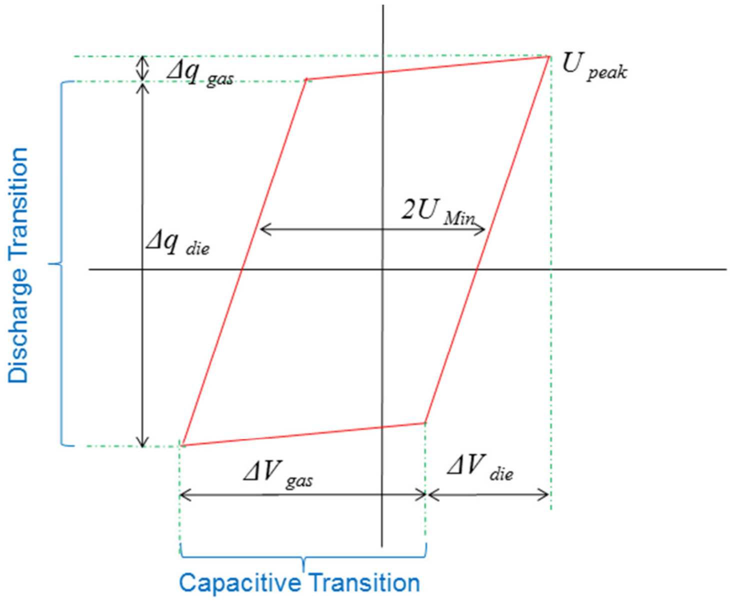

Figure 26: Lissajous Figure

Under the conditions

$$U_{gas} < |U_{peak}| \text{ and } U_{peak} < U_{Min}\frac{(C_{die}+C_{gas})}{C_{die}},$$

the cell is behaving in a purely capacitive fashion, since the voltage is not sufficient for breakdown. The plot of charge vs. voltage would be a straight line whose slope is

$$C_{cell} = \frac{(C_{dielectric} C_{gas})}{(C_{dielectric} + C_{gas})} \quad \textbf{(1. 1)}$$

When the breakdown voltage reached, the plot will become a parallelogram (a phase shift is caused by resistive losses). At this point, the Manley equations can be used:

$$u_{total} = U_{dielectric} + U_{gas} \quad \textbf{(3. 26)}$$

$$U_{dielectric} = \frac{Q_{dielectric}}{C_{dielectric}} = \frac{Q_{total}}{C_{dielectric}} \quad \textbf{(3. 27)}$$

$$U_{gas} = \frac{Q_{ges}}{C_{gas}} = U_{Min} \quad \textbf{(3. 28)}$$

Equation 3.26 states that the total voltage of the cell is made up of the voltage across the dielectric barrier and the gas. Equation 3.27 assumes that the charge on the dielectric ($Q_{dielectric}$) is equal to the total charge of the cell (Q_{total}), independent of whether the charge was capacitively or resistively coupled through the cell. Equation 3.28 assumes that the maximum value of the gas voltage will be the breakdown voltage.

$$\begin{aligned} &U_{dielectric} = \frac{Q_{total}}{C_{dielectric}} \therefore Q_{total} = (U_{dielectric})(C_{dielectric}), \\ &U_{total} = U_{dielectric} + U_{gas} \therefore U_{dielectric} = U_{total} - U_{gas}, \\ &U_{gas} = U_{Min} \quad \therefore \quad Q_{total} = (U_{total} - U_{Min})(C_{dielectric}) \end{aligned} \quad \textbf{(3. 29)}$$

Q_{cell} is represented in the Lissajous figure by the “vertical” sides of the parallelogram. The slopes of these lines are the dielectric capacitance (C_{die}). The points where these sides intercept the horizontal axis are equal to the product of $\pm C_{die}$ and U_{Min}. Since this is the case, U_{Min} can be directly measured from the Lissajous figure. If peak values are substituted into the equation for Q_{total}, the peak charge (Q_{peak}) can be calculated. This is the highest point on the Lissajous figure.

$$Q_{peak} = (U_{peak} - U_{Min})(C_{dielectric}) \quad \textbf{(3. 30)}$$

The total charge required for a transition from the positive breakdown voltage to the negative (ΔQ_{total}) can be found by

$$\Delta Q_{total} = 2 C_{gas} U_{\min} \quad \textbf{(3. 31)}$$

Also

$$2Q_{peak} = \Delta Q_{dielectric} + \Delta Q_{total} \tag{3. 32}$$

By substituting equations (3.30) and (3.31) into (3.32) the following is obtained

$$\Delta Q_d = 2C_d \left[U_{peak} - \left[\frac{C_{die} + C_{gas}}{C_{die}} \right] U_{Min} \right] \tag{3. 33}$$

Since $W = qV$, the energy that is deposited into the gas in a full cycle is

$$W = 2\Delta Q_{die} U_{Min} \tag{3. 34}$$

Substituting equation (3.33) into equation (3.34) returns

$$w = 4U_{Min} C_{die} \left[U_{peak} - \left[\frac{C_{die} + C_{gas}}{C_{die}} \right] U_{Min} \right] \tag{3. 35}$$

The mean power of the system can be found by multiplying the mean energy by the frequency. To perform Q-V measurements, three high voltage capacitors were places in series. The total capacitance of this set up was measured to be 2.2 nF. High voltage probes were placed on either side of the capacitors and the voltage drop across them was measured. Measurements of voltage, current and charge were made with one of two Tektronix TDS series oscilloscopes and saved on to floppy disk or memory stick. It is important to measure characteristics simultaneously, as phase information is not conserved otherwise. When measuring voltage and charge, signals were averaged over 512 samples. However, current traces were not averaged, due to the randomness of microdischarge peaks.

III.2: ZnO Thin Films Experiment

III.2.a: PLD Description:

ZnO thin films were deposited on PMMA (Perspex) and Kapton substrates using the Pulsed Laser Deposition (PLD) system described herein. The system consists of a Powerlite Q-Switched Nd:YAG laser, with a fundamental output wavelength of 1064 nm (IR) that is frequency quadrupled to produce a final output wavelength of 266 nm (UV). The laser is pulsed at a frequency of 10 Hz and pulse duration of 6 ns. The specifications of the Powerlite 1080 are given in table 5 and the internal layout of the laser is illustrated in figure 27. An Nd:YAG crystal consists of an yttrium aluminium garnet crystal (the YAG) that is doped with triply ionised neodymium (Nd III). Neodymium is used because its ions are approximately the same size as yttrium ions (radii differ by ≈3%), and so it replaces a small fraction of them (1%). The utility of this material as a lasing medium was first demonstrated by J.E. Geuset *et al* in 1964 (1964). Nd:YAG possesses several featured that make it suitable as a lasing material: it is hard (8-8.5 on Mohs scale), has excellent optical clarity (Koechner and Bass 2003) and has a high thermal conductivity (0.14 $W{\cdot}cm^{-1}{\cdot}K^{-1}$).

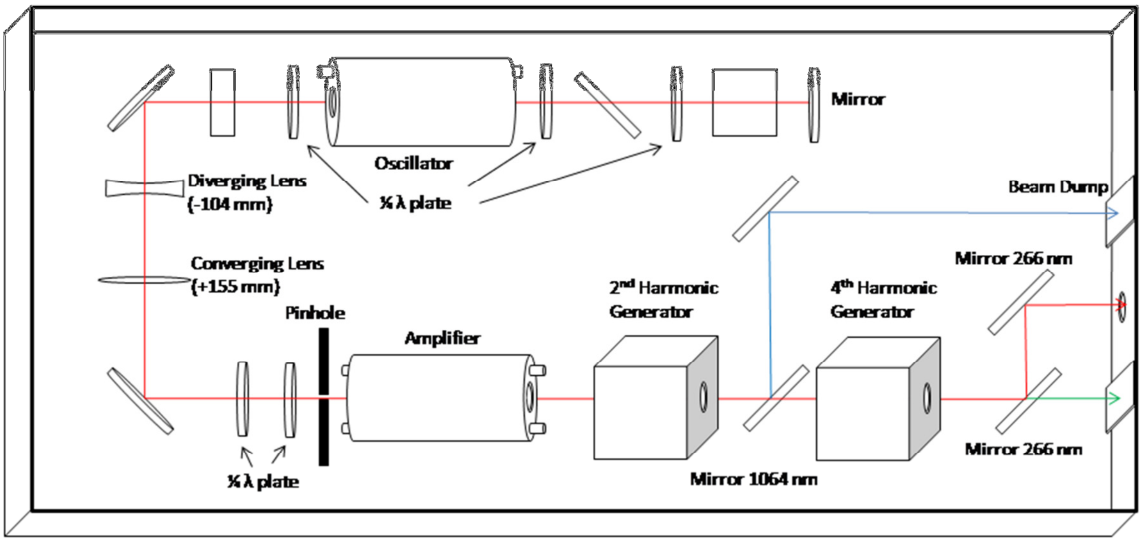

Figure 27: Internal optics of Powerlite 1080 Nd: YAG laser

Table 5: Powerlite 1080 Specifications

Energy (λ=266 nm)	**Pulse Width (ns)**	**Linewidth (cm^{-1})**	**Divergence (mrad)**	**Beam Diameter (mm)**
150 mJ	5 – 7	1	0.45	9

The laser light is directed, via a system of mirrors, into a choice of two high vacuum systems; both consisting of a stainless steel, spherical vacuum chamber with a diameter of 45.72 cm (with adjacent load-lock chamber) evacuated by a turbo pump. The base pressure of the first chamber is around $3{\times}10^{-8}$ mBar while the second chamber has a base pressure of 2×10^{-8} Torr ($2.6{\times}10^{-11}$ mBar). Each chamber contains a motorised carousel on which a selection of up to 6 targets can be mounted, oriented such that the laser light is incident upon them. The laser light is focussed to a point on the surface of the target, resulting in a fluence of 2.0 J cm^{-1}.

A plume of plasma is formed at the surface of the target, which propagates outward and is incident upon the sample. The distance between the target and the sample is 55 mm. Oxygen is introduced as a process gas. In the first chamber, the oxygen level is controlled manually, by means of a flow meter. In the second chamber, mass flow controllers automatically monitor and control the oxygen pressure. A schematic representation of the PLD chambers is shown in figures 28 and 29 respectively.

Depositions were performed on Perspex substrates measuring 5 mm×20 mm and on Kapton substrates measuring 20 mm×25 mm. Substrates were washed in isopropyl alcohol (IPA) in an ultrasonic bath for 15 minutes and rinsed in de ionised water. They were fixed to the sample holder using a bead of vacuum grease when no heat treatment was to be applied, and a bead of silver paste when heat was used. When silver paste was used, samples were cured on a hot plate at 100 degrees for 10 minutes. Depositions were performed primarily at 5,000, 10,000 and 20,000 laser shots, while a small number of samples were grown at 40,000, 60,000 and 80,000 laser shots. During deposition, oxygen pressure was maintained at pressures of 1, 10, 30 mTorr for “low pressure” depositions and at 75, 150 and 300 mTorr for “high pressure” depositions. Depositions were performed with a nominally undoped zinc oxide (ZnO) target, ZnO targets with 2% aluminium doping (by weight) and an Mg 0.25 ZnO 0.75 alloyed target.

Samples were characterised using X-ray diffraction (XRD), atomic force microscopy (AFM), Van der Pauw resistance measurements and water contact angle (WCA) measurements. In order to estimate the relation between the number of shots on the deposition and the film thickness, some samples were partially masked during deposition, and their thickness measured using a profilometer. Samples were then given to colleagues in the DCU School of Biotechnology, who grew electroactive biofilms upon them and measured their electrical output using chronoamperometry (CA) and cyclic voltammetry (CV).

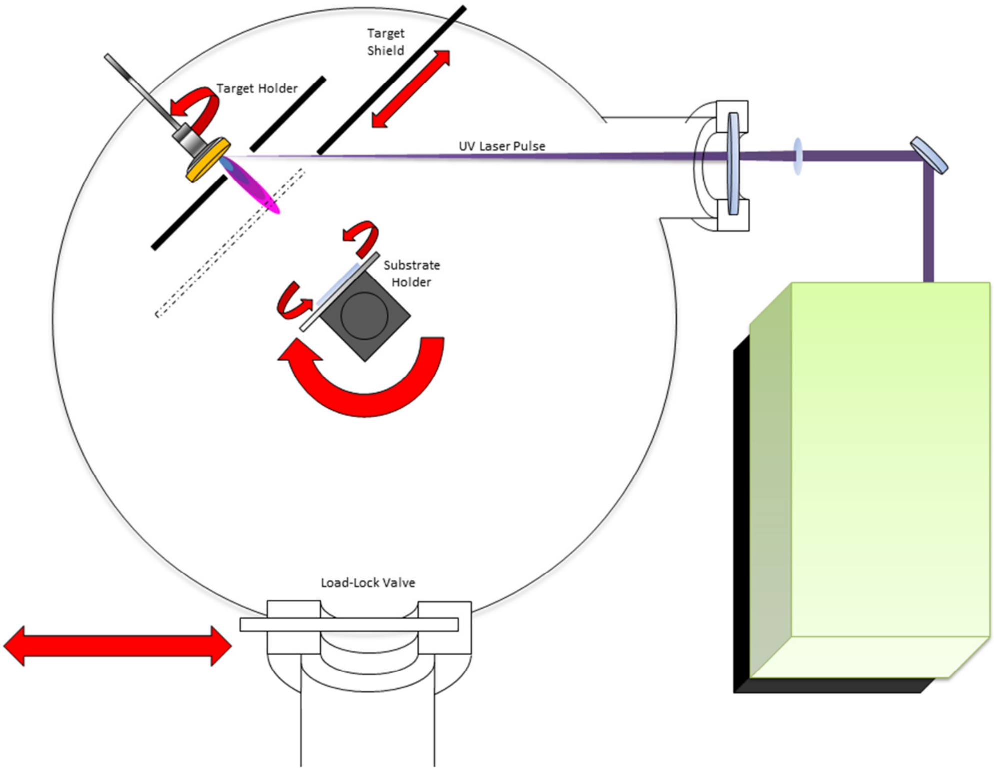

Figure 28: Diagram of Pulsed Laser Deposition Set-up in first chamber

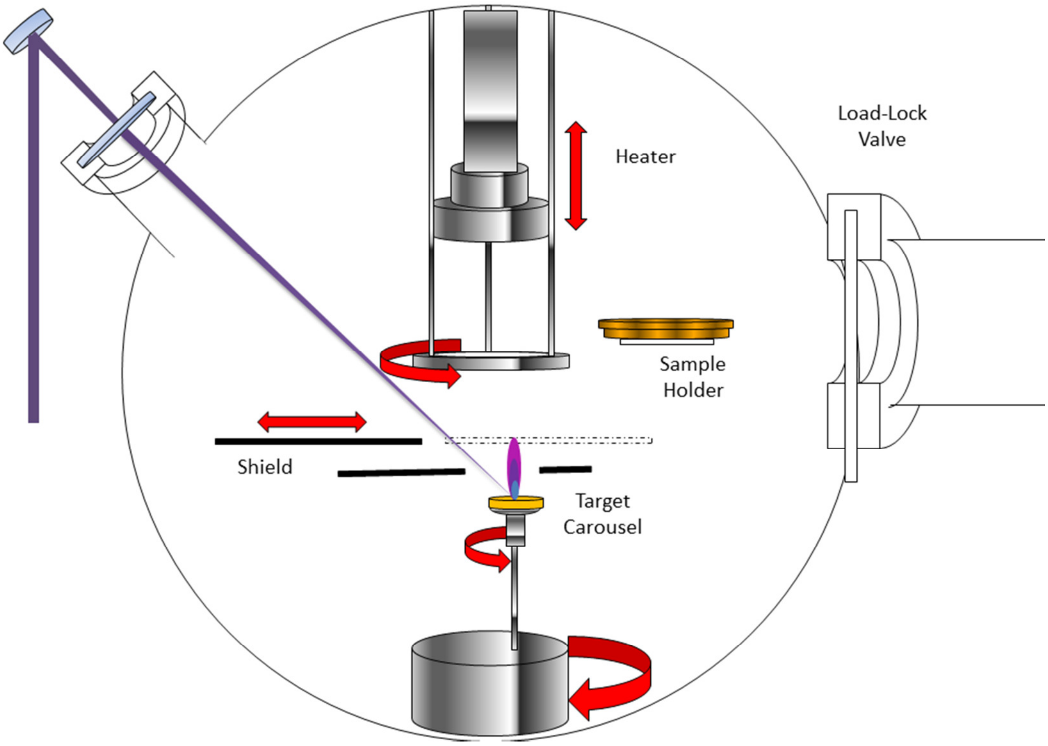

Figure 29: Diagram of Pulsed Laser Deposition Set-up in second chamber

III.2.b: X-ray Diffraction:

X-ray diffraction is a technique to investigate the arrangement of atoms within crystals. X-ray diffraction was pioneered by the father and son William Henry Bragg and William Lawrence Bragg (Perutz 2012). There are several methods of X-ray diffraction, some of which utilise *elastic* collisions (where the scattered X-ray wavelength is the same as the incoming X-ray wavelength) and others which employ *inelastic* collisions (incoming and scattered X-rays have different wavelengths). This description will focus on X-ray diffraction performed upon a solid crystal sample utilising elastic collisions. A diagram of X-ray diffraction is shown in figure 30.

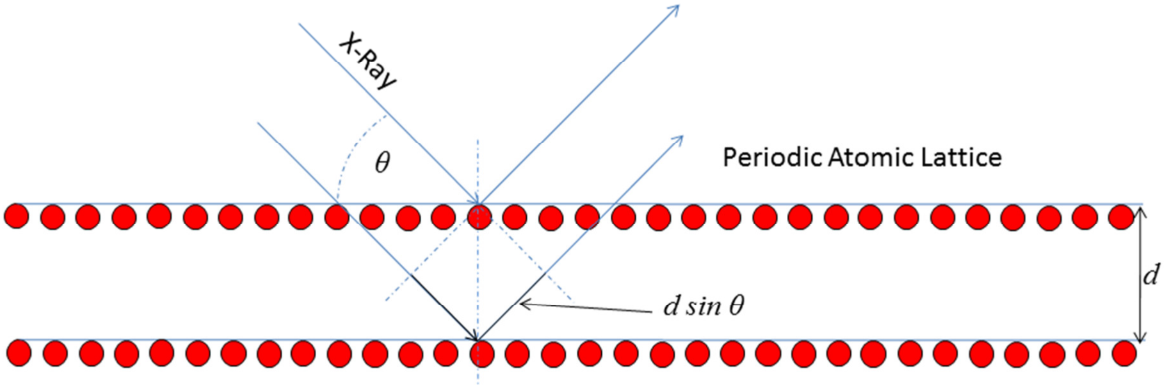

Figure 30: Diagram of Principle of X-ray Diffraction

A sample of the material under investigation is illuminated with X-rays. If the sample has a crystal structure, the X-rays will be diffracted in such a fashion as to cause constructive and destructive interference by the periodic structure to form a diffraction pattern. X-rays will be scattered from the atoms in accordance with the Bragg Equation:

$$n\lambda = 2d\sin\theta \qquad \textbf{\textit{(3. 36)}}$$

By measuring the angle of diffraction, it is possible to calculate “d”, the inter-atomic distance. Analysis of the pattern will yield information on the density of electrons, from which the mean position of the atoms can be inferred. An amorphous structure will scatter the X-rays randomly, leading to destructive interference which won’t form a diffraction pattern. A typical X-ray diffraction apparatus, consists of an X-ray detector mounted on a goniometer, which can move along the arc of a circle, at the centre of which is the sample. The sample will be illuminated by X-rays and will scatter them at certain angles, dependent on its crystal structure. The detector can move in an arc around the samples and will detect the increase in X-ray radiation at the scattered angles. The intensity of the X-ray radiation is recorded and plotted as a function of angle. It is possible, on sophisticated models, for the sample to be rotated in multiple axes, allowing for elucidation of the structure in multiple dimensions.

In laboratory XRD equipment, X-rays are generated by focussing a beam of electrons upon a target. The electrons are absorbed by the target and decelerate, releasing energy in the form of X-ray photons, in a process known as *Bremsstrahlung* (braking) radiation. Copper (Cu) and molybdenum (Mo) are commonly used target materials with photon wavelengths of 0.154 nm and 0.08 nm respectively. (Materials Research Laboratory at University of California, Santa Barbara n.d.). The K-alpha emission line is utilised. K-alpha lines result when an electron from the 2p shell transitions to the 1s shell. Because there are two possible spin configurations in the 2p shell (1/2 and 3/2), the K-alpha line is a doublet. The K-alpha lines are generally the strongest X-ray emissions. When X-rays are generated, they are passed through a slit to create a collimated beam. In order to fully interrogate the sample, it is rotated under the X-ray beam by an angle theta (θ) while the detector is moved through an angle of two theta (2θ). The θ-2θ arrangement is shown in figure 31.

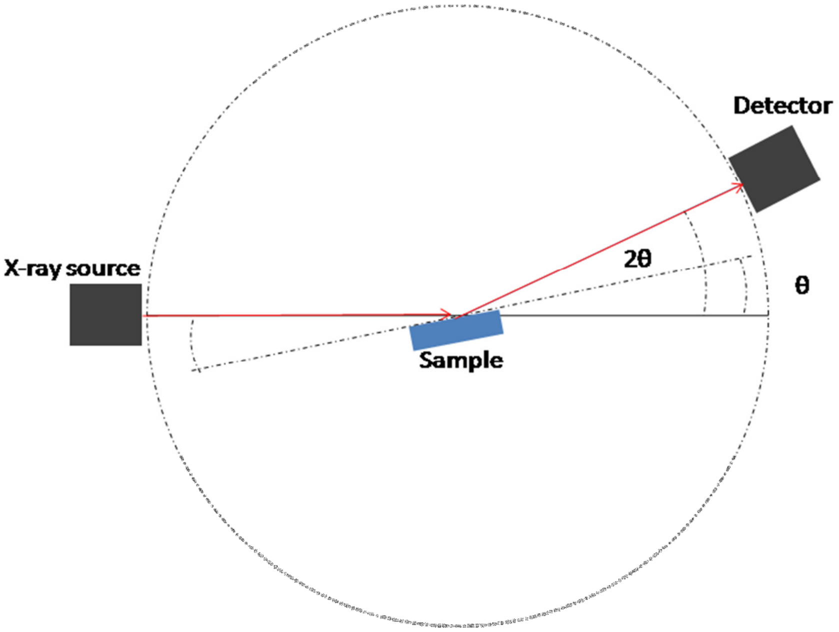

Figure 31: Diagram of (ϑ - 2ϑ) X-ray diffraction arrangement

X-ray diffraction was performed using a Bruker D8 Advance model diffractometer. This model uses a Bruker/Siemens KFL Cu 2K X-ray source. Gobel mirrors are used to reflect and direct the X-ray beam and a scintillation counter acts as an X-ray detector. Zinc oxide has a wurtzite crystal structure and is generally oriented along the c-axis on most substrates. Perspex and Kapton offer an advantage when performing XRD due to being amorphous; any observed peaks must be due to the deposited film. X-ray Diffraction was performed on samples between 15^{o} and 80^{o}. Scans were performed in increments of 0.05^{o}.

III.2.c: Atomic Force Microscopy:

Atomic force microscopy (AFM) is an imaging technique that can characterise the surface topography of a sample down to the atomic scale. A hollow cylinder of piezo-material is fabricated to serve as a mounting for an AFM tip. Four electrodes are placed on its outer surface at points 90^{o} apart, and one on the inside surface. By applying a voltage between these electrodes, the tube can be made to move in any direction, illustrated in figure 32.

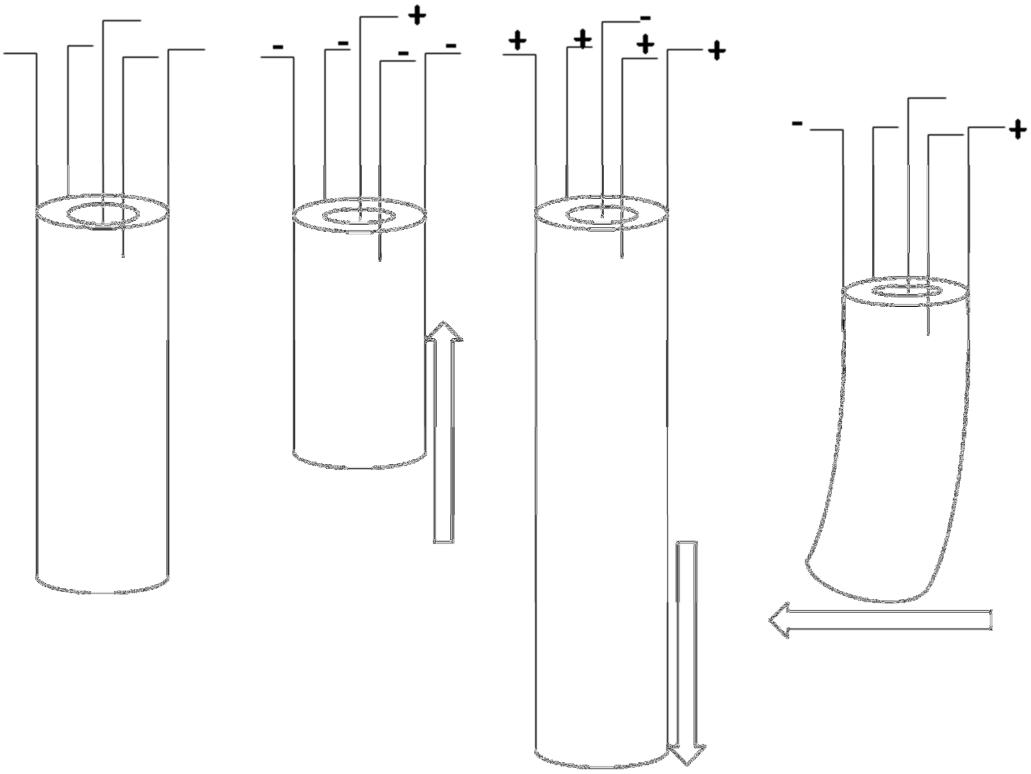

Figure 32: AFM Piezo tube control

The AFM tip is usually manufactured from Silicon Nitride ($N_4\ Si_3$) with optical lithographic techniques and has an extremely narrow, pointed end, tens of nanometres in diameter, to maximise resolution. The tip is fabricated on one end of a long narrow cantilever, in the range 140 – 180 µm which usually has a resonant frequency in the 100 – 500 kHz range (Geissib 2003).

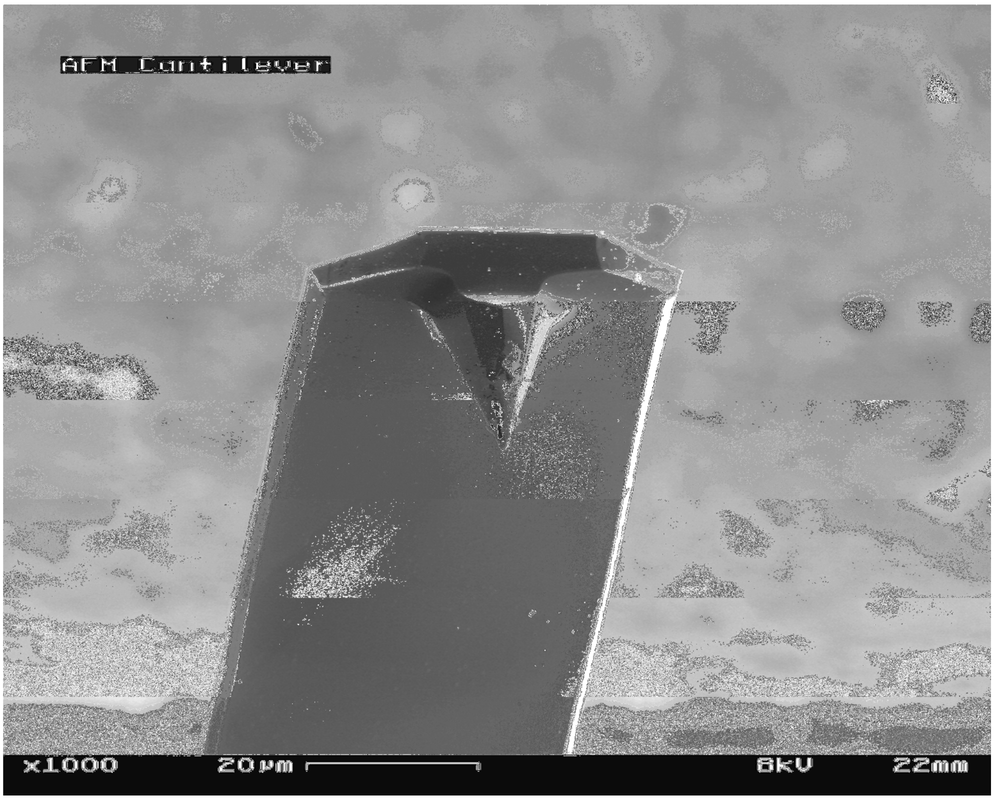

Figure 33: SEM image of AFM tip

Tip deflection can be measured optically (preferred method) or electrically (less common). A typical optical deflection system is displayed in figure 34 and consists of a laser beam which illuminates the back of the cantilever and is reflected into a quadrant photodiode. As the tip is tracked over the sample surface, interaction with the surface causes it to be deflected minutely which causes a large deflection in the laser, detected by the quadrant photodiode. The difference in the position of the laser on the diode is used to calculate the surface topography. The cantilever setup is ideal for AFM; it is rigid in two axes of motion, but flexible in the third and will only detect deflections that are normal to the sample surface, dampening out stray vibrations.

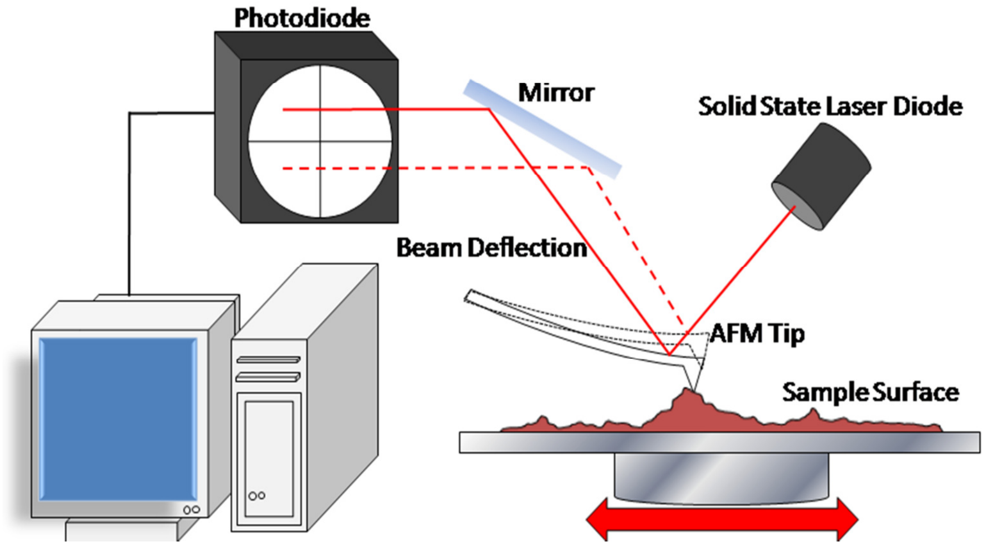

Figure 34: Diagram of Atomic Force Microscope Set up

The amount by which the tip will be deflected is proportional to its spring constant (k) which can be found from (Geissib 2003)

$$k = \frac{Y\omega t^3}{4L^3} \tag{3. 37}$$

where ω is the width, t is the thickness, L is the length of the cantilever and Y is Young's Modulus of the cantilever material. The resonant frequency of the cantilever can be found from (Geissib 2003):

$$f_0 = 0.162\frac{t}{L^2}\sqrt{\frac{Y}{\rho}} \tag{3. 38}$$

where ρ is the mass density of the cantilever material. The resonant frequency is an important characteristic when using the AFM in non-contact mode, which will be described in more detail later.

AFM can be performed with the tip touching with the surface (contact mode), or positioned immediately above it (non-contact and tapping modes). In contact mode, a "soft" tip that has a lower spring constant and is more sensitive to minute deflections is utilised. The tip should have a spring constant that is less than the inter-atomic spring constant of atoms in a solid (< 10 N/m) and are generally between 0.01 – 5 N/m (Geissib 2003). As the tip is brought into near-contact with, and tracked across the surface, the force between the tip and the sample ($F_{tip\text{-}sample}$) is measured. The tip height (z) is varied to keep $F_{tip\text{-}sample}$ constant. Using the AFM in non-contact mode, a stiffer tip, with a higher k value is used; the tip is maintained above the sample and is forced to resonate (vibrate or oscillate) at a frequency slightly below (or above) its natural resonance frequency. The long range Van der Waals forces, typically act in the range of 1 - 10 nm from the surface and play a dominant role in non-contact mode. These forces decrease the resonance frequency of the tip. In non-contact mode, the tip is either kept at the same distance and the change in deflection measured, or the tip is moved so that the deflection remains the same, and the change in height measured. Using the AFM in non-contact mode is essential for the study particles on the surface of a sample or a coating that has been applied to a surface.

In tapping mode, the tip oscillates with much greater amplitude than non-contact mode and is periodically brought into contact with the surface. Interaction with the surface through the Van der Waals forces causes a reduction in the tip oscillation amplitude, changing the deflection of the tip which is measured by the photodiode. Tapping mode reduces the damage done to the tip and sample during measurement, however measurements take longer to perform.

AFM was performed using a Digital Instruments Veeco Dimension 3100. In these experiments, the AFM was used in Tapping mode. A silicon tip with a length of 160 ± 20 µm and width of 50 ± 2 µm was utilised. The specifications of this tip are given in table 6

Table 6: AFM tip specifications

Tip Height (h):	7 - 15µm
Front Angle (FA):	0 ± 1º
Back Angle (BA):	35 ±1º
Side Angle (SA):	35 ±1º
Tip Radius (Nom):	7nm
Tip Radius (Max):	10nm

This tip has a resonance frequency (f_0) of 315 ± 34 kHz. Images were taken over areas of 6 µm×6 µm, 30 µm×30 µm and 100 µm×100 µm on each sample. Images were taken at a setting of 512 samples per line. Scan speed was varied to ensure the best image for each sample. AFM images were investigated using the software package “Wsxm” which is available for free to download from the internet (Horcas, et al. 2007).

III.2.d: Van der Pauw resistivity measurement:

Four point probe measurement is a method of accurately measuring small electrical resistances. Four point probe measurement offers improvements in accuracy over measurement with two terminals; by using separate pairs of terminals to carry current and sense voltage, the impedance contribution of the wires themselves is eliminated.

To measure resistance with two terminals, the terminals are connected to the material under investigation and a current (the *force current*) applied. The voltage drop between the terminals is measured, however there is a voltage drop between the wires themselves which is also detected and adds error to the measurement. In order to eliminate this as a source of error, four point probe measurement uses a second set of terminals (through which no current is passed) to measure the voltage drop. By isolating the terminals that supply the current from the terminals that measure the voltage, the error due to the internal resistance is eliminated.

The Van der Pauw method is a refinement of four terminal sensing. It is a technique used to measure several thin film characteristics; among them sheet resistance (and thus the bulk resistivity), the mobility of the sample and whether the sample is “p” or “n” type. The technique was developed by Leo J Van der Pauw and reported in 1958 (van der Pauw 1958). For the technique to be applied successfully:

- The contacts are placed at the circumference of the sample
- The contacts are sufficiently small compared to the sample, by at least an order of magnitude
- The sample is uniformly thick
- The surface of the sample is singly connected, without holes

Consider a flat sample of arbitrary shape to which have been fixed four electrical contacts A, B, C and D. Such an arrangement is presented in figure 35. The resistance $R_{AB,CD}$ is defined as the potential difference $V_D - V_C$ between the contacts D and C per unit current through the contacts A and B. Similarly, the resistance $R_{BC,DA}$ is the potential difference $V_A - V_D$

between A and D per unit current through B and C. Van der Pauw shows that the following relationship holds:

$$\exp(-\pi R_{AB,CD}\, d/\rho)+\exp(-\pi R_{BC,DA}\, d/\rho)=1 \tag{3. 39}$$

where ρ is the resistivity of the sample and $d$is the sample thickness (van der Pauw 1958). Van der Pauw realised that, to measure the resistivity of a flat sample, all that was required is the resistances $R_{AB,CD}$ and $R_{BC,DA}$ (van der Pauw 1958)

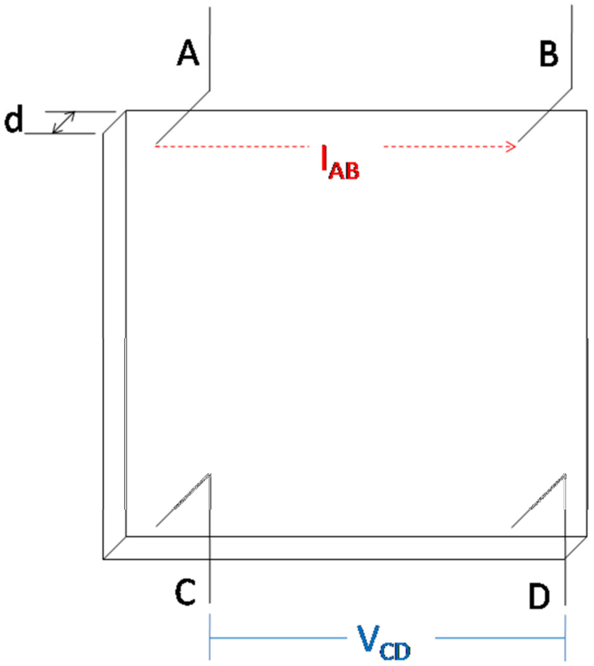

Figure 35: Diagram of Four Pont Probe terminals

To perform a measurement, a current is passed between two contacts (i.e. A and B), and a voltage is measured between the other two (i.e. C and D). These values are used to calculate a resistance using Ohm’s Law. Accuracy can be improved by reversing the polarity for each pair, and recording two more measurements. Because of the reciprocity theorem

$$R_{AB,CD}=R_{CD,AB} \tag{3. 40}$$

by repeating measurements with the pairs reversed (current through C and D, voltage across A and B) and averaging over four measurements, accuracy is improved. By making measurements of sheet resistance (expressed in Ohms (Ω)) and multiplying by the sample thickness (expressed in cm), it is possible to calculate the resistivity of the sample (in Ωcm).

In this work, Van der Pauw resistivity measurements were performed using an Accent HL 550 PC Hall Effect measurement instrument. For greater precision, each measurement was performed at a series of measurement currents, starting at 1 pA and increasing by a factor of ten until measurement failure. Samples have a surface area of 1 cm^2.

III.2.e Profilometry:

Film thickness and surface roughness are important. There are a variety of methods to perform these measurements, some of which require physical contact with the surface, others which are dependent on various optical techniques (change in focus, change in intensity etc.). A typical contact profilometer setup is shown in figure 36, and consists of a stylus that can be moved in the X, Y and Z axes with millimetre precision. The stylus is positioned over a horizontal plate on which samples are placed. The stylus is generally manipulated via computer and its position on the sample observed with a camera focused on the surface. The stylus is brought in contact with the surface in question, and then moved laterally across the surface, measuring changes in vertical position as a function of horizontal position. This information is recorded and used to plot a profile of the surface. To return accurate measurements, a profilometer must be able to detect very fine changes in height, at the nanometre scale. A Dektak 150 surface profilometer was used in these experiments.

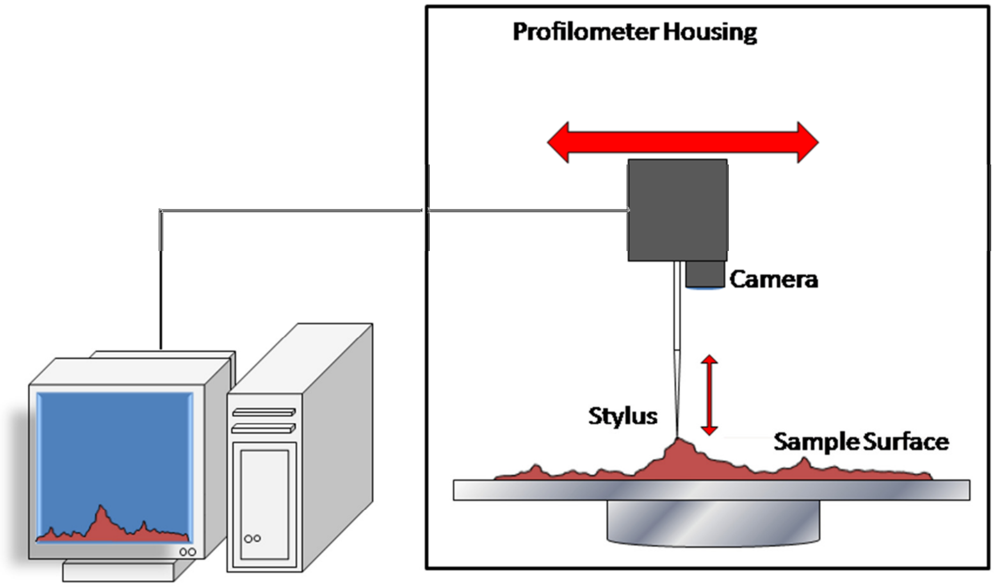

Figure 36: Diagram Schematic Principle of Profilometer Set up

III.2.f: Water Contact Angle:

Water contact angle measurements were performed using a First Ten Ängstroms FTA 200 water contact angle measurement apparatus using FTA 32 software. A schematic diagram of the set up used to perform WCA measurements is illustrated in figure 37. The manufacturers claim that water contact angle measurements have a standard deviation of less than one degree. The syringe that deposits water droplets is computer controlled and can be set to a flow rate between 0.05 – 125 µL/s. Flow rates of between 3 and 4 µL/s we used. The syringe needle tip was placed between 5 and 12 mm from the film surface. Multiple measurements were performed on each sample for accuracy and to investigate film uniformity. No less than five measurements were aken and averaged on any given sample, and between ten and fifteen measurements were frequently made. After measurements were completed, water droplets were removed by blotting the surface of the film with an absorbent wipe. Water Contact Angle (WCA) measurements were performed as soon as possible after deposition to minimise error due to dust particles and surface damage to the film. Films were kept wrapped in lens tissue and stored in styrene sample cases for protection.

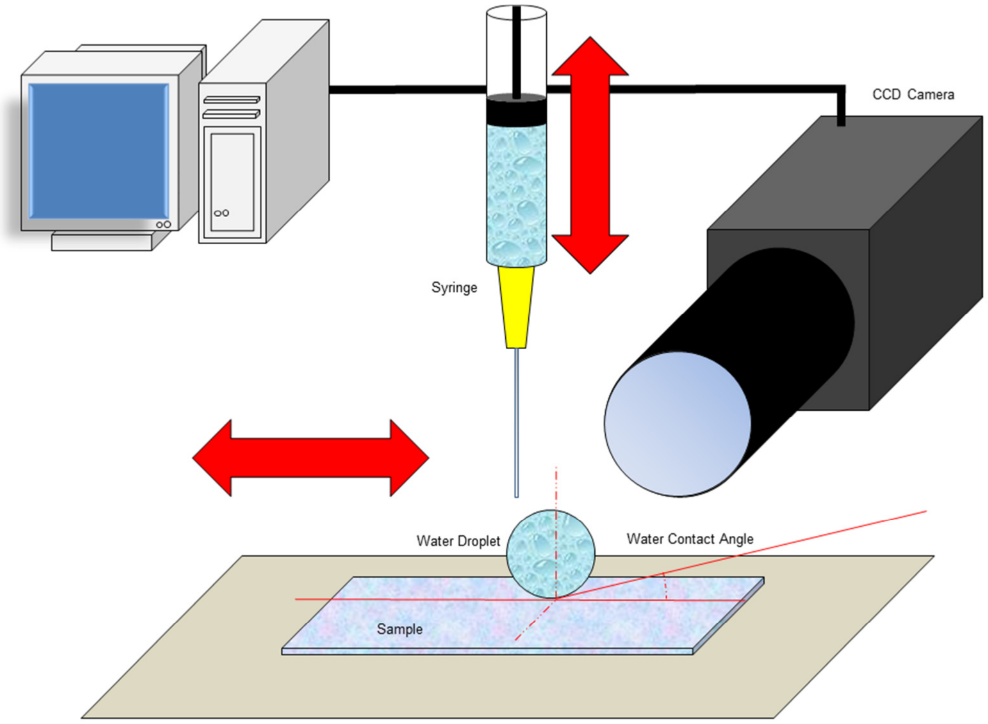

Figure 37: Diagram of Water Contact Angle Set up

III.2.g: Bacterial Preparation:

Biofilms were grown upon transparent zinc oxide film by our colleagues in the DCU school of Biotechnology. The gram positive bacteria *Geobacter Sulfurreducens* was initially cultured in large batches in a solution of iron chloride and deionised water, to which was added nutrients and a buffer. This solution causes the bacteria to grow slowly. As *G. sulfurreducens* was required for biofilm growth, samples were taken from this culture and placed in a solution of fumeric acid, sodium acetate, deionised water and carbon dioxide, which promotes speedier growth. The pH of both solutions is 6.8. The cultures were kept at a temperature of 30 ^{0}C. It should be noted that *G. sulfurreducens* is an anaerobic bacteria, and any exposure to oxygen is lethal.

The gram negative bacteria *E.coli* was cultured in a solution of glucose and deionised water and exposed to atmospheric oxygen by agitating the solution to aerate it. This culture was also kept at 30 ^{0}C and had a pH of 7.

Shewanella loihica was initially cultured in a medium consisting of proteins, yeast extract, salt and deionised water which has a pH of 7.2. This medium is autoclaved to sterilise, and then 2 ml of 1 mol/litre of magnesium sulfate ($Mg\ SO_4$) and 0.1 ml of 1 mol/litre calcium chlorate ($CaCl_2$) is added. When grown in the electrochemical cell (ECC) a growth medium composed of the following was used:

- 500 ml distilled water
- 2.5 g $NaHCO_3$ (sodium carbonate)
- 0.08 g $CaCl_2.2H_2O$ (calcium chloride dihydrate)
- 1 g NH_4Cl (ammonium chloride)
- 0.2 g $MgCl_2.6H_2O$ (magnesium chloride hexahydrate)
- 10 g NaCl (salt)
- 7.2 g HEPES (buffer, a substance added to keep pH constant)
- 0.5 g yeast extract
- 10 ml trace minerals
- 1 ml vitamin solution
- Iron citrate 4.92 g (electron acceptor)
- Lactic acid 0.77 ml (electron donor)

This mixture was diluted with distilled water to bring the volume to 1 L. Sodium hydroxide (NaOH) was added to bring the pH to 7.6 and the mixture autoclaved. 0.05% of casamino acids (substances that would be destroyed by autoclave) were then added.

III.2.h: Bacterial Electrical Characterisation:

Bacterial electrical characterisation was performed by our colleagues in the DCU School of Biotechnology. Chronoamperometry (CA) is an analytical technique for elucidating the electrochemical behaviour of biofilms. A working electrode on which the film is grown is subjected to a potential and the current density output is recorded. The potential is kept constant over a period of several hours and the change in current density recorded as a function of time. It is important that the analysis is conducted over a broad time interval (several hours) to ensure that the results are reliable.

Cyclic Voltammetry (CV) is another analytical tool for understanding the electrochemical behaviour of biofilms. The potential is stepped up incrementally and the current density recorded as a function of applied potential. A three electrode system of measurement is widely utilised for both CA and CV measurements. The circuit diagram for such a system is illustrated in figure 38. This system consists of a working electrode, a reference electrode and an auxiliary electrode. Potential is applied to the working electrode, measured through the reference electrode while the circuit is completed by the auxiliary electrode. The electrical potential of reference does not change easily during measurement (Avci 2007, 29). The experiments are performed by a potentiostat that controls the potential applied between the reference and working electrodes, while the current is measured through the auxiliary electrode. A diagram of the potentiostat is provided in figure 39.

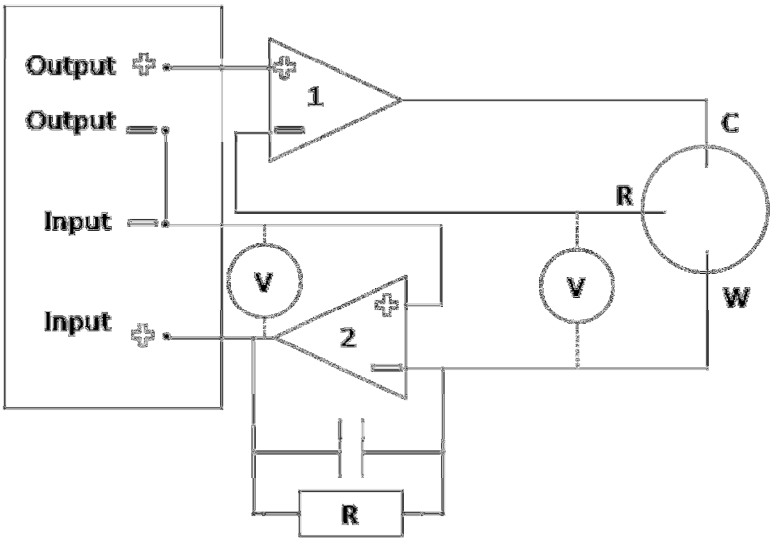

Figure 38: Schematic circuit diagram for performing CA and CV measurements

Platinum wires from the working electrode were inserted into heat-pulled 3-mm glass capillary tubes and soldered inside the capillary to copper wires. Counter electrodes consisting of a 0.1-mm-diameter platinum wire were inserted into a 3-mm glass capillary and soldered to a copper wire.

Reference electrodes were connected to bioreactors via a salt bridge assembled from a 3-mm glass capillary and a 3-mm Vycor frit. Electrode capillaries were inserted through ports in a custom-made Teflon lid sealed with an O ring. This fits onto a 20-ml conical electrochemical cell, which was washed in nitric acid (HNO_3). A small magnetic stir bar was inserted and the cell autoclaved for 15 min. The salt bridge was then filled with 0.1 Mol/litre of Sodium sulphate (Na_2SO_4) in 1% agar. A saturated calomel reference electrode (Fisher Scientific, Pittsburgh, PA) was placed at the top of this agar layer and covered in additional Na2SO4 to ensure electrical contact. The reactors were placed in an in-house-built water bath to maintain cells at 30°C.

To maintain the strict anaerobic conditions required by *Geobacter* bacteria, all reactors were operated under a constant flow of sterile humidified N2-CO2 (80:20 [vol/vol]), which has been passed over a heated copper column to remove trace Oxygen. Each reactor was located above an independent magnetic stirring unit. Autoclaved bioreactors flushed free of oxygen, filled with sterile growth medium, and incubated at 30°C were analysed before each experiment to verify anaerobicity and the absence of redox-active species. These autoclaved, verified bioreactors were then used for growth of *G. Sulfurreducens*, *E. coli* or *S. loihica* cultures.

A typical bioreactor was inoculated with 40% (vol/vol) of stationary phase *G.sulfurreducens* cells. After inoculation, a potential step of 0.24 V versus the standard hydrogen electrode (SHE) was applied and the reactors were incubated until the current stabilized (≈72 h). The potential step was ≈200 mV higher than the midpoint potential, sustaining a half-maximal anodic current. The behaviour of *G. sulfurreducens*, *E. coli* and *S. loihica* biofilms grown on ZnO films grown using PLD was measured.

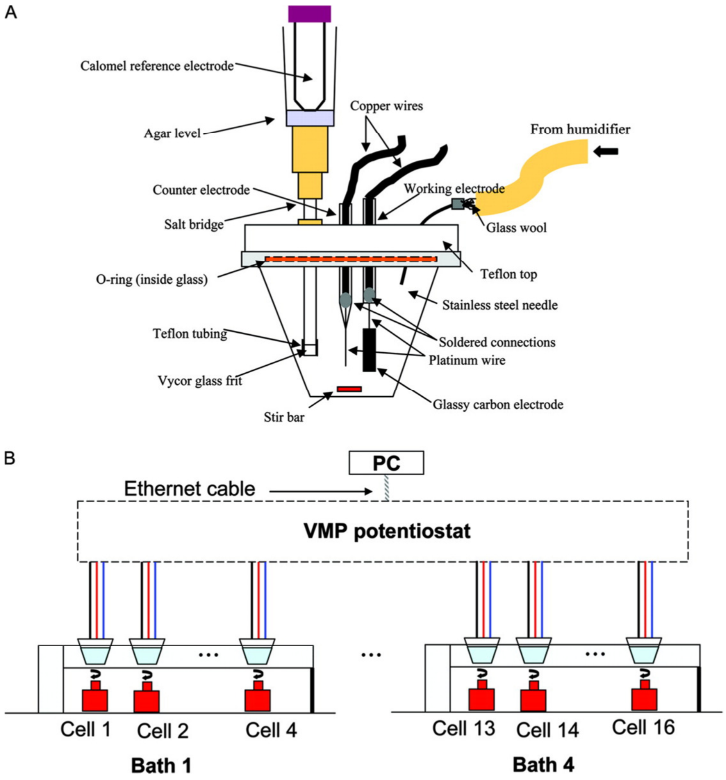

Figure 39: Diagram of three electrode bioelectroreactor and connection to multichannel potentiostat (E. Marsili, J. R. Rollefson, et al. 2008)

Chapter IV: Results and Analyses

This section outlines the results of the various characterisation methods.

IV.1 Plasma Experiments

IV.1.a Electrical Characterisation:

The voltage and current behaviour of the plasma system at electrode separations from 30 mm to 100 mm are displayed on figures 40 and 41 as a function of time, over two periods (41, 42) and half a period (43) of the discharge.

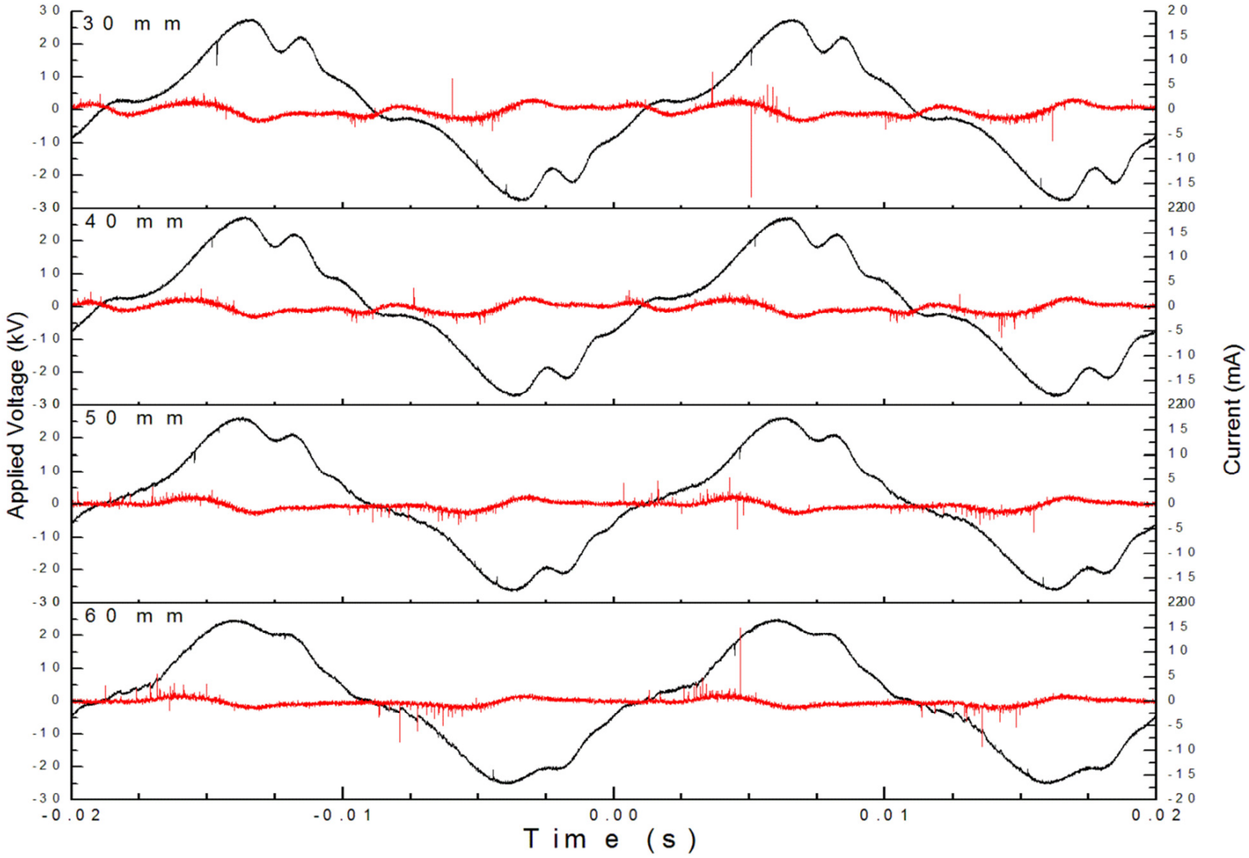

Figure 40: I-V Curves from 30 mm to 60 mm

Voltage traces shows a quasi-sinusoidal signal, however a small “dip” occurs at 6 ms, immediately after the peak voltage is reached. This is most apparent at 30 and 40 mm, but is present at all electrode separations. We believe it is due to the circuitry of our apparatus. The current traces exhibit many short lived microdischarges, characteristic of a silent barrier discharge (SBD) (Kogelschatz, Dielectric Barrier Discharges: Their History, Discharge Physics and Industrial Applications 2003). This indicates electrical breakdown in the gas is in the form of a large number of short-lived current filaments that occur during a well-defined window in the half cycle.

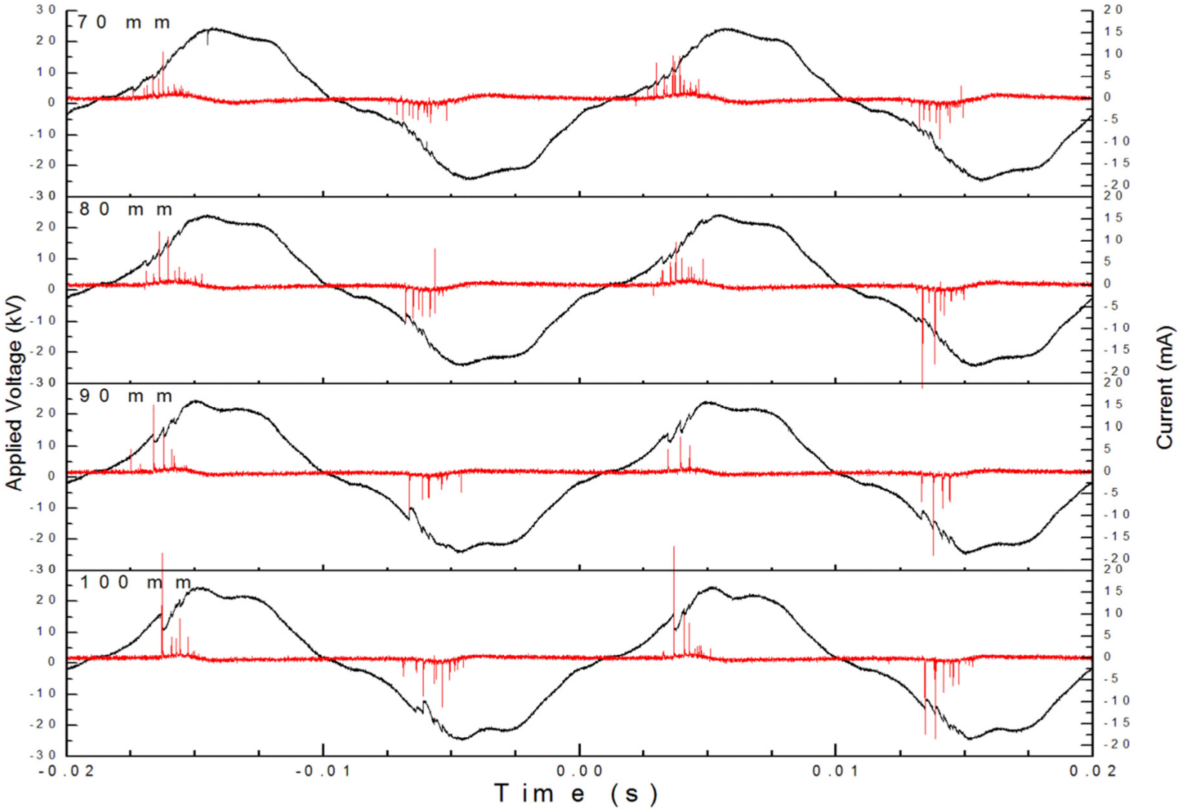

Figure 41: I-V Curves from 70 mm to 100 mm

Similar microdischarge behaviour has been observed and reported in the literature (Zhang, et al. 2010). A maximum peak current of approximately 10 mA is observed. The current filaments appear on top of a continuous capacitive current pattern (Wagner, et al. 2003) (Kogelschatz 2003) that is more apparent at shorter electrode distances but is observed for all the measured electrode separations. We infer from this observation that the discharge regime in this range of electrode gaps remains comparable. The current pattern occurs twice per cycle, and is confined to the rising slope of the applied voltage. The duration of microdischarge activity, measured as the time between microdischarge ignition and cessation (Zhang, et al. 2010, Valdivia-Barrientos, et al. 2006), reduces as electrode separation increases. It can be observed in figures 40 and 41 that the duration of one "bunch" of microdischarges is approximately 6 ms at small separation values (30 - 40 mm), decreasing to approximately 2 ms for the larger separation values (90 - 100 mm), corresponding to duty cycles of over 50% and less than 10%, respectively. This behaviour is compatible with the fact that the value of the breakdown voltage increases with electrode distance (Zhang, et al. 2010, Valdivia-Barrientos, et al. 2006). It is also observed that the number of microdischarges decreases as separation increases, but that the current density of individual discharges increases. At a separation of 30 mm, an average of 20 microdischarges are observed per half cycle, with an average current value of 5 mA, whereas at a separation of 100 mm, these values become 10 microdischarges and 15 mA, respectively. Using values of onset voltage (U_{Min}) and maximum voltage that were measured from Q-V data, a quantitative comparison with expected microdischarge duration, assuming sine wave behaviour of the applied voltage, was calculated. The results are given in table 7. The corresponding values show agreement and show an overall trend for onset voltage to increase with electrode separation.

The Q-V measurements for gap distances from 30 to 100 mm are presented in figures 42 to 44. Figure 43 contains an example of the Q-V plot with the relevant features highlighted. The traces of these figures adhere to the parallelogram shape reported by Kogelschatz (Kogelschatz 2003), therefore confirming that the basic series capacitance model is applicable to our DBD in the experimental conditions used. The discharge characteristics were evaluated from the data of figure 42 and are summarised in table 7 as a function of electrode separation. These parameters are useful when optimising the plasma; considerations such as power dissipated and charge transferred allow the efficiency of the plasma to be quantified.

Table 7: Plasma parameters as a function of electrode separation

Electrode Spacing (mm)	C_{tot} (pF)	C_d (pF)	C_g (pF)	U_{Min} (kV)	U_{Max} (kV)	U_d (kV)	Discharge Duration (ms)	
							Calculated	Measured
30	32	320	36	10.9	28.3	9.8	3.7	6.1
40	32	305	36	12.8	27.1	11.4	3.4	5.6
50	33	293	37	13.6	27.7	12.1	3.3	5.3
60	42	294	49	15.1	26.6	12.9	3.1	4.0
70	42	293	49	14.95	25.9	12.8	3.0	2.3
80	42	247	51	15.4	25.3	12.8	2.9	1.9
90	48	247	60	15.5	24.6	12.5	2.8	2.0
100	45	165	62	14.9	23.9	10.8	2.8	1.9

By overlaying all Q-V plots on a single graph as shown in figure 43, the change in the Q-V plots as separation increases become evident. The parallelogram becomes more pronounced, with sharper corners. At the same time the height reduces quickly and the width of the top and bottom of the shape become longer and more pronounced. The slopes of the sides of the figure become shallower over this interval.

The surface area enclosed by the Q-V Lissajous figure is a measure of the power P (discharge energy multiplied by the frequency) into the discharge, regardless of the shape of this figure (Yehia and Mizuno 2005). Using Origin 6.0, the area of the Q-V plots in figure 42 were measured. Power figures were also calculated from the so-called Manley equations for comparison (Valdivia-Barrientos, et al. 2006, Yehia and Mizuno 2005). The characteristics of the discharge are illustrated below, from an analysis of the measured data in the framework of the series capacitor model that was outlined in section III.1.e (Manley 1943).

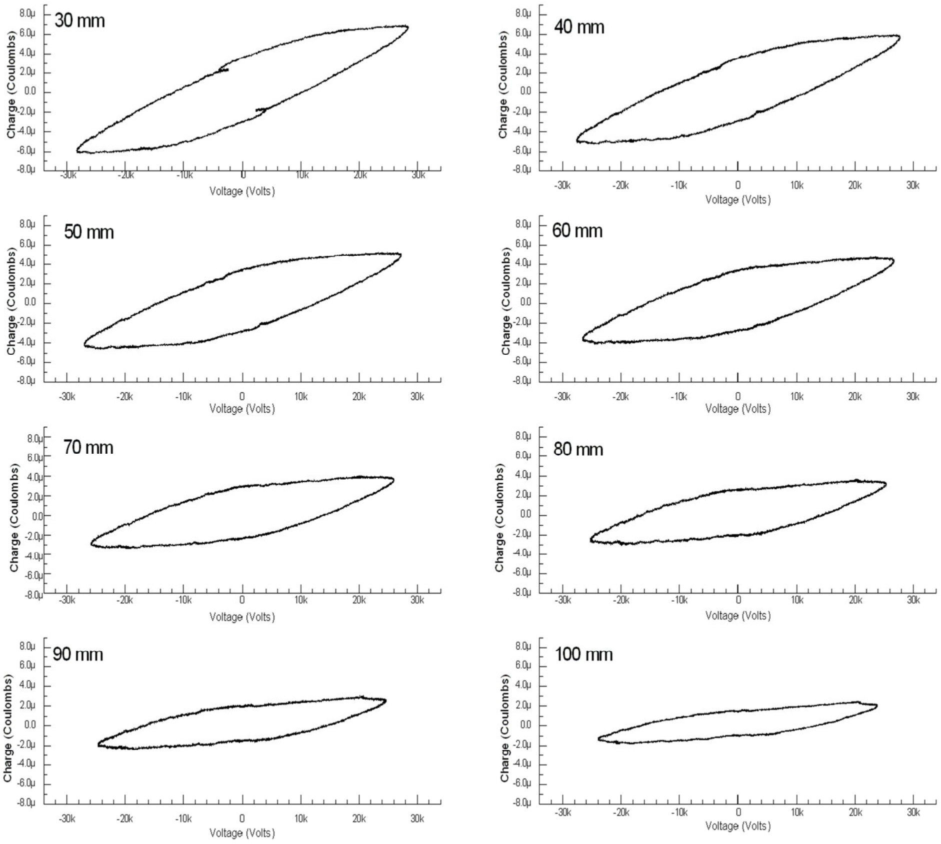

Figure 42: Q-V plots from 30 to 100 mm

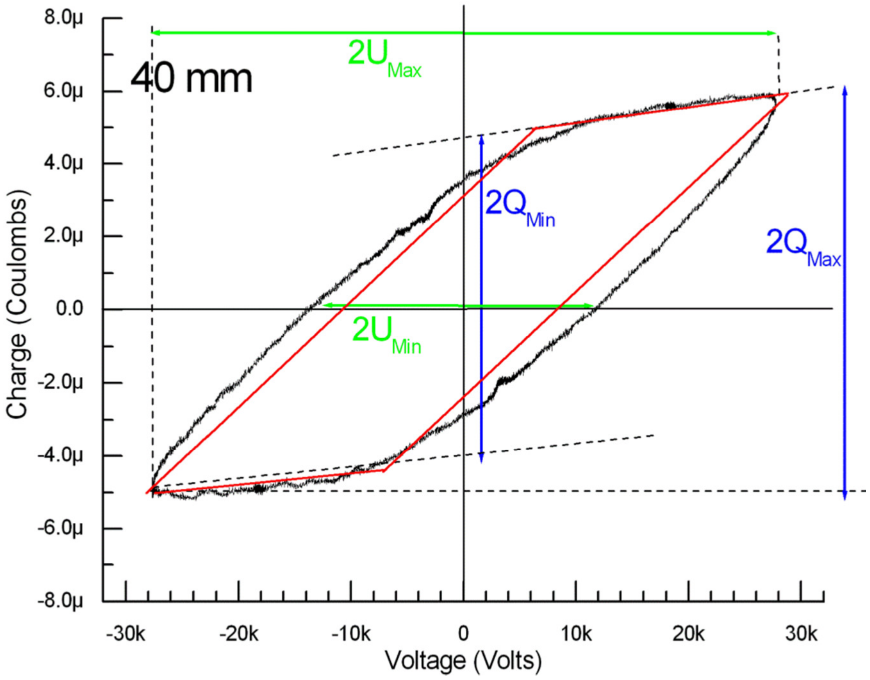

Figure 43: 40 mm Q V Plot with major characteristics highlighted

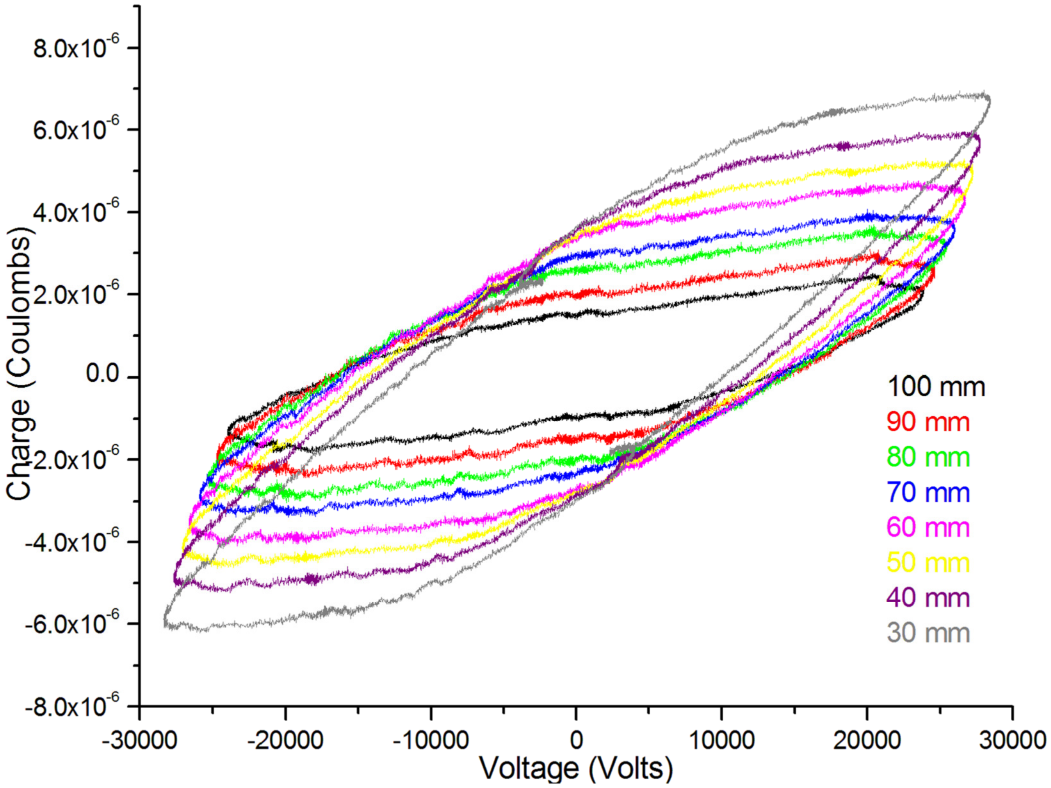

Figure 44: Overlay of Q-V plots from 30 to 100 mm

From figures 42 and 44, it is seen that the slopes yielding the value of the total capacitance (top and bottom slopes) are comparatively shallow and the associated error in the slope measurement is estimated to be ± 10%. A slight departure from the ideal parallelogram shape is observed. Instead of consisting of 4 straight sections with sharp corners, the Q-V plots form a slightly more elliptical shape, consisting of rounded corners and sides that curve outward. This behaviour has been observed by other researchers who typically attribute it to the resistive behaviour of the discharge (Yehia and Mizuno 2005, Falkenstein and Coogan 1997). These deviations will contribute to the error. Keeping these factors in mind, we calculate gas capacitance in the range of 40 pF while the corresponding dielectric capacitances, obtained from the steeper side slopes, are around 300 pF. Gas capacitance values are about one order of magnitude larger than the basic parallel plate capacitor estimates of a few pF obtained with the relative electric permittivity of air/He gas ($\varepsilon_r \sim \varepsilon_0 = 8.85 \times 10^{-12}$ Fm^{-1}) while the latter cannot be readily compared with calculated values because of the composite dielectric electrode used in this work. Using the dielectric and total capacitance values listed in table 7, we deduce a range of β factor values (

$\beta = C_g / C_d$) of $0.11 \leq \beta \leq 0.38$, Typical of the operation of DBD's, β is a key factor controlling the value of the power P (Eliasson, Kogelschatz and Hirth 1987). The experimental values of U_{Min} (the minimum voltage to maintain the discharge) and U_{Max} (the maximum applied voltage) obtained from the Q-V plots are also outlined in Table 7 as a function of electrode separation; furthermore, U_{Min} is plotted as a function of electrode separation in figure 45.

Up to gap values of 70 mm, U_{Min} is observed to increase in a linear fashion, levelling off around 15 kV for larger gap values. A small decrease in the value of the U_{Min} as the gap increases is also observed. This behaviour is attributed to the corresponding change in the overall impedance of the system as described above. The discharge voltage values U_D deduced from U_{Min} are listed in table 7 and exhibit a dependence on gap distance similar to those of U_{Min}.

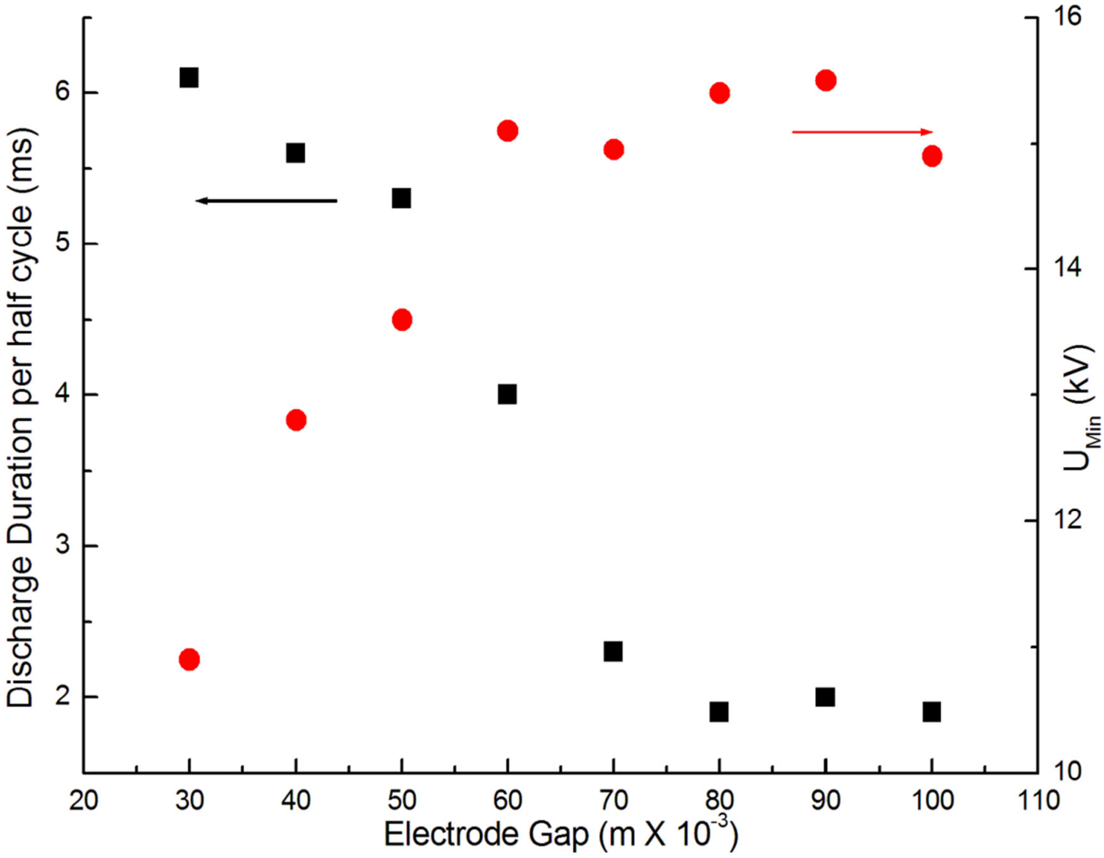

Figure 45: Discharge Duration and Breakdown voltage as a function of Electrode Separation

From the discharge voltage values, the corresponding reduced breakdown field strength E/n values are estimated (in units of Td = 10^{-17} Vcm^{-2}), assuming the atmospheric pressure gas mixture to be at 300 K and show the corresponding plot on figure 46. The observed behaviour of U_{Min} and E/n are compatible with the expected behaviour of the Paschen curve for large values of the Pd product (Burm 2007). In particular, we note from figure 45 that the control of the gap spacing strongly influences the electric field at breakdown, thereby providing a control over the electron energy during microdischarge activity and thereby the yield of the physical/chemical processes driven by electron collisions.

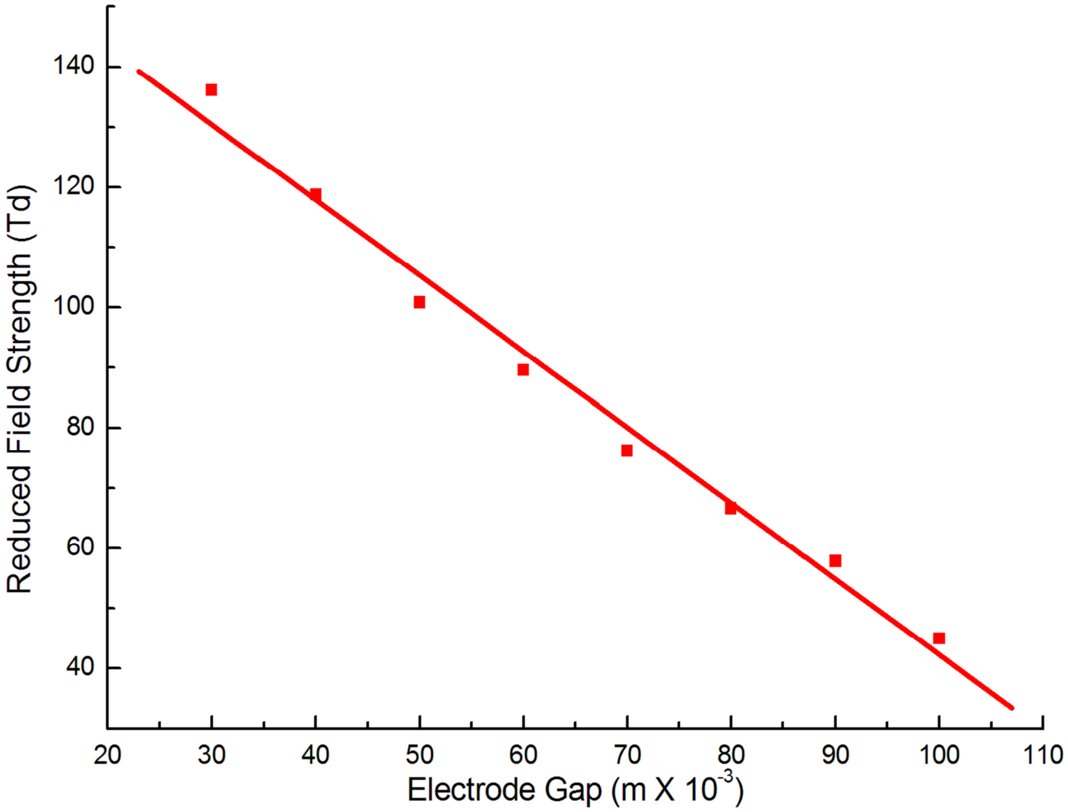

Figure 46: Reduced Field Strength as a function of electrode separation

Figure 47 illustrates the variations of the discharge power P as a function of gap distance on and the displaced charge per cycle. P is estimated either directly from the surface area of the enclosed Q-V plots (calculated using “Origin 6.0”) or by using the following expression (a variation on the Manley equation). This formula has no dependence on the applied voltage shape; it is based only on measurable quantities

$$P = 4fC_d(1+\beta)^{-1}U_{Min}(U_{Max} - U_{Min})$$

The two curves are in good agreement with similar shaped curves and magnitudes that are within 10%. This is further evidence that the capacitor in series model described previously is valid for interpreting the microdischarge beahvour of the system.

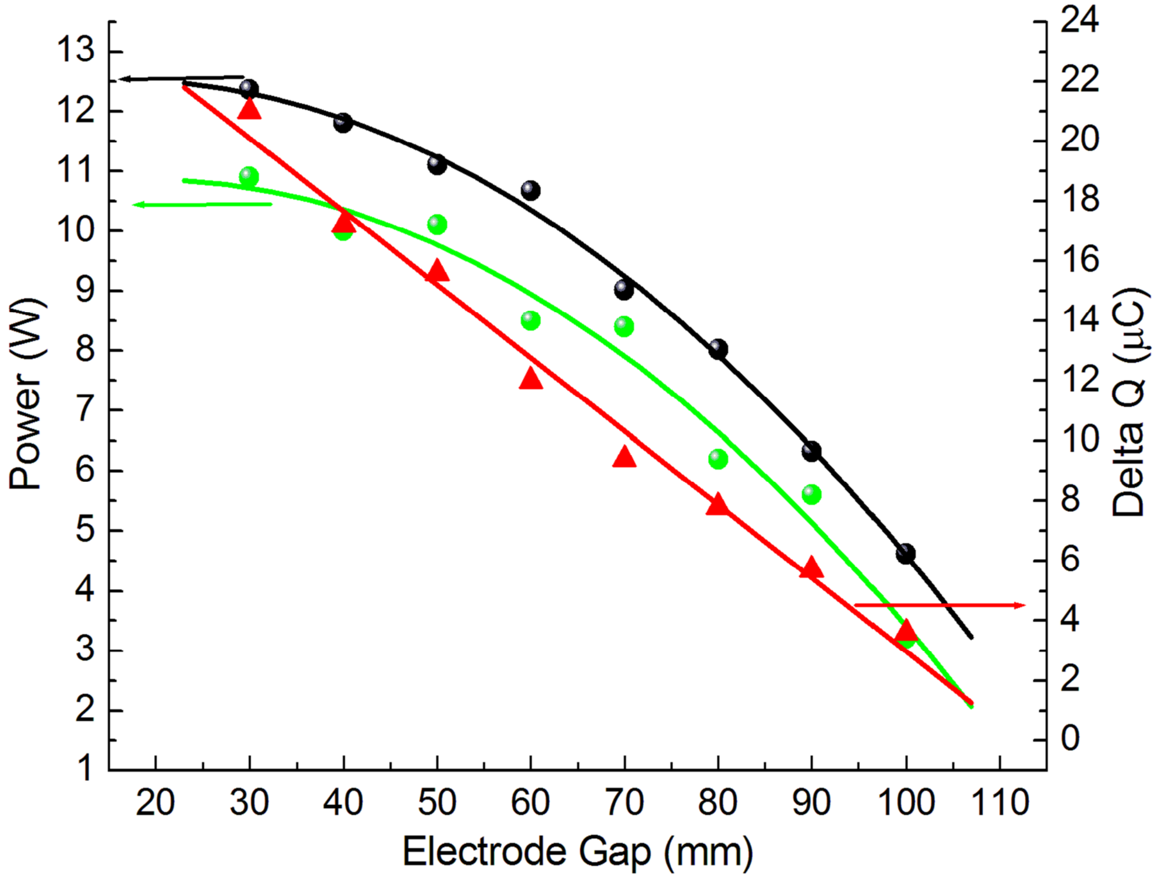

Figure 47: Measured Power (black line with circles) calculated power (green line with squares) and charge transferred (red line with triangles) as a function of electrode separation

The measured discharge power is in the range of several watts and exhibits a quadratic dependence on gap distance, similar to the known quadratic dependence of the power on U_{min} (Eliasson, Kogelschatz and Hirth 1987). In contrast, the displaced charge per cycle shows a linear decrease with gap distance. These are useful relations for the purpose of optimising or controlling the discharge power.

IV.1.b Emission Spectroscopy:

Figure 48 is a photograph of the plasma system in operation at an electrode separation of 40 mm. As can be seen therein, the plasma glow is clearly confined to the inter-electrode volume. A number of filaments are also faintly visible.

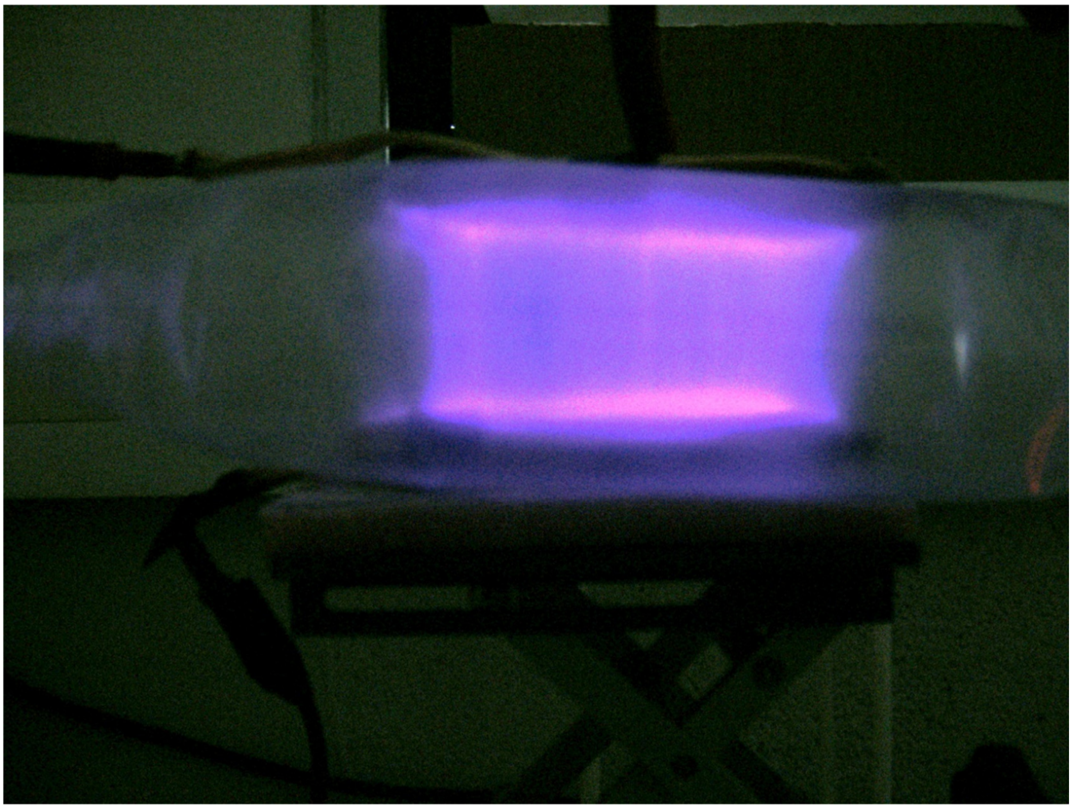

Figure 48: Image of 15 kV plasma system in operation (electrode separation 40 mm)

An emission spectrum is displayed in figure 51. This spectrum is taken at the centre of a gap of 40 mm and is displayed on a relative intensity scale. This spectrum was recorded by integrating over 5 seconds and averaging over 5 samples, allowing genuine spectral features of the source to be distinguished from background noise. Considering that the leak rate we have measured is on the order of 3 mg min^{-1}, we are confident that the change in the composition of the gas in our plasma is negligible over the time scale in which we take our measurements and does not affect the emission spectrum intensity. The absorption of light in the ultraviolet rage by the polyethylene material of the bag was measured; the bag was found to transmit 92% of the light. In the insert of figure 49, the same spectrum is displayed on an absolute intensity scale. This was used for the purpose of allowing comparison with the software package SPECAIR (C. Laux 2002, Laux, Spence, et al. 2003).

The spectrum that we present shows similarity to those reported by several authors studying helium/air plasmas at atmospheric pressure (Ries, et al. 2011, Chiper, et al. 2004, Walsh, et al. 2010). The lines observed in our spectra could be readily identified using tables of spectral data and are presented in table 8 (Pearse and Gaydon 1976).

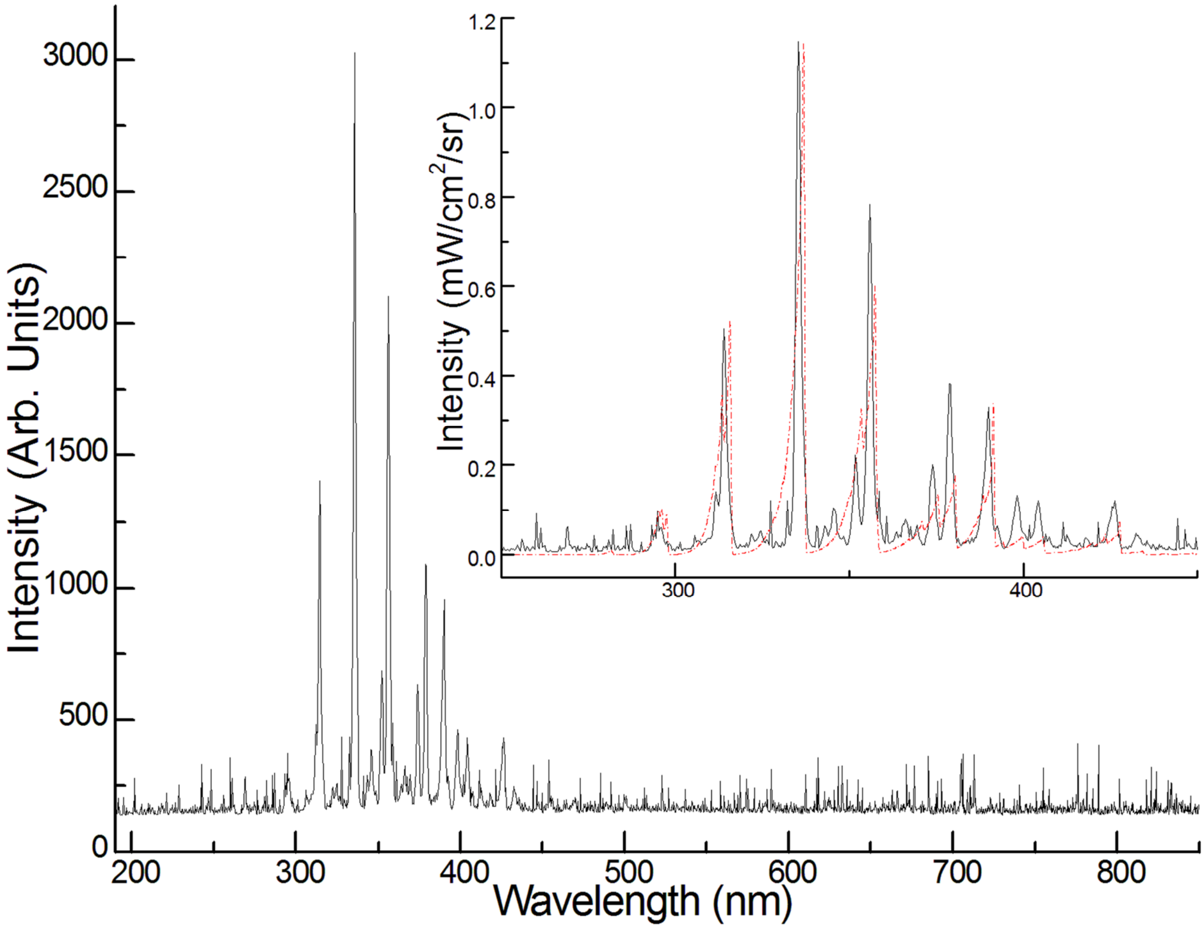

Figure 49: Optical emission spectrum of plasma at an electrode separation of 40 mm (insert) the same spectrum on an intensity calibrated scale

The emission peaks of most interest are found in the near UV and blue part of the visible spectrum, and correspond to the vibrational structure of electronic transitions in common diatomic molecules. The rotational structure is not fully resolved in our experimental conditions. The strongest emissions occur from 300 nm to 425 nm. These bands are attributed to the second positive system of N_2, the first negative system of N_2^+ and the 306.4 nm system of OH. Bands located from 315 nm to 357 nm are attributable to the second positive system of N_2. Emissions from 370 nm to 425 nm are chiefly due to the first negative system of N_2^+ and occur due to the Penning ionisation mechanism, according to Walsh *et al* (2010).

Table 8: Emission spectra data **(Pearse and Gaydon 1976)**

	Observed Wavelength (nm)	**Attributed Wavelength (nm)**	**Electronic Transition**	**Vibrational Levels**		**Species**
				v’	***v’’***	
	243.26	243.30	$B^2\Pi - X^2\Pi$	3	4	NO
	248.81	248.78	$B^2\Pi - X^2\Pi$	2	4	NO
	261.26	261.34	$A^2\Sigma^+$-$X^2\Pi$	2	0	OH
	269.89	269.11	$A^2\Sigma^+$-$X^2\Pi$	3	1	OH
	282.00	281.91	$A^2\Sigma^+$-$X^2\Pi$	1	0	OH
	287.44	287.53	$A^2\Sigma^+$-$X^2\Pi$	2	1	OH
	288.60	288.23	$A^2\Sigma^+$-$X^2\Pi$	2	1	OH
	295.18	295.12	$A^2\Sigma^+$-$X^2\Pi$	3	2	OH
	296.34	296.24	$A^2\Sigma^+$-$X^2\Pi$	3	2	OH
	301.74	302.12	$A^2\Sigma^+$-$X^2\Pi$	0	0	OH
	307.12	306.72	$A^2\Sigma^+$-$X^2\Pi$	0	0	OH
A	315.38	315.93	$C^3\Pi_u$-$B^3{}_g$	1	0	N_2
1	336.29	337.13	$C^3\Pi_u$-$B^3{}_g$	0	0	N_2
B	351.86	353.67	$C^3\Pi_u$-$B^3{}_g$	1	2	N_2
2	356.96	357.69	$C^3\Pi_u$-$B^3{}_g$	0	1	N_2
C	373.90	375.54	$C^3\Pi_u$-$B^3{}_g$	1	3	N_2
3	379.60	380.49	$C^3\Pi_u$-$B^3{}_g$	0	2	N_2
	390.62	391.44	$B^2\Sigma_u{}^+ - X^2\Sigma_g{}^+$	0	0	N_2^+
D	398.3	399.84	$C^3\Pi_u$-$B^3{}_g$	1	4	N_2
4	404.1	405.94	$C^3\Pi_u$-$B^3{}_g$	0	3	N_2
	426.48	427.81	$B^2\Sigma_u{}^+ - X^2\Sigma_g{}^+$	0	1	N_2^+
	500.96		$2s^22p3d$ - $2s^22p3p$	Atomic		N^+
			$1s3p - 1s2s$	Transition		He
	586.91		$1s3d - 1s2p$			He
	667.09		$1s3d - 1s2p$			He
	685.78	685.63	$b^4\Sigma_g{}^-$ -$a^4\Pi_u$	0	2	O_2^+
	706.20		$1s3s - 1s2p$	Atomic		He
	776.06		$2s^22p^33p\ {}^5P$ - $2s^22p^33s\ {}^5S$	Transition		O

The small band at 685.78 nm is assigned to a transition in the first negative system of the O_2^+ molecular ion following Pearse and Gaydon (1976); we note the absence of any other vibrational components of this transition in our spectra. A similar observation was made by Lee *et al* in the case of a He/O_2 atmospheric plasma glow discharge (APGD) (2001). We observe a small number of bands of weak intensity below 260 nm, which are attributable to transitions in NO (Pearse and Gaydon 1976). Other vibrational components of the same system are likely to overlap with OH emission bands in the range from 260 nm to 310 nm. Emission from atomic species are also observed in the visible range (see figure 48), with the most intense being the helium line at 706.20 nm and the oxygen line at 776 nm. The emission at 500.96 nm is possibly a blend of N^+ and helium contributions. Our spectrum shows similarity to spectra obtained with similar non thermal plasma apparatus used by other groups for decontamination (Ragni, et al. 2010, Perni, et al. 2007, Schwabedissen, et al. 2007), in particular, we note the presence of the neutral atomic oxygen line around 777 nm, used by Perni *et al* as an indicator of the significant role played by O* species in the inactivation of *E. coli* (Perni, et al. 2007).

IV.1.c Temperature Estimates using SPECAIR:

Spectra were obtained in similar acquisition conditions as a function of gap distance on an absolute intensity scale. An example of these is shown as an insert in figure 49. These spectra were analysed using the SPECAIR simulation program designed by Laux *et al* (C. Laux 2002, Laux, Spence, et al. 2003), which has been used extensively to model the optical emission spectra of various types of plasmas at atmospheric pressure (Luo, Denning and Scharer 2008). SPECAIR can calculate the emission spectrum using 37 molecular transitions in NO, N_2, N_2^+, O_2, CN, OH, NH, C_2 and CO and atomic lines for N, O and C. SPECAIR intensity spectra are generated by solving the equation of radiative transfer. It uses the values of emission and absorption coefficients which are based on the level populations obtained from either collisional radiative calculations or by assuming the internal levels follow Maxwell Boltzmann distributions under non-equilibrium conditions (C. Laux 2002) at T_e, T_v and T_r the electronic, vibrational and rotational temperatures, respectively.

Using SPECAIR, we obtained a visual best fit with our emission spectra using T_e, T_v, T_r and T_t as fitting parameters. Typically $T_e > T_v > T_r > T_t$ *and* T_t will also be near room temperature

(Laux, Spence, et al. 2003). The molar fraction of N_2^+/N_2 is also a fitting parameter. We found that the value of T_e was the most critical parameter governing the absolute spectral intensity of all bands, while the vibrational temperature governs the relative intensities of the N_2 bands. We typically adjusted T_e on the value of the intensity of the 335 nm emission band, and adjusted T_v to get the best fit with the relative intensities that we observed. We note here that the band at 356.96 nm is consistently underestimated in the SPECAIR spectra. The rotational temperature T_r is based on a fit of the envelope of the rotational structure in our spectral resolution conditions, and thus is a less reliable physical parameter as it is unresolved.

An example of a best fit is presented as an insert in figure 49. This was achieved with values of $T_e = (4{,}980 \pm 100)$ K, $T_v = (2{,}700 \pm 50)$ K, $T_r = (3{,}100 \pm 50)$ K, $T_t = (300 \pm 50)$ K and $N_2^+/N_2 = 2.8\times10^{-8}$. From these figures, we estimate the ion density to be $n_i \approx 1.1\times10^{17}$ m^{-3} assuming the ion temperature to be equal to the translational temperature. This is also an estimation of the electron density n_e. Gulec *et* al (2011), using SPECAIR, report results of $T_e = 5{,}850 \pm 400$ K, $T_t = 300 \pm 50$ K and $T_v = 2500 \pm 500$ K. Lu *et al* report $T_r = 1{,}800$ K and $T_v = 2{,}600$ K and $n_e = 7\times10^{18}$ m^{-3} using electrical conductivity measurements. (2003) Nersisyan and Graham return values of $T_t = 360 \pm 20$ K and $T_v = 2{,}700 \pm 900$ K (2004). Chiper *et al* reports a $T_r = 450$ K (2004). This comparison shows our results, obtained at electrode separations and voltages that are an order of magnitude larger; to be in line with these atmospheric plasma DBD works.

As electrode separation is increased, a reduction in overall emission intensities is observed. However, the relative intensities of peaks are conserved. Direct comparison of intensities at different electrode separations is difficult, due to experimental constraints. Similar temperature fits were applied to the spectra as a function of electrode separation (not shown). Figure 50 illustrates the variations of the SPECAIR best fit values of T_e, T_v and n_e as a function of electrode separation. It is seen that T_v remains constant at 2,700 K for all the spectra, while a small but noticeable decrease in T_e is seen, while n_e fluctuates slightly but remains in the order of 10^{17} m^{-3}. As the reduced electric field value determines the electron temperature, the observed decrease in T_e is compatible with the data of figure 46 showing a decrease of E/n with gap distance.

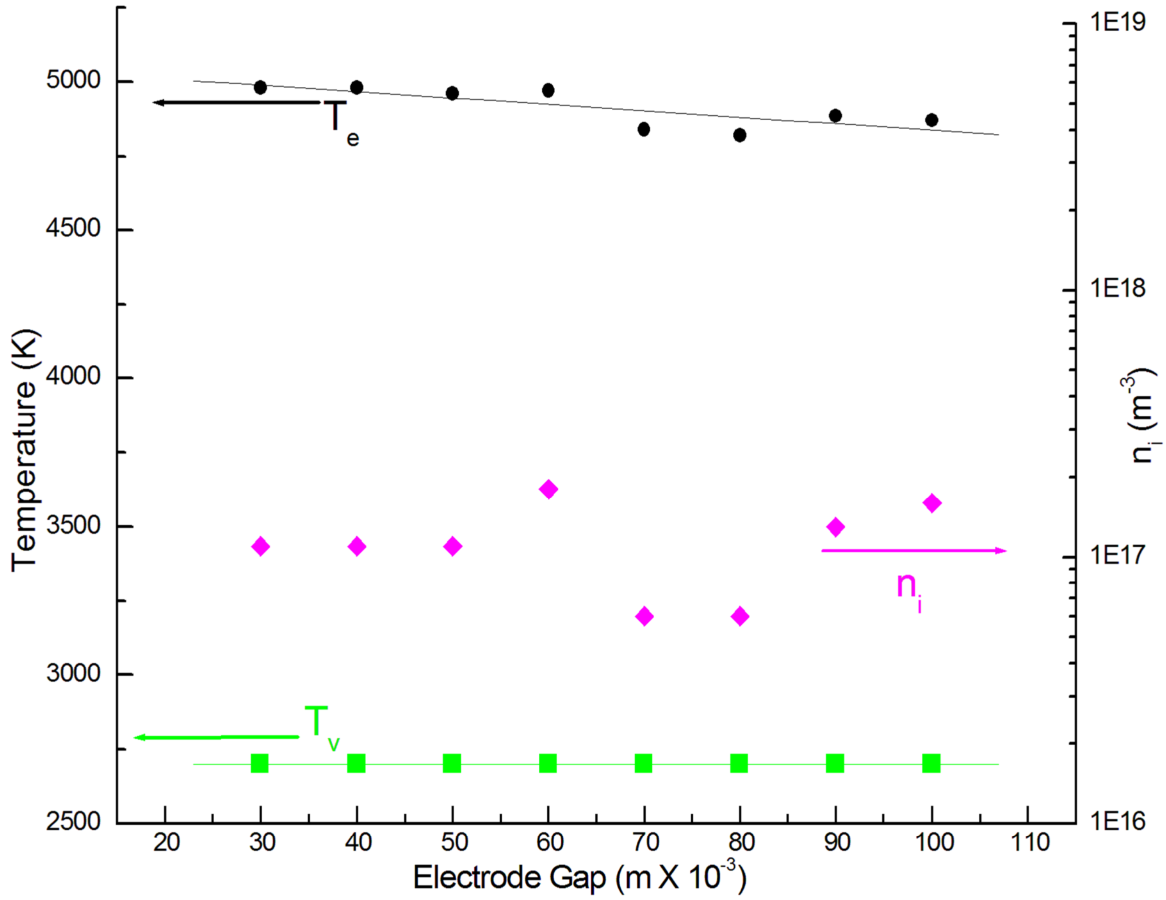

Figure 50: Graph of electronic (black circles) and vibrational (green squares) temperatures and ion density (purple lozenges) as a function of electrode gap

T_v was also estimated using the Boltzmann plot method. The relative intensities of emissions from the second positive system of N_2 were measured at all electrode separations. The Einstein emission coefficients were taken from Laux and Kruger (1992). An example of the data used to generate a Boltzmann plot for 40 mm separation is given in table 9. Using this data, a graph of $ln\ [\lambda/A]$ against energy in eV was plotted. The slope of this graph is equal to T_v in eV. This was then converted to Kelvin. The Boltzmann plot for 40 mm is displayed in figure 51. The T_v calculated using this method is (3200 ± 300) K, which is in good agreement with the SPECAIR estimate.

Table 9: Boltzmann plot data for 40 mm

λ (nm)	(v', v'')	Intensity	A (x 10^7 s^{-1})
337.1	1 (0, 0)	2879	1.337
357.7	2 (0, 1)	1957	0.890
380.5	3 (0, 2)	940	0.353
405.9	4 (0, 3)	267	0.109
315.9	a (1, 0)	1257	1.266
333.9	(1, 1)	310	0.0579
353.7	b (1, 2)	545	0.559
375.5	c (1, 3)	457	0.4885
399.8	d (1, 4)	310	0.2375

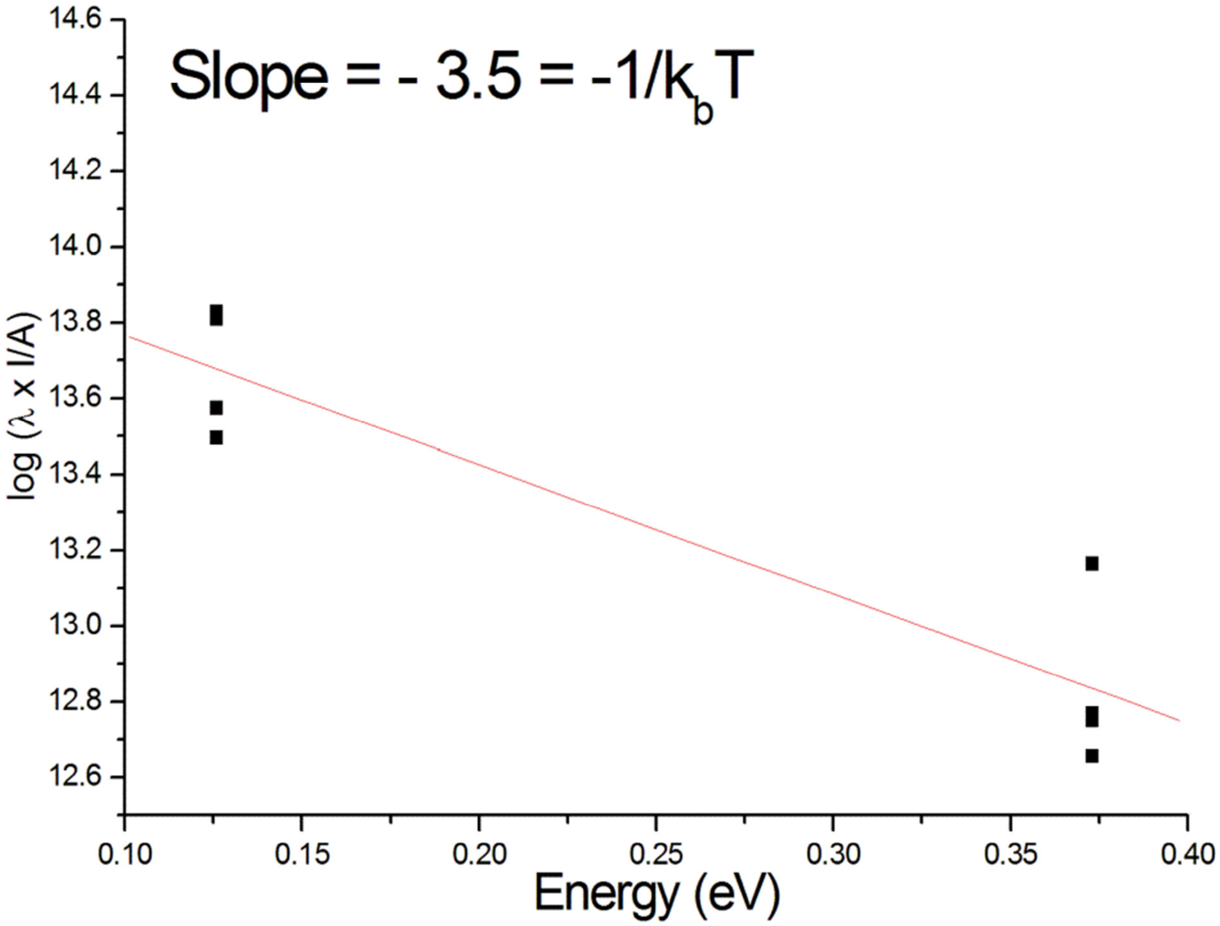

Figure 51: Boltzmann plot at 40 mm

IV.1.d Effects of Plasma on Package:

The results of water contact angle measurements on a piece of plastic from a plastic bag that was not exposed to the plasma, compared to a similar piece from a bag that was used repeatedly in plasma experiments is shown in figure 52. Contact angle measurements were performed immediately after plasma treatment (< 1 hour). Twelve measurements were taken at various points in the surface of each piece, with a distance of no less than 5 mm between adjacent drops. The pre-treatment water contact angle has a mean value of 96.33 ^{O} with a standard deviation of ±5 ^{O}. Since a value of 90 ^{O} is where a surface is considered "hydrophobic", the surface of the bag is in the hydrophobic range. In contrast, the mean water contact angle, post treatment, is 54.6 ^{O} with a standard deviation of ± 5.8 ^{O}. This is significantly reduced, a change of 41.7 ^{O} ± 10 ^{O}.

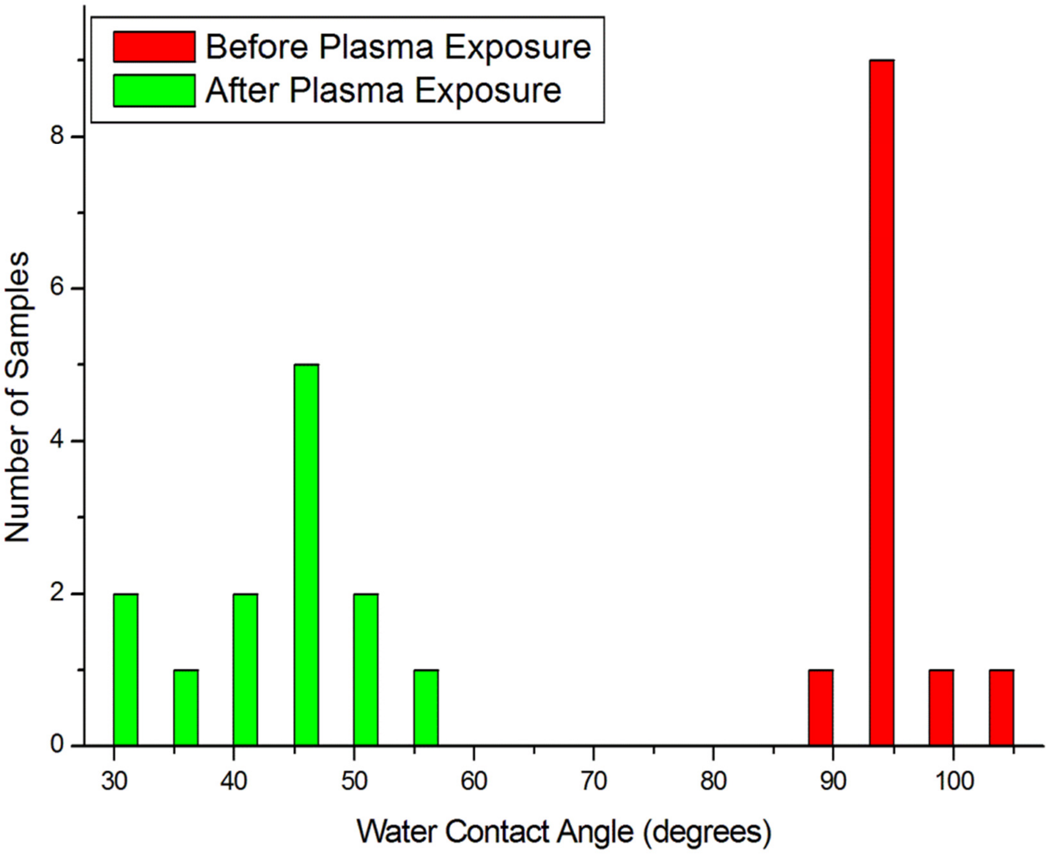

Figure 52: Graph of change in Water Contact Angle

This reduction is in agreement with results reported by other authors. Chiper *et al* (2009) report reductions from 98° to 68° (30°) after treatment with a parallel plate helium DBD. Ren *et al* showed the change in water contact angle for a PE film exposed to a DBD in air with respect to time and report that water contact angle was reduced from 93.2° to 54° over a 50 second treatment time (Ren, et al. 2008). They also show that the greatest change in water contact angle happens in the first few seconds (0 – 10 s) of plasma exposure, with further exposure only having a limited effect on the plastic. Beyond 20 seconds, the change is negligible. A similar observation is made by Geter, Morent and Lays (2007) who observe a reduction from 101.7° to 53.5° after 10 seconds of plasma exposure. The majority of the reduction is observed to occur in the first 2 seconds of plasma treatment. Šíra *et al* report reductions from 91° to values that are approximately 40° when PE is exposed to plasmas formed from several combinations of nitrogen and hydrogen. The reductions reported by these authors show are similar to the measurements we report. The mean value of the contact angle before plasma treatment is 96° ± 4.2° and the mean value after treatment is 54° ± 10°, values that are 99.6% and 99% of our results, respectively. This decrease is attributed to an increase in polarised molecules in the surface of the plastic, due to the interaction of the plasma with the polymers of the plastic. Using attenuated total reflectance (ATR) spectroscopy, de Geyter *et al* conclude that plasma, formed from air, generates "oxygen containing functionalities (alcohols, aldehydes, ketones and carboxylic acids) on the PE surface" (2007). Wang *et al* concluded similarly, that "the PE surface is activated and combined with oxygen when exposed to the air DBD" (2008).

IV.1.e Microbial Inactivation:

Microbial inactivation experiments were performed by our colleagues in the DIT school of Food Science and Environmental Health at an electrode separation of 40 mm for a period of 5 minutes. The microbial samples were placed in the sealed bag, outside of the direct plasma stream. The population levels of the bacterial samples are displayed in figure 53. The population of *E. coli* was significantly reduced by more than 1.5 log cycles after the applied plasma treatment. The parent strain and the Δ*dnaK*, Δ*soxR*, Δ*soxS*, Δ*oxyR*, Δ*rpoS* mutants exhibited similar susceptibility during the 5-minute treatment. Nevertheless, the parent strain appeared to recover faster than some of the mutants, as can be seen from the examples in figure 54. We believe that this points to a role for the transcriptional regulators *oxyR* and *rpoS* on the *E. coli* repair mechanisms in the plasma stress environment. It is evident from these storage studies that the generated environment of the applied treatment targets specific mechanisms activating these regulator systems. The efficacy of the treatment can also be assessed by comparison of the microbial recovery between the untreated (control) and the plasma treated samples (figure 54). Most of the mutant cells exhibited slower or no growth when compared with their controls, examples are given in figure 54 (b), (c).

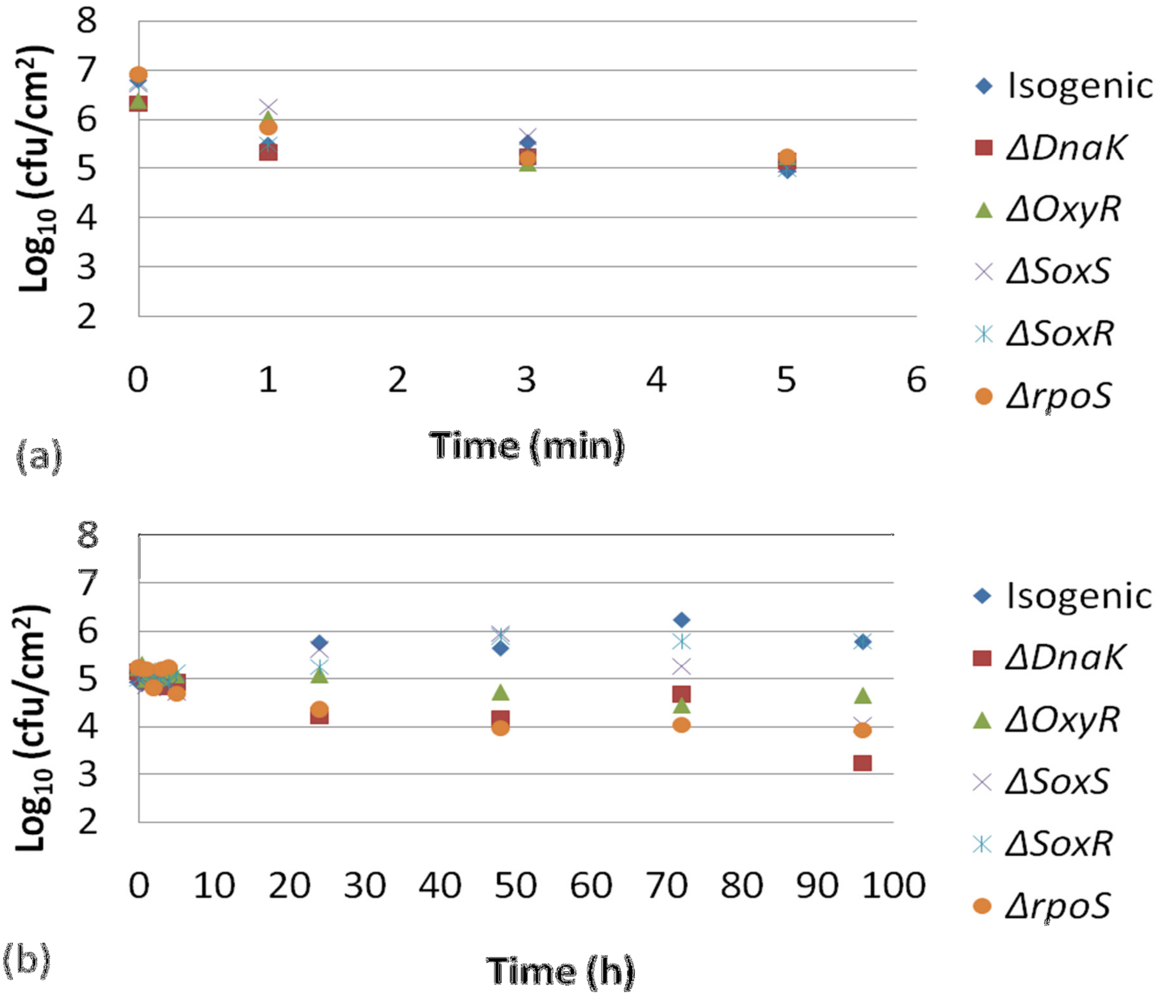

Figure 53: (a) Microbial inactivation of E. coli K12 during the plasma treatment
(b) Microbial recovery of E. Coli following plasma treatment
(◊: wild type, ▫: ΔDnaK, ▲: ΔOxyR, x: ΔSoxS, *: ΔSoxR, ○: ΔrpoS.)

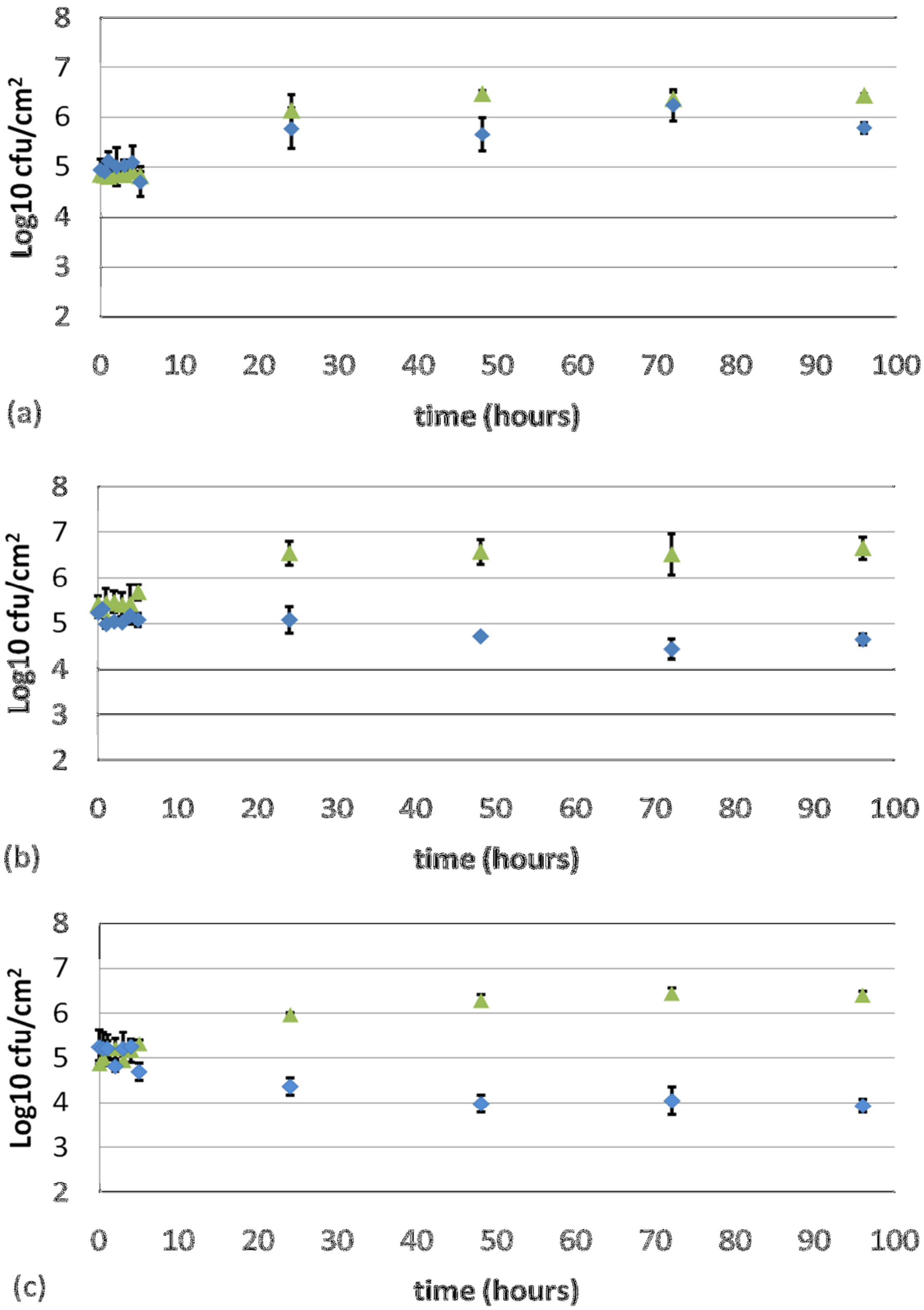

Figure 54: Microbial recovery of (a) isogenic E. coli K12, (b) ΔoxyR, (c) ΔrpoS (▲: controls – non-plasma treated, ◊: plasma treated samples)

Figure 54 (a) shos E. *coli* K 12 recovers most quickly and stabilises at a population of approximately 6 log CFU/ cm^2, about 1 log higher than immediately after plasma treatment. *oxyR* does not show population recovery, but reduces still further to log 4.5 CFU/cm^2. *OxyR* is a redox responsive transcription regulator that is induced in the presence of oxygen radicals (Greenberg, et al. 1990). Strains with *oxyR* deletions are also unable to induce hydrogen peroxide (H_2O_2) inducible genes so they are hypersensitive to it (Christman, Storz and Ames 1989). From these results the main mechanisms of antibacterial action appear to be related to an oxidative environment. This conclusion is supported by the results of Perni *et al* (2007), who report an 8 log cycle reduction for the *ΔsoxS* mutant, achieved even more quickly when oxygen is introduced into their He APGD plasma pencil system. We attribute the differing log reductions to differences in experimental configuration. Additionally, the effect on the microbial recovery post-treatment, usually overlooked in published scientific works, appears to be an important issue for unravelling the antimicrobial mechanisms of specific disinfection technologies.

Other mutants that did not result in full population recovery during the storage time were the Δ*dnaK* and Δ*rpoS* mutants. *Rpos* strains exhibited a continuing drop in population over the following 100 hours DnaK and RpoS are two proteins protecting from general stress which, although not dedicated mechanisms of protection against oxidative radicals, have been previously shown to confer protection against them (Loewen, et al. 1998). Recovery of Δ*SoxR* was highest among the examined mutants and close to the recovery of the control samples (results not shown). The SoxR is the regulator which, in its oxidised form, enhances transcription of *soxS* that encodes for a transcriptional activator of several genes of the SoxRS regulon (Pomposiello and Demple 2001). These genes are directly responsible for the removal of superoxide anions or repair of superoxide damaged macromolecules such as DNA. The high recovery of Δ*soxR* indicates that superoxide anions (O_2^-) do not appear to be the agents that constrain the recovery of the plasma treated cells.

Production of reactive oxygen /nitrogen species and other radicals have a major role on the antimicrobial mechanism. Moisan et al have described two general mechanisms in which cold atmospheric plasma inactivates microbes (2001). These include cell damage by ultraviolet light or etching under the action of atomic and molecular radicals produced by the plasma. Other mechanisms of microbial inactivation (Laroussi, Mendis and Rosenberg 2003) due to plasma treatment are cellular damage caused by the plasma generated electrostatic stress (Mendis, Rosenberg and Azam 2000) and cell wall damage caused by ion perforation and ozonation (Poiata, et al. 2010). The SEM images show that the application of plasma resulted in cell disruption for the examined parent, Δ*soxR* and Δ*rpoS* cells (see Figures 55-57). Considering that the samples were not placed within the plasma stream, the etching effect could be considered the preponderant mechanism of bacterial inactivation in our work.

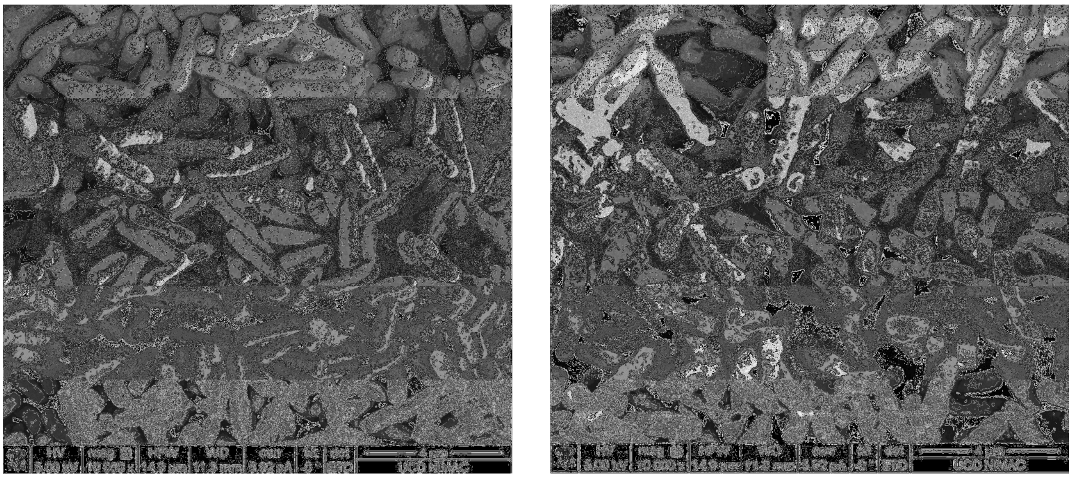

Figure 55: SEM Images of isogenic E.coli K12 (control: left, plasma treated for 5 minutes: right)

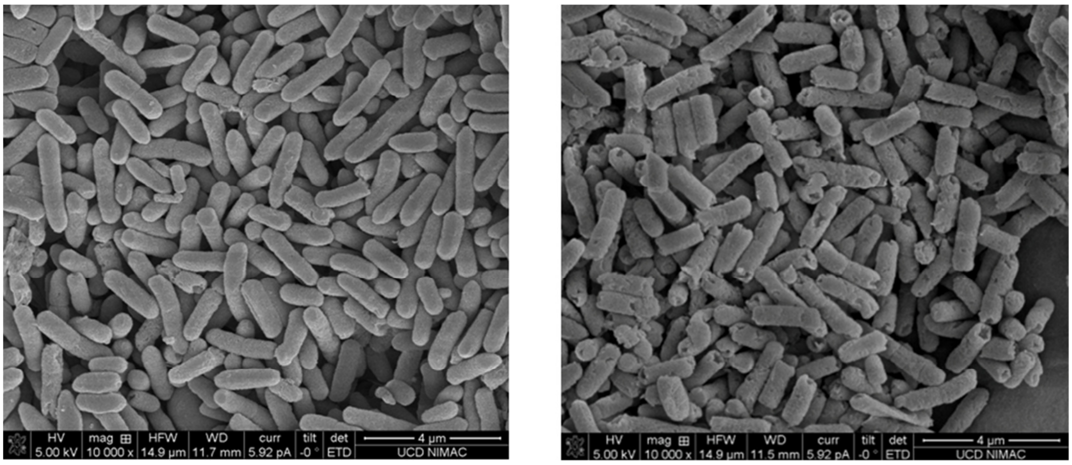

Figure 56: SEM images of E. coli ΔrpoS (control: left, plasma treated for 5 min: right)

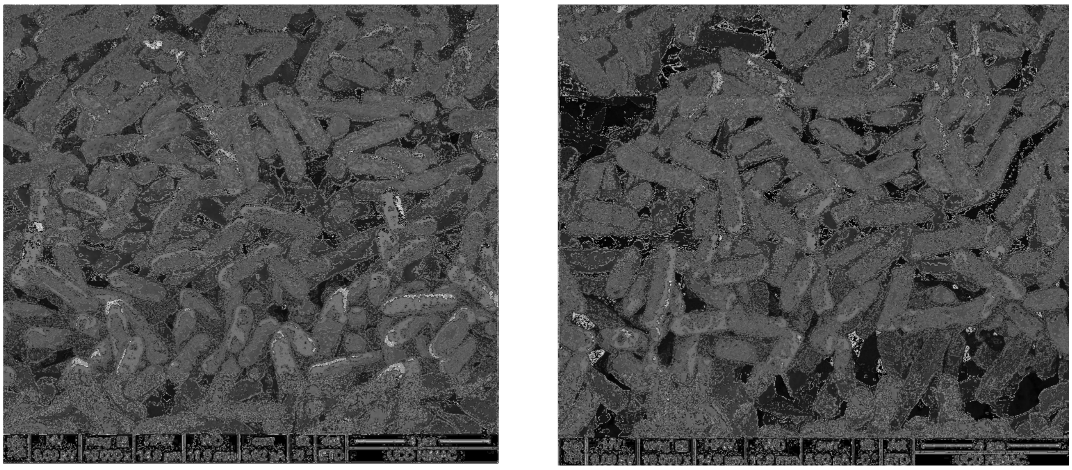

Figure 57: SEM images of E. coli ΔsoxR (control: left, plasma treated for 5 min: right)

IV.2 Pulsed Laser Deposition of ZnO Thin Films:

Zinc oxide thin films, nominally undoped, doped with 2% aluminium and alloyed with magnesium were prepared by pulsed laser deposition. These films were characterised using several analytical methods to quantify structural and electrical properties.

IV.2.a Film thickness:

Films were masked during deposition, leaving a clean surface with a sharp edge. Contact profilometry was performed along this boundary to estimate film thickness. Figure 58 shows the cross section of two ZnO: Al films that were measured.

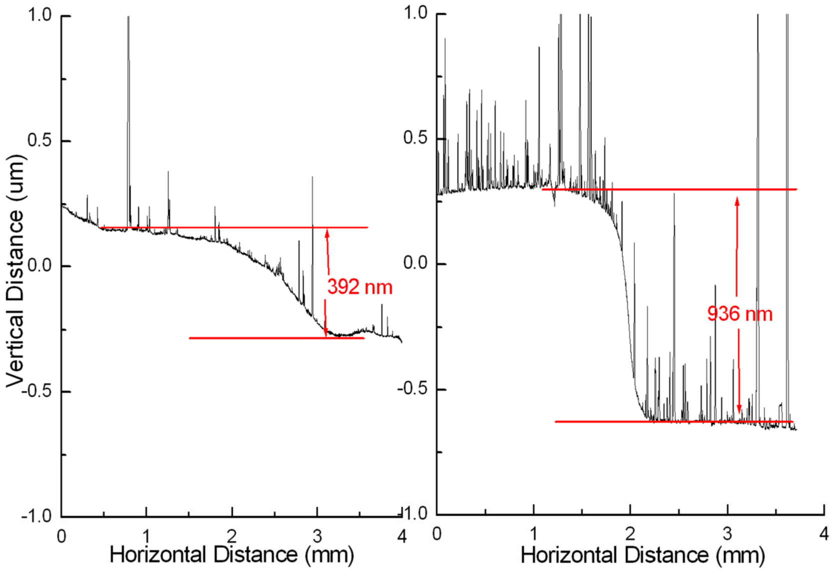

Figure 58: Graph of Height profile of 20,000 (left) and 40,000 (right) ZnO: Al samples

Using profilometer measurements, a relationship between the number of shots used to grow a sample and sample thickness became apparent. It was found that samples grown using 10,000 laser pulses grew to a thickness of 200 – 250 nm, samples grown with 20,000 laser pulses grew to a thickness of 350 – 450 nm and samples grown with 40,000 laser pulses grew to approximately 1 µm, leading to an calculated average layer thickness of 23 picometres per shot. Knowledge of film thickness is necessary to make estimates of resistivity from measurements of sheet resistance. Due to the individual nature of PLD systems, direct comparison of thickness per shot is difficult, but several authors report film thicknesses for ZnO and doped ZnO films of approximately 200 to 350 nm (Narasimhan, et al. 1997, Park, Ikegami and Ebihara 2005), measured either through a profilometry method as described herein, SEM or through spectroscopic ellipsometry.

IV.2.b X-ray Diffraction:

Figure 59 shows a diagram of X-ray Diffraction (XRD) patterns of ZnO films as a function of film thickness proportional to shot count.

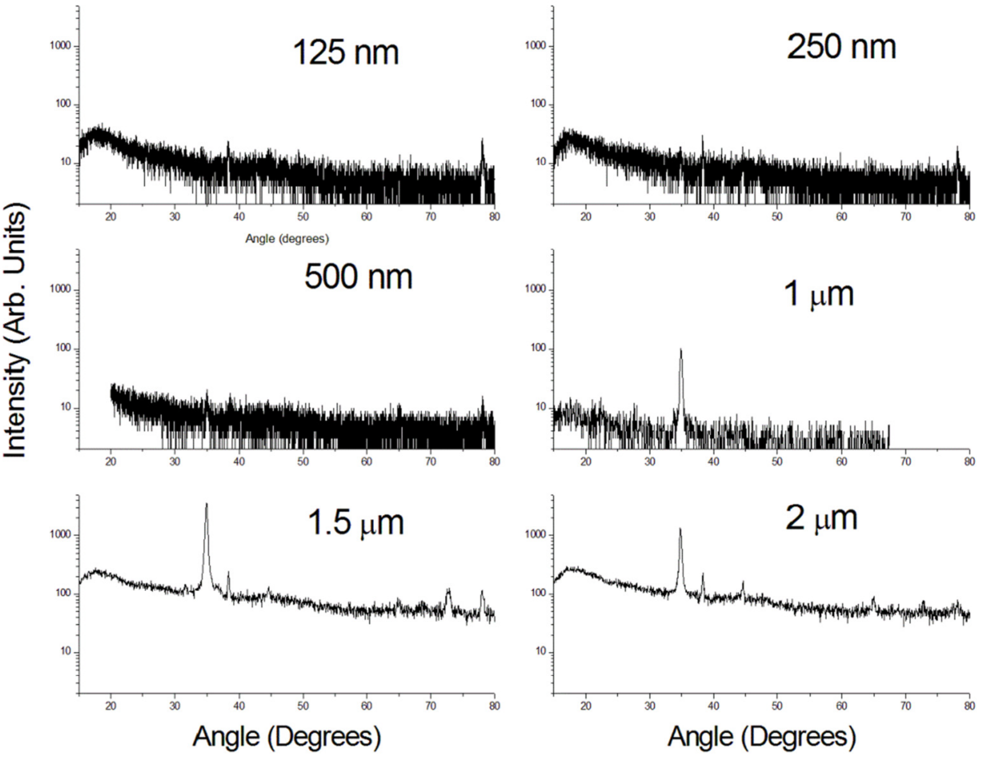

Figure 59: XRD patterns for various zinc oxide thin films

A clear progression is observed, with a peak at 34.8° becoming apparent as film thickness increases, smaller peaks at 38.3° and 44.6° also become visible at greater thickness. This implies that, as films initially form, they have an amorphous structure, like the amorphous structure of the substrate on which they are deposited, while a crystal structure develops as layers of ZnO are deposited on top and orient themselves along the c – axis. Villanueva *et al*, whose work investigates the properties of ZnO films deposited on glass at 250 °C (2006), compare the XRD patterns of layers grown using 6,000 and 24,000 shots, both of which exhibit a peak at 15.5 °, and find that the 24,000 shot sample similarly exhibits a stronger peak, implying a more crystalline structure. Since our work with ZnO and ZnO: Al on Perspex and Kapton was limited to 20,000 shot growths, corresponding to approximately 500 nm, These samples did not exhibit noticeable crystalline structure. As can be seen in figure 60, at 125, 250 and 500 nm no crystal peaks are evident on Perspex or Kapton.

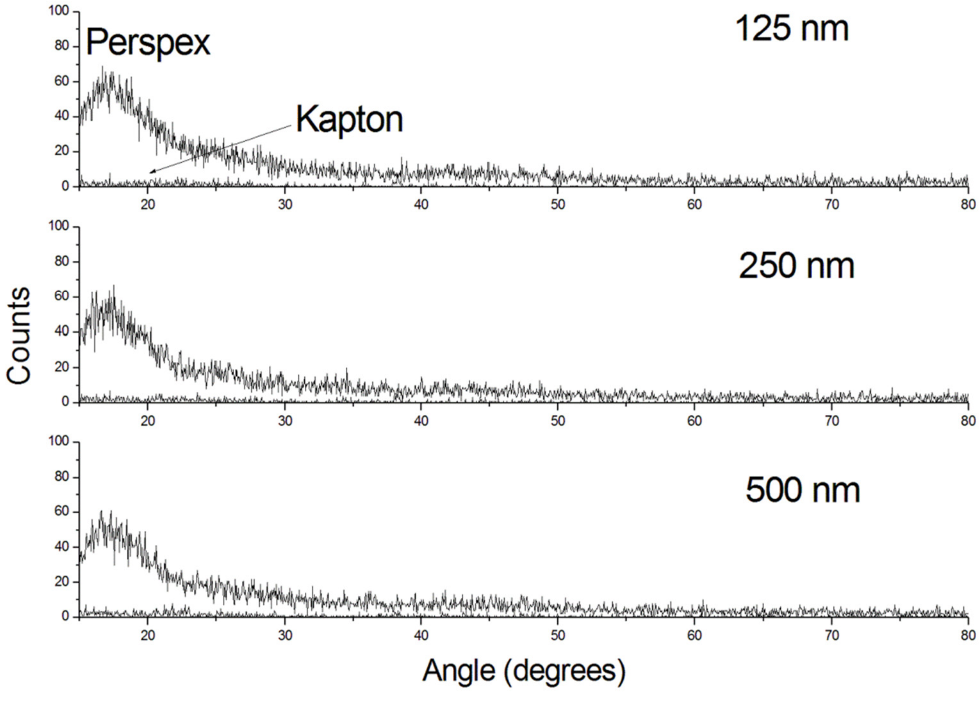

Figure 60: ZnO: Al films grown at 300 mTorr on Perspex and Kapton

Liu, Zhao and Lian (Liu, Zhao and Lian 2006) perform XRD on PLD samples grown at room temperature at a pressure of 9 Pa (≈70 mTorr) as a function of laser fluence. They report that increasing fluence correlates with increasing crystallinity; at fluence values comparable with those used in our experiments (1.0 – 1.4 J cm^2) they observe only small peaks at 37°.

IV.2.c Atomic Force Microscopy:

Analysis of AFM profiles such as those displayed in figures 61 to 67 reveal a homogeneous surface structure, without major features. Samples that have been subject to heat treatment exhibit ridges in the surface at regular intervals, attributed to differences in the rate of thermal expansion of the film and the plastic substrate. After calculating the dimensions of the AFM tip in relation to the dimensions of these features, we are confident that AFM has imaged the bottom of the ridge. These are a surface feature only and do not penetrate the thickness of the film. Apart from these features, the films do not exhibit major or abrupt changes in height. Five AFM images of ZnO, ZnO: Al and Mg ZnO films of various thicknesses grown at various pressures were measured using WSXM software. The average height of the films was found to be 36.7 ± 26.5 nm. Also shown is an AFM image of a 125 nm film of 2% ZnO: Al on Perspex with a cross sectional profile taken along the yellow dotted line. The surface along this cross section has a standard deviation from the mean film position of 6.23 nm while the RMS roughness as calculated by WSXM is 6.95 nm. It should be noted that, in this case, the mean "thickness" of 147 nm does not refer to the actual film thickness, but rather to the vertical distance from the arbitrary starting position of the AFM tip. These results are comparable with results for films of similar thickness grown by Christoulakis *et al* (Christoulakis, et al. 2006). They report roughness values of ≈4 nm for a 100 nm thick film and ≈6 nm for a 150 nm thick film. Ngom *et* al have also reported calculated roughness values of 4.1 ± 0.2 nm for a laser fluence of 1.0 J/cm^2 for tungsten dopes ZnO films (Ngom, et al. 2009). Roughness analysis of a 500 nm sample (figure 61) returns a value of 4.7 nm, showing that, in the range 100 – 500 nm there is no dramatic change in roughness that might suggest the formation of nanostructures.

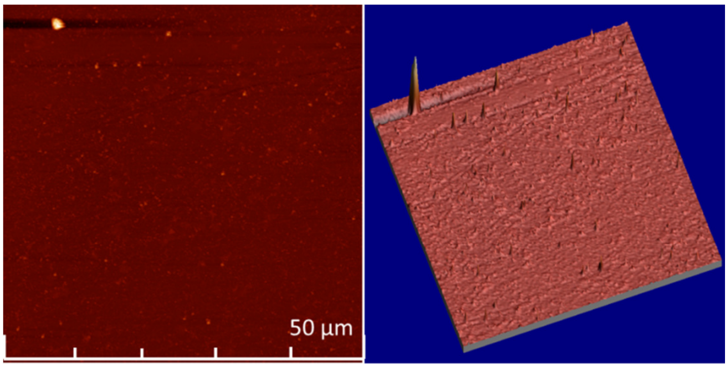

Figure 61: Blank Perspex (a) 2 D image (b) 3 D image (RMS roughness 10.5 nm)

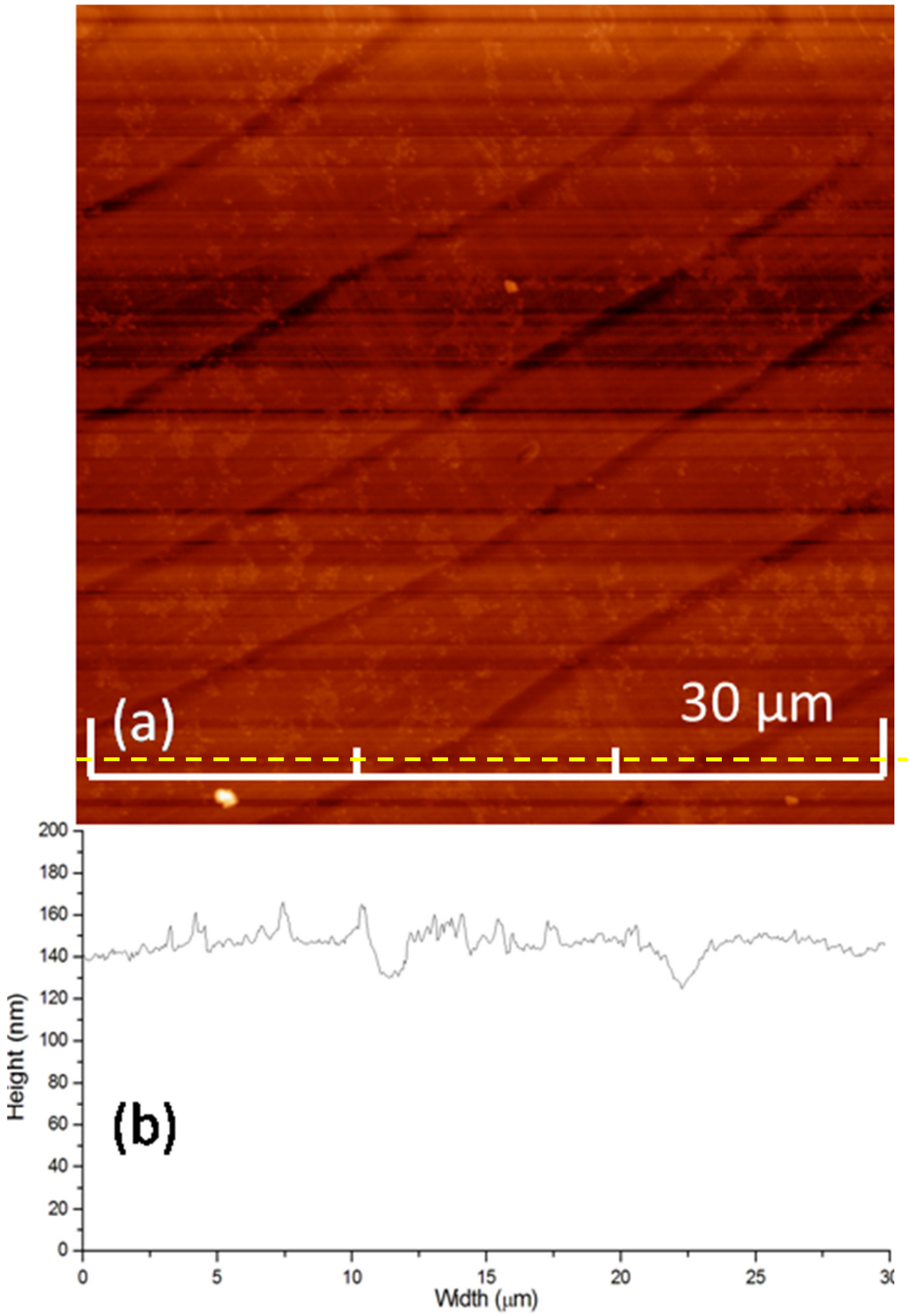

Figure 62: (a) AFM profile of a 125 nm ZnO: Al film grown at 75 mTorr and annealed at 100 degrees (RMS roughness: 16.3 nm)

(b) Line profile of film (yellow dotted line indicates cross section)

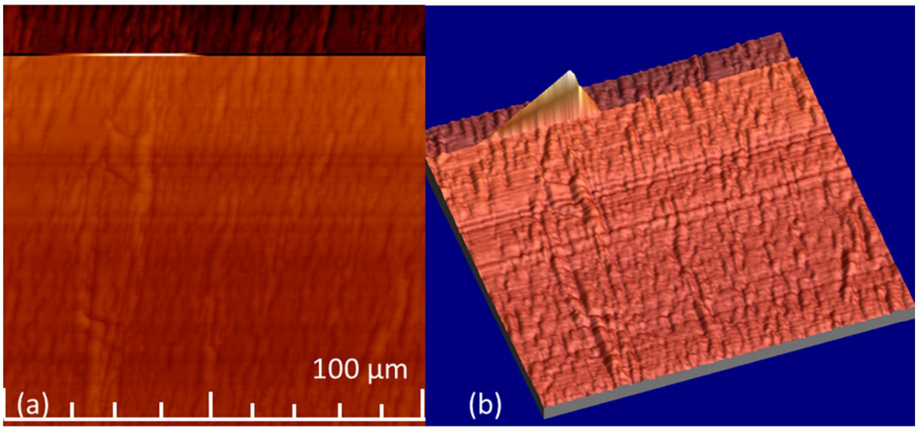

Figure 63: 250 nm ZnO: Al film grown at 10 mTorr annealed at 100 degrees (a) 2l D image (b) 3 D image (RMS roughness: 24.3 nm)

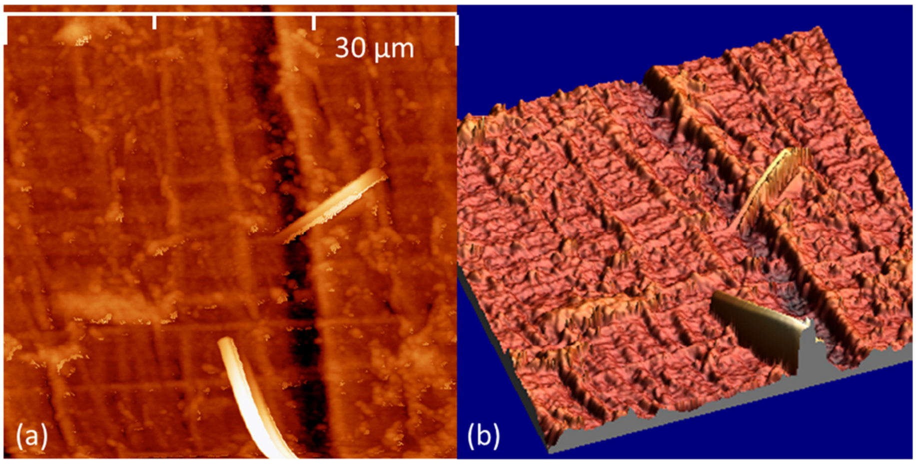

Figure 64: 250 nm ZnO: Al film grown at 30 mTorr annealed at 100 degrees (a) 2 D image (b) 3 D image (RMS roughness: 19.3 nm)

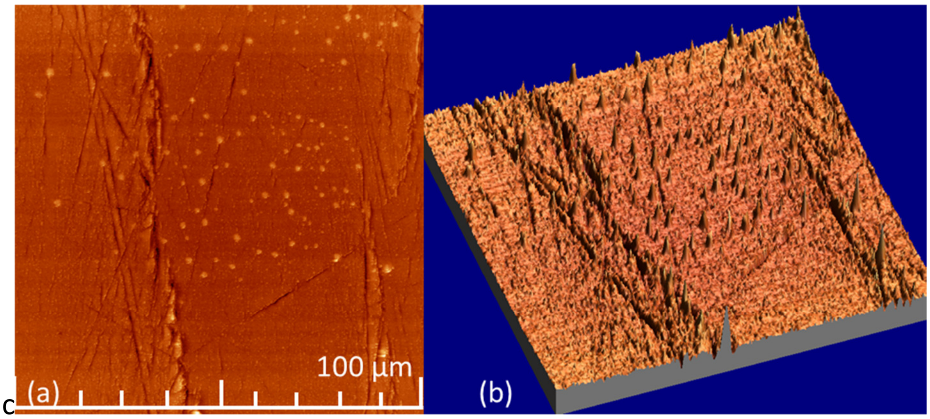

Figure 65: 500 nm ZnO: Al film grown at 30 mTorr annealed at 100 degrees (a) 2 D image (b) 3 D image (RMS roughness: 14.7 nm)

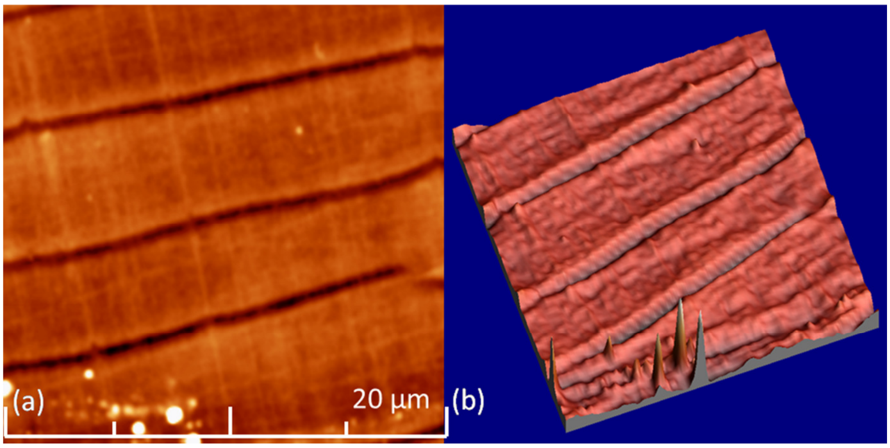

Figure 66: 500 nm ZnO film grown at 150 mTorr, annealed at 100 degrees (a) 2 D image (b) 3 D image (RMS roughness: 5.1 nm)

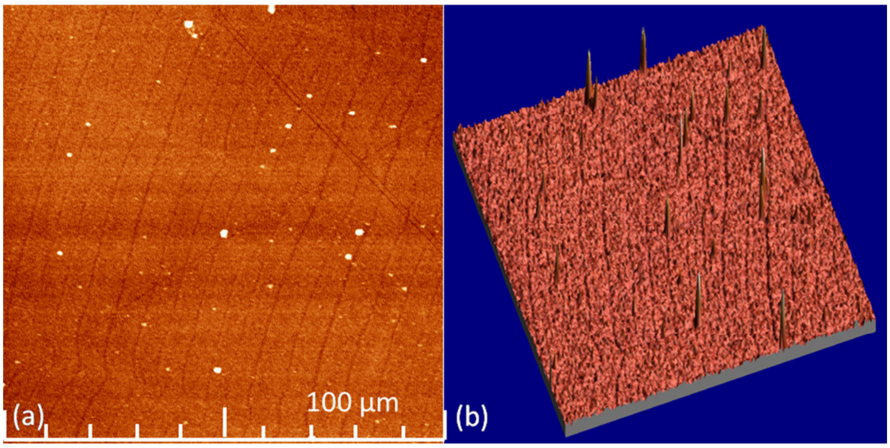

Figure 67: 750 nm Mg ZnO film grown at 300 mTorr; annealed at 100 degrees (a) 2 D image (b) 3 D image (RMS roughness 21.8)

IV.2.d Electrical Properties:

The sheet resistance of samples deposited on PMMA (Perspex^{TM}) and Kapton^{TM} under various conditions was measured with a Van der Pauw 4 point probe, the results are illustrated in figure 68 and 69, separated by substrate and target, and presented as a function of film thickness and growth pressure. Unless otherwise stated, samples on Perspex and Kapton were annealed at 100 ^{O}C in oxygen. The resistivity of zinc oxide films on Perspex and Kapton is given in figure 68. Resistivity ranges from 10^{-2} to 10^{7} Ω cm. Depositions performed at low pressures (1 mTorr and 10 mTorr) exhibit the lowest resistivities. At deposition pressures above 30 mTorr, resistivity varies between 10^{4} and 10^{6} Ω cm. Depositions performed with the same parameters on both Kapton and Perspex exhibit comparable sheet resistance, most samples are within one order of magnitude. Since both substrates are amorphous plastics, and since samples in the thickness range (125 nm – 500 nm) do not show noticeable crystal structure under XRD (section IV.2.b), it is reasonable to infer that films grown on these substrates are primarily amorphous and their electrical characteristics are not governed by their structure. For depositions performed at high pressures, measured resistivity ranges from 10^2 to 10^5 Ω cm. Samples grown at a pressure of 300 mTorr usually have sheet resistance an order of magnitude lower than those grown at 150 mTorr. There is an overall reduction in resistivity at larger film thicknesses, which is most noticeable for both Perspex and Kapton at low pressures (1 – 10 mTorr). This can be attributed to the film having a high metal content at these low oxygen pressures. However, the reduction is also observed at higher pressures on Perspex.

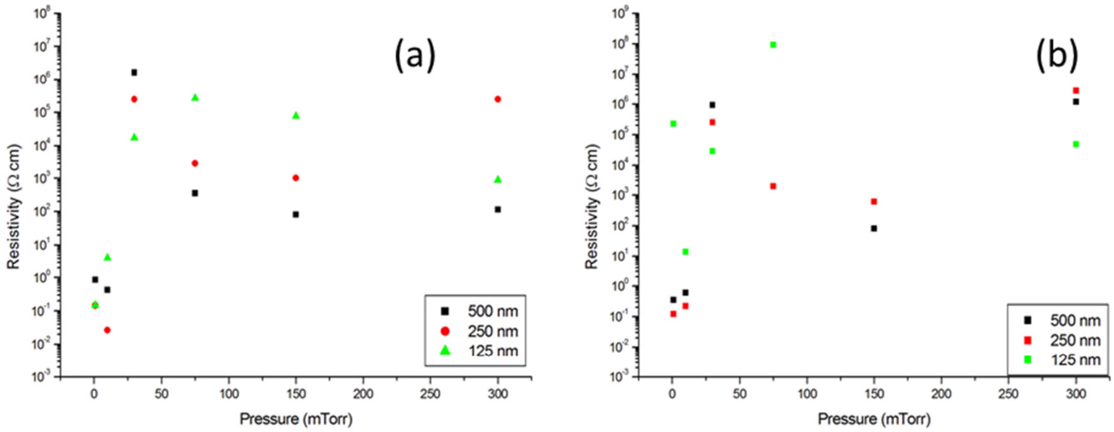

Figure 68: Resistivity of ZnO plotted as a function of growth pressure on (a) Perspex (b) Kapton

Electrical measurements for ZnO: Al on Perspex and Kapton are given in figure 69. Resistivity for the doped target ranges from 10^{-2} to 10^7 Ω cm. The depositions performed at the lowest oxygen pressure returned significantly lower values. The range of sheet resistances is comparable with undoped ZnO, however a slightly larger number of samples exhibit resistance at the low end of this range and the most conductive samples were ZnO: Al films grown at 1 or 10 mTorr. Similarly to ZnO films, there is typically a decrease in resistivity as film thickness increases for all growth pressures, with the lowest growth pressures (1 – 10 mTorr) exhibiting the lowest values. Again, this is attributed to a metal rich film being formed at low pressures.

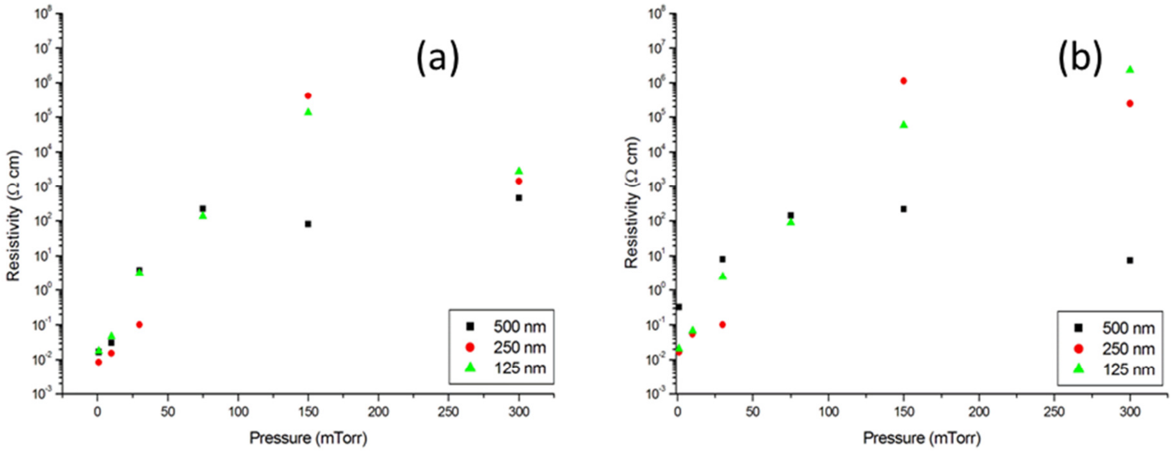

Figure 69: Resistivity of ZnO: Al by growth pressure on (a) Perspex (b) Kapton

Table 10: Characteristics of Mg ZnO on Perspex

Thickness (nm)	Target	Pressure	Heat	Substrate	Sheet resistance (Ω)	Resistivity (Ω cm)
1250	Mg ZnO	75	--	Perspex	Unable to measure	N/A
1000	Mg ZnO	75	--	Perspex	1.40×10^{10}	1.4×10^{6}
750	Mg ZnO	75	--	Perspex	Unable to measure	N/A
750	Mg ZnO	150	--	Perspex	1.90×10^{10}	1.425×10^{6}
750	Mg ZnO	300	--	Perspex	1.10×10^{11}	8.25×10^{6}
500	Mg ZnO	150	--	Perspex	Unable to measure	N/A
500	Mg ZnO	150	--	Perspex	2.40×10^{10}	1.2×10^{6}
500	Mg ZnO	300	--	Perspex	Unable to measure	N/A
250	Mg ZnO	75	--	Perspex	Unable to measure	N/A
250	Mg ZnO	150	--	Perspex	Unable to measure	N/A
250	Mg ZnO	300	--	Perspex	Unable to measure	N/A
125	Mg ZnO	150	500	Silicon	Unable to measure	N/A
125	Mg ZnO	150	500	Silicon	8.60×10^{7}	2.15×10^{3}
125	Mg ZnO	150	600	Silicon	1.90×10^{7}	4.75×10^{2}
125	Mg ZnO	150	700	Silicon	6.70×10^{7}	1.68×10^{3}

Table 10 contains the results of electrical characterisation of magnesium zinc oxide thin films. As can be seen, attempts to measure sheet resistance on Mg ZnO samples were generally not successful, with “Measurement Failure” being reported by the instrument on multiple occasions. We believe that this is due to high contact resistance interfering with the measurement. The few successful measurements indicate similar values to those measured for ZnO and ZnO: Al at similar oxygen pressures. Mg ZnO films grown at high temperatures (> 500^{o} C) in silicon exhibited sheet resistances comparable with undoped and aluminium doped ZnO films grown at 100^{o} C.

There is not a great deal of literature available with which to make comparison with the higher deposition pressures investigated in this work (75 mTorr – 300 mTorr), most researchers confine themselves to values in the 1 mTorr range. However, K.L. Narasimhan *et al* report on the electrical properties of zinc oxide films of 300—to 350 nm thickness grown using PLD on glass substrates at oxygen pressures up to approximately 300 mTorr. They report resistivity of $\approx 3.16\times10^{-3}$ Ω cm at a pressure of 10 mTorr when grown at room temperature; this is one order of magnitude lower than our results for a film of ≈500 nm grown at 10 mTorr. Narasimham also reports significant increases in sheet resistance at pressures of 100 mTorr at room temperature, reporting a value of $\approx 10^{3}$ Ω cm (1997). This compares favourably with our results for ZnO films of 250 nm and 500 nm, which have resistivities of 3.57×10^{2} and 3×10^{3} Ω cm, respectively. A similar dramatic increase is observed in our own results, taking place at pressures between 1 and 10 mTorr. Resistivity values for 1 mTorr are approximately 10^{-1} Ω cm at several thicknesses but increase substantially above 10 mTorr. An increase of resistivity is also reported by Singh and Mehra; who grow aluminium doped zinc oxide on quartz and Corning glass from 25^{o} C to 300^{o} C. They observe that from oxygen pressures less than 0.5 mTorr to 1 mTorr, resistivity decreases and reach a minimum of 7.3×10^{-4} Ω cm at 1 mTorr before climbing again (2001). The work of Singh and Mehra is focused on the pressure range up to 10 mTorr. They also do not report on film thickness, making it impossible to directly compare sheet resistance values. However our films of several thicknesses grown at 1 mTorr exhibit a resistivity of 5.5×10^{-1} Ω cm. Both Narasimham and Singh observe that resistivity is decreased by applying heat during deposition, indeed Narasimham exhibits values that show an improvement of as much as four orders of magnitude at pressures of 100 mTorr, while Singh reports a more modest but consistent improvement of one order of magnitude. In general, we observed some decrease in sheet resistance when comparing heated and non-heated samples, but reductions were generally within an order of magnitude. Due to the melting point of PMMA

(≈160 ^{O} C) it was not possible to apply significant heating to thin films deposited on PMMA substrates, however, we observed significant improvements in resistivity when films were deposited on glass substrates and annealed at 500 ^{O} C; glass samples grown at 300 mTorr exhibited an average value of 13.8 Ω cm compared to samples grown at room temperature that had a resistivity of 3416 Ω cm, a reduction by a factor of 250. This is attributed to improvement in the crystal structure due to the energy supplied by high temperature.

An improvement of approximately two orders of magnitude is reported by Mass, Bhattacharya and Katiyar (2003) when samples were grown using an Al-doped target with concentrations up to 2%. Liu and Lian (2007) examined the electrical properties of ZnO: Al thin films on glass at 11 Pa (82.5 mTorr) as a function of dopant concentration (as a percentage by weight). They report a resistivity of $\approx 1\times10^{-3}$ Ω cm for a 2% Al dopant, the same as used in the experiments reported here. This is 4 to 5 orders of magnitude lower than the resistivity values we report for an equivalent pressure (75 mTorr), deposition temperature in this paper is given as 150 ^{O} C, which we do not believe is significantly higher than our deposition temperature (100^{O} C) to account for this difference. However, Liu and Lian state that the target-substrate distance in their system was 2.3 cm, roughly half the distance in our own PLD system, which may significantly change how the plasma interacts with the substrate as compared to our system. It is interesting to note that these authors reported the lowest resistivity measurements at an Al concentration of 2%, with both lower and higher concentrations returning resistivities at least one order of magnitude higher. Park, Ikegami and Ebihara (2005) grow 200 nm ZnO: Al films on glass substrates at 500 ^{o} C; they report a resistivity of 5.14×10^{-4} Ω cm at 1 mTorr, 7.5×10^{-4} Ω cm at 10 mTorr and 5.22 Ω cm at 100 mTorr. The results at 1 and 10 mTorr are two orders of magnitude lower than those we report, it should be noted that Park *et al* perform depositions at a temperature of 500 ^{O} C, a temperature that, as has been noted, is not possible on PMMA substrates. It should also be noted that a significant increase in resistivity is observed for pressures above 50 mTorr, which shows similarity with similar increases reported in this work, as well as in the work of Narasimhan (1997) and of Singh and Mehra (2001) as mentioned previously.

IV.2.e Water Contact Angle:

Water contact angle measurements were performed on thin film samples as described in the experimental section of this thesis. Water contact angle measurements for ZnO and ZnO: Al are plotted as a function of growth pressure in figures 70 and 71.

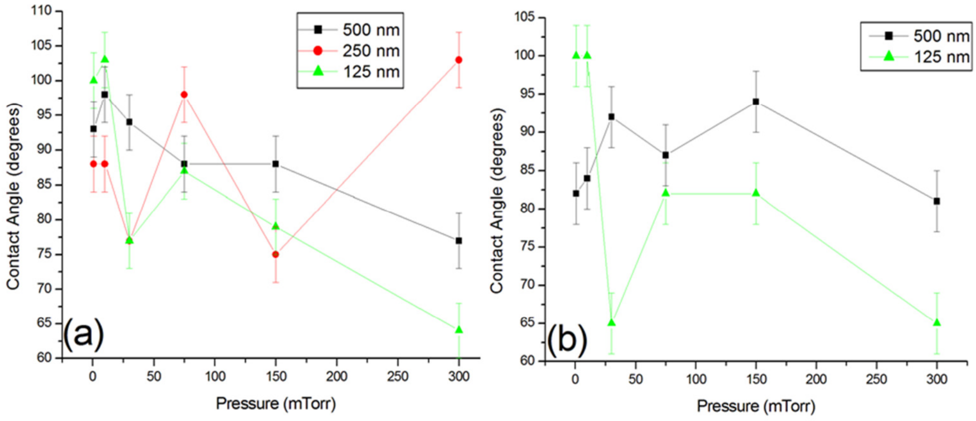

Figure 70: Water Contact Angle measurements for ZnO on (a) Perspex and (b) Kapton as a function of Growth Pressure

It is observed that contact angle for zinc oxide at low growth pressures are in the range 90^o to 105^o, as growth pressure increases there is a downward trend, indicating samples become more hydrophilic. The greatest reduction is in 125 nm films, which return a contact angle of 64^o at 300 mTorr on Perspex and 65^o on Kapton. Results of Perspex and Kapton show a comparable reduction.

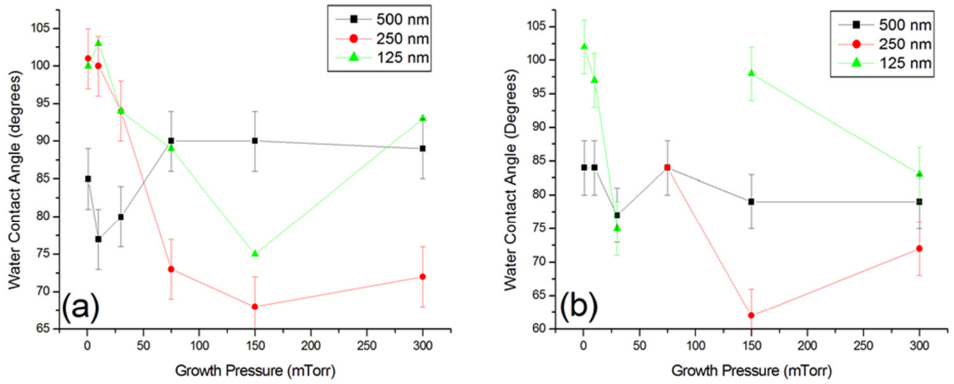

Figure 71: Water Contact Angle of ZnO: Al on (a) Perspex and (b) Kapton as a function of growth pressure

ZnO: Al films show results that are comparable to those of ZnO, and show a similar reduction in contact angle with increasing pressure. This drop is most apparent in the 250 nm samples, which reach a minimum contact angle of about 70°. These results seem to be in line with contact angles reported for thin films grown by other researchers. Se Jin Kim reports a contact angle of 76° in his thesis (S. J. Kim 2008). A comparable value of "close to 80°" is reported for ZnO grown on silicon at 40 mTorr at 650° C by Papadopoulou *et al* (Papadopoulou, Barberoglou, et al. 2009). In another paper, Papadopoulou *et al* (Papadopoulou, Pagkozidis, et al. 2010) report that the measured water contact angle is 95°, for a 100 nm thick ZnO film grown at ≈4 mTorr at 650° C. There is a change of ≈15° between samples grown by the same group at similar growth conditions, save for the change in pressure. This agrees with the range of contact angles measured for 20,000 shot films grown from 1 to 300 mTorr using both ZnO and ZnO: Al targets. In the case of the ZnO target, contact angles range from 77° to 98° with a mean value of 92° and a standard deviation of 4°. Similarly, for the ZnO: Al target, values range from 77° to 90°, the mean angle is 85° with a standard deviation of 6°. It should also be noted that the thinnest films grown at 5,000 shots exhibit contact angles of ≈100° at low pressure (1 – 10 mTorr) when grown with ZnO and ZnO: Al targets on both Perspex and Kapton substrates.

These results are important in the context of the growth of microbial films, as it is important to ensure that the surface is sufficiently hydrophilic that the film will adhere. However, in order to maximise the number of organisms in a given area, it is important to limit the hydrophilic nature of the film, as microbes will "spread out", illustrated in figure 72, which shows a dense microbial film (a), and a sparse film, likely due to the hydrophobic surface inhibiting adhesion by the bacteria.

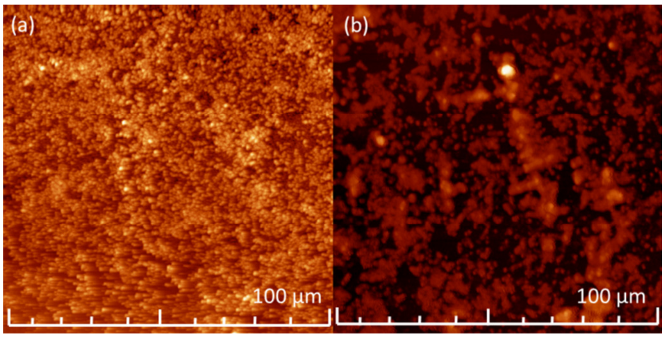

Figure 72: AFM images of biofilm on thin film substrate

IV.2.f Bacterial Electrical Measurements:

Microbial Biofilm Voltammetry (MBV) experiments were performed on a selection of ZnO, ZnO: Al and Mg ZnO samples grown by PLD by our colleagues from the DCU School of Biotechnology. These results were compared with those of bacteria grown on a commercially available ITO thin film. In the *G. sulfurreducens* experiment with ITO coated electrode, application of a potential of 0.242 V vs. SHE to the working electrode resulted in a constant current increase as shown in figure 58, indicating attachment and growth of the biofilm , continuous oxidation of acetate (the electron donor) and subsequent reduction of ITO electrode. The initial exponential increase in the catalytic current reached a plateau of 12.5 µA/cm^2 after 48 hours and did not increase further when the spent growth medium was replaced. This is an indication that the biofilm has reached a “saturation phase” (E. Marsili, J. B. Rollefson, et al. 2008). CV of *G. sulfurreducens* biofilms, shown as an insert in figure 75 at different growth stages, show a typical sigmoidal wave with an onset at - 0.2 V vs. SHE. Similar current patterns were observed in *G. sulfurreducens* biofilms formed on glassy carbon electrode.

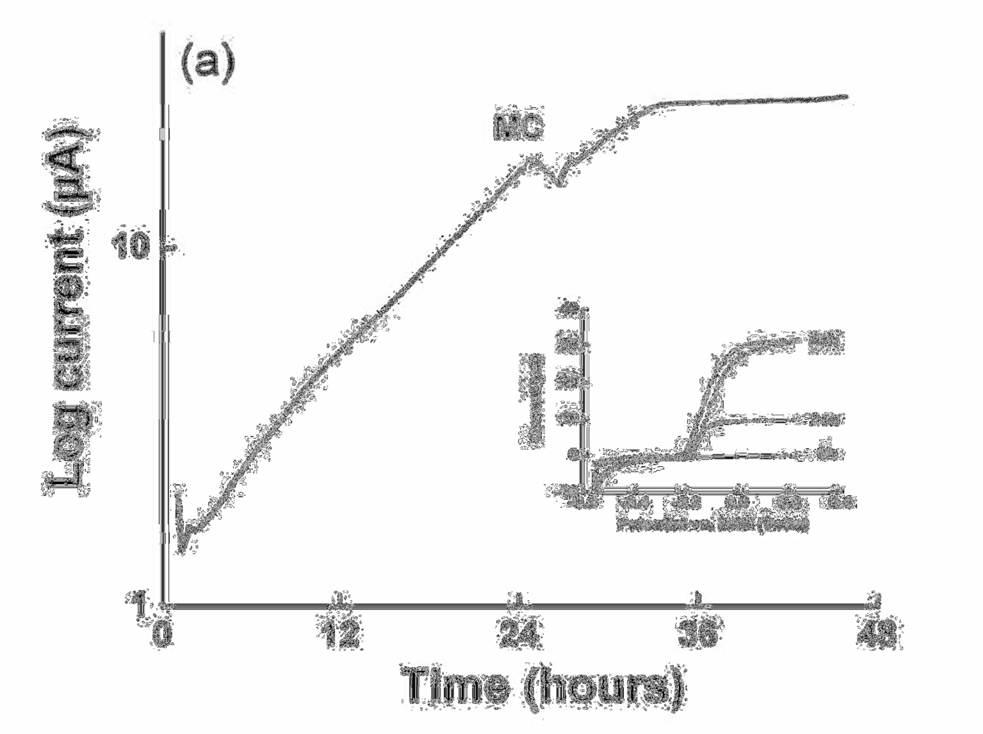

Figure 73: CA and (insert) CV measurement of G.sulfurreducens on ITO

In a similar experiment using *G.sulfurreducens* with ZnO as the working electrode, no current production was observed. This is possibly due to the antimicrobial properties of ZnO which are attributed to the formation of reactive oxygen radicals at the interface. This might have resulted in the disruption of the cell membrane of *G. sulfurreducens*, thereby blocking the EET process. It is known that biofilms of facultative bacteria such as *E. coli* are more resistant towards the oxidative stress induced by reactive oxygen species. Moreover, electroactivity in *E. coli* biofilm has been demonstrated (Zhang, et al. 2008). Therefore, our colleagues chose to grow the facultative *E.coli* on 136 nm ZnO film electrodes, under the same conditions adopted for *G. sulfurreducens*. To increase extracellular electron transfer (EET) between *E.coli* biofilm and ZnO electrode, 0.5 µM of anthraquinone-2, 6-disulfonate (AQDS) was added as a redox mediator. Glucose was added as electron donor to the non-limiting concentration of 11 mM. A sustained current was observed during the CA, shown in figure 76, indicating continuous oxidation of glucose and electrochemical reduction of the working electrode. The pattern of current production development was significantly different from that observed during the *G. Sulfurreducens* experiments. The current initially showed an exponential increase, with a maximum value of 1.3 µA/cm^2. After approximately 12 hours, the current started to decrease due to exhaustion of glucose in the medium. The current production was resumed upon replacement of the spent growth medium and did not change significantly upon repeated media changes (MC). The CV shown as an insert in Fig.76 did not present a pronounced sigmoidal pattern.

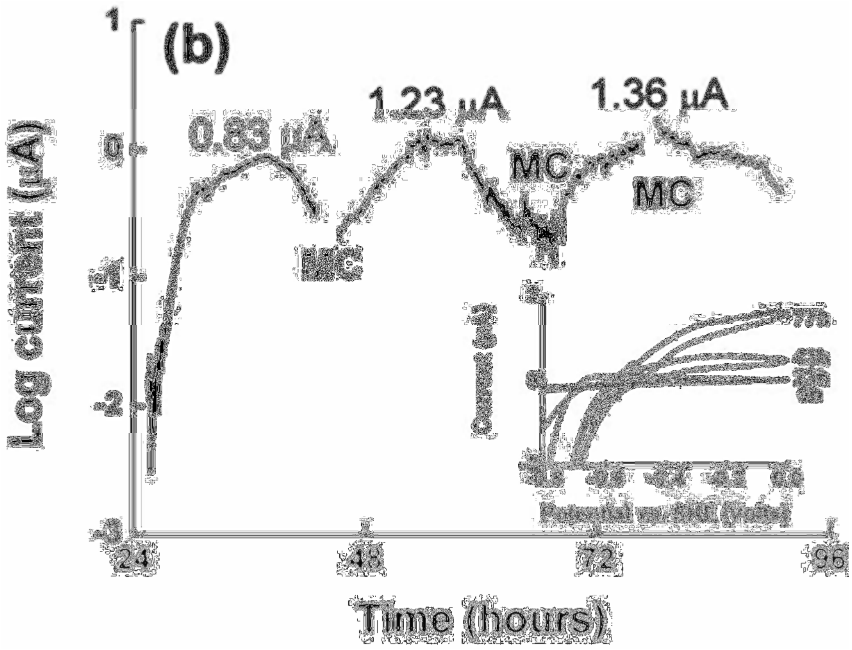

Figure 74: CA and (insert) CV measurement of E.coli on ZnO

The performance of *Shewanella loihica* grown on ZnO films was also compared to that of a similar film grown on ITO, which is illustrated in figure 77. ITO initially exhibited a current density of approximately 0.5 μA/cm^2, which decreased to approximately 0.3 μA/cm^2 over 24 hours. At this point, the growth medium was changed in order to promote biofilm growth. The measured current density increased to approximately 1.8 μA/cm^2. There was a sharp reduction in the current density over the following 24 hours, and the current density at the time of the second medium change is approximately 0.8 μA/cm^2. After the second medium change, the current density climbs steadily and peaks at a value of 2.5 μA/cm^2 before decreasing sharply to a value of about 1.8 μA/cm^2. A similar increase is observed after the third medium change, with the current density reaching its peak value of 3.5 μA/cm^2 after approximately 84 hours, before beginning to decrease. Similar behaviour was observed for *E.coli* biofilms grown on ZnO thin films but not for *G. sulfurreduccens* grown on ITO (see above). The increase in current density observed after the second and third changed of growth medium are attributed by our colleagues to the “catalytic oxidation of lactate in the EAB” while the subsequent decrease is “likely due to the exhaustion of the lactate in the medium and/or to a pH change due to an accumulation of metabolic end products“ (Connolly, et al. 2011). It is unclear whether the peak current density observed is indicative of a “saturation phase” as described for *G. Sulfurreducens* on ITO as no current density plateau is observed to occur. It should be noted that this CA measurement is performed over 96 hours, rather than the 48 hours of that measurement.

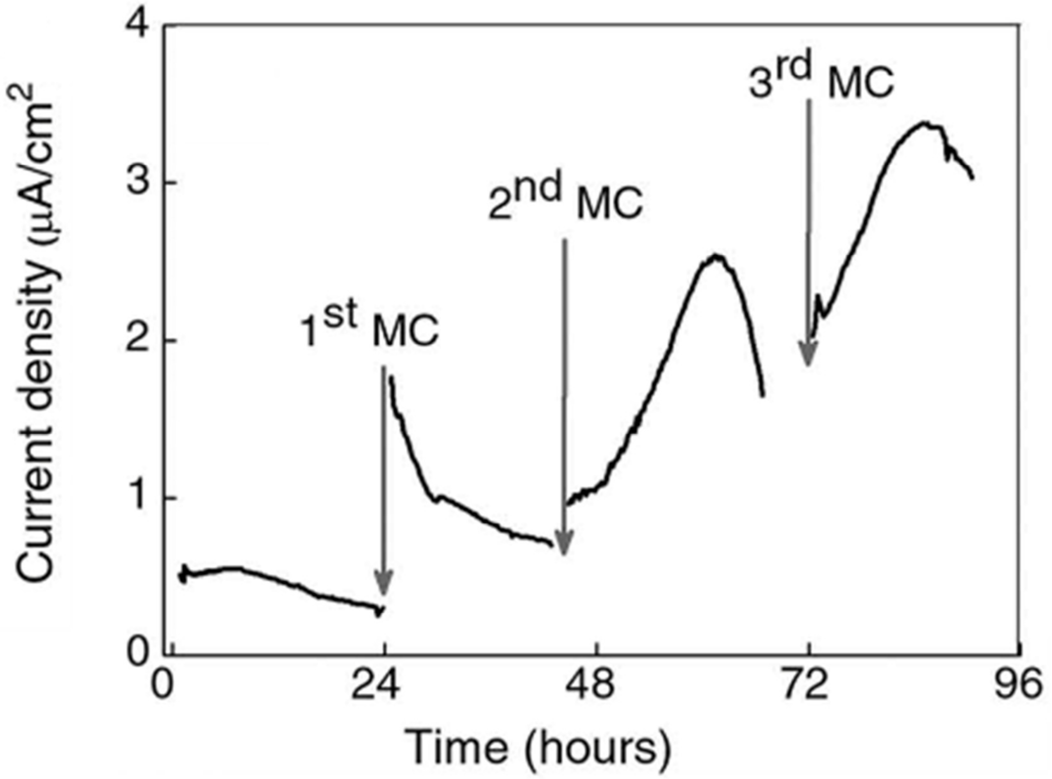

Figure 75: CA measurement of S.loihica on ITO

The behaviour of *S.loihica* on ZnO is markedly different, as shown in figure 78. The absolute current density that was measured is 0.25 μA/cm^2, a value which is an order of magnitude lower than on ITO. The current density climbs steadily for approximately 8 hours to a value of ≈0.035 μA/cm^2. Subsequently, it decreases slightly before recovering and rising to ≈0.09 μA/cm^2, this is followed by a slight decrease which soon recovers. A steady increase in current density is observed, which continues after the growth medium is changed. The peak value (0.25 μA/cm^2) is reached and decreases at a low rate over the following twelve hours. After approximately sixteen hours (64 hours in total), there is a marked drop in current density which continues after the second change of the growth medium. The current density reaches a minimum value after three days (72 hours total) before briefly increasing to approximately 0.18 μA/cm^2. The more modest current density is attributable to the higher hydrophobicity of the ZnO films (the films used in these experiments have a

WCA of 92°, compared to 74° for ITO). It is possible that the lower surface roughness also contributed (ITO films used had a measured surface roughness of 12 nm, while the ZnO films had a roughness of 2 nm), which our colleagues believe inhibits adsorption of the membrane cytochromes on the electrode, lowering the measured current density. It should also be noted that the higher sheet resistance of ZnO films compared to ITO films could be a limiting influence on the production of current at the interface between the electrode and the biofilm. There is no correlation between current density increase and the change in growth medium, which indicates that the decrease in current density is not due to exhaustion of the electron donor. There is also no observed "saturation phase" in which the current density level reaches a plateau.

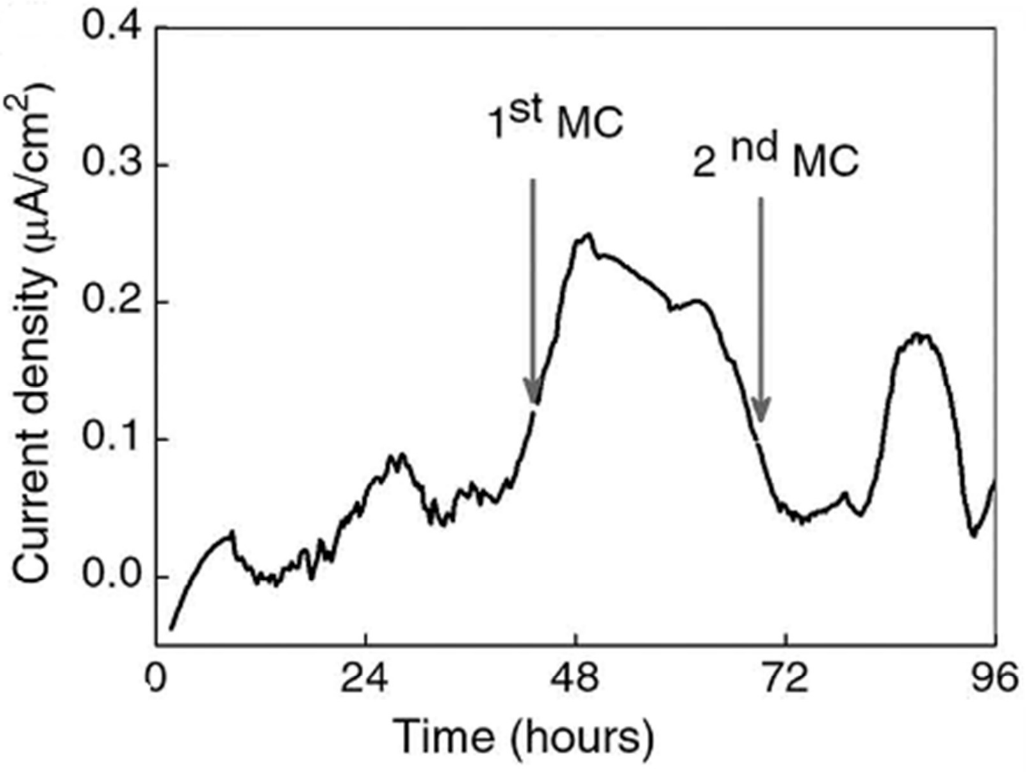

Figure 76: CA measurement of S.loihica on ZnO

To perform MBV, the samples were subjected to a variable sweeping voltage at intervals over a span of days and their current density recorded as a function of applied voltage. The current density curve for *Shewanella loihica* grown on ITO traces a sigmoidal curve. At the initial applied potential of -0.8 V, the current density at 43 hours is measured as -0.5 μA/cm^2. It approaches 0 μA/cm^2 very gradually as the potential is increased towards the positive. At approximately -1.5 µA/cm^2, the current density increases at a greater rate and peaks at a value of approximately 1 µA/cm^2 at a potential of +0.2 V. The potential is then reversed, and the current density follows a similar pattern. When the experiment is performed with cultures incubated for 67 and 90 hours, the sigmoidal pattern is more pronounced, and the peak current density is significantly higher; 4 µA/cm^2 and 9 µA/cm^2 respectively. This can be seen in figure 79. The behaviour of *Shewanella loihica* on ITO is similar to results the same researchers reported for *Shewanella* grown on graphite electrodes (Jain, Zhang, et al. 2012) and indicate that electron transfer is by a combination of direct transfer between the film and the electrode, and mediated transfer of electrons by redox mediators (flavins).

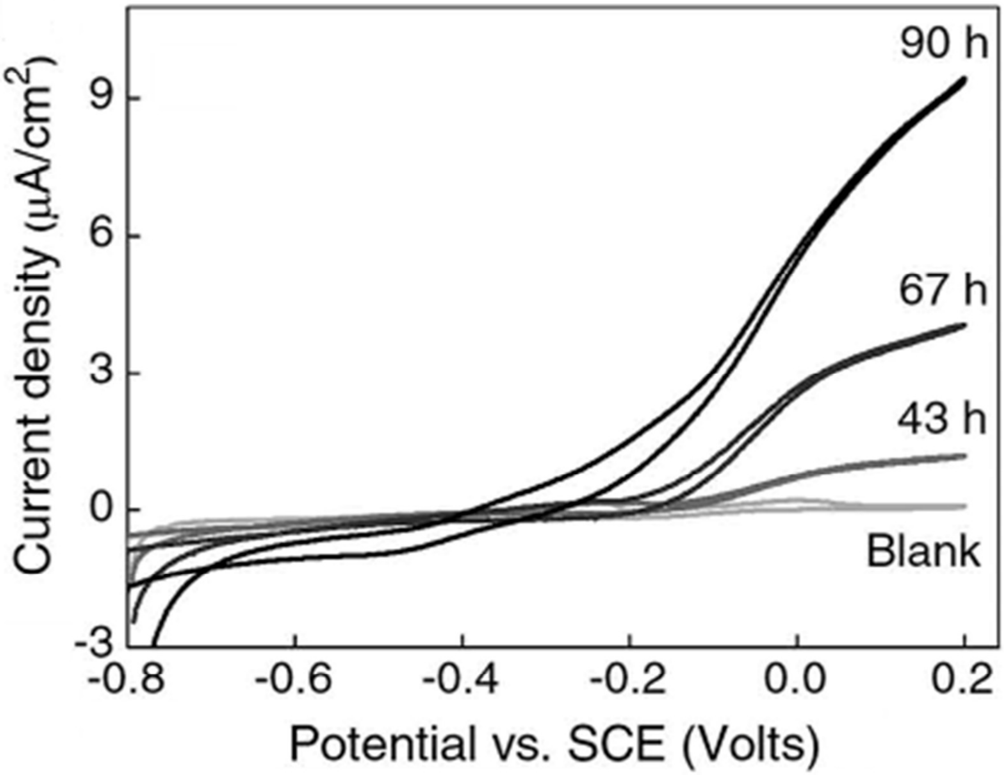

Figure 77: CV measurement of S.loihica on ITO

The behaviour of Shewanella on zinc oxide was notably different. When a potential of -0.8 V is applied, the measured current density is -1.5 µA/cm^2. This decreases (towards zero) as the potential goes from -0.8 to -0.6 V, and then briefly stabilises. At -0.45, the current density reduced again at a greater rate. At approximately -0.2 V, the reduction in current density became less severe and reaches 0 µA/cm^2 at a potential of approximately -0.1 V.

The current density continues past 0 µA/cm^2 and increases as a positive potential is applied, reaching a value of 0.6 µA/cm^2 at the maximum voltage of +0.2 V. At this point the applied potential is reversed. The current density reduces slightly as the potential drops, reaching a value of 0.5 µA/cm^2 before beginning to rise again. The peak current density of 1 µA/cm^2 is reached at a potential of -0.25 µA/cm^2. From this point, the current density reduces at a steady rate until reaching 0 µA/cm^2 at a potential of -0.7 V. The current density continues past 0 µA/cm^2 and reaches a peak negative current density at -0.8 V. CV behaviour is illustrated in figure 80.

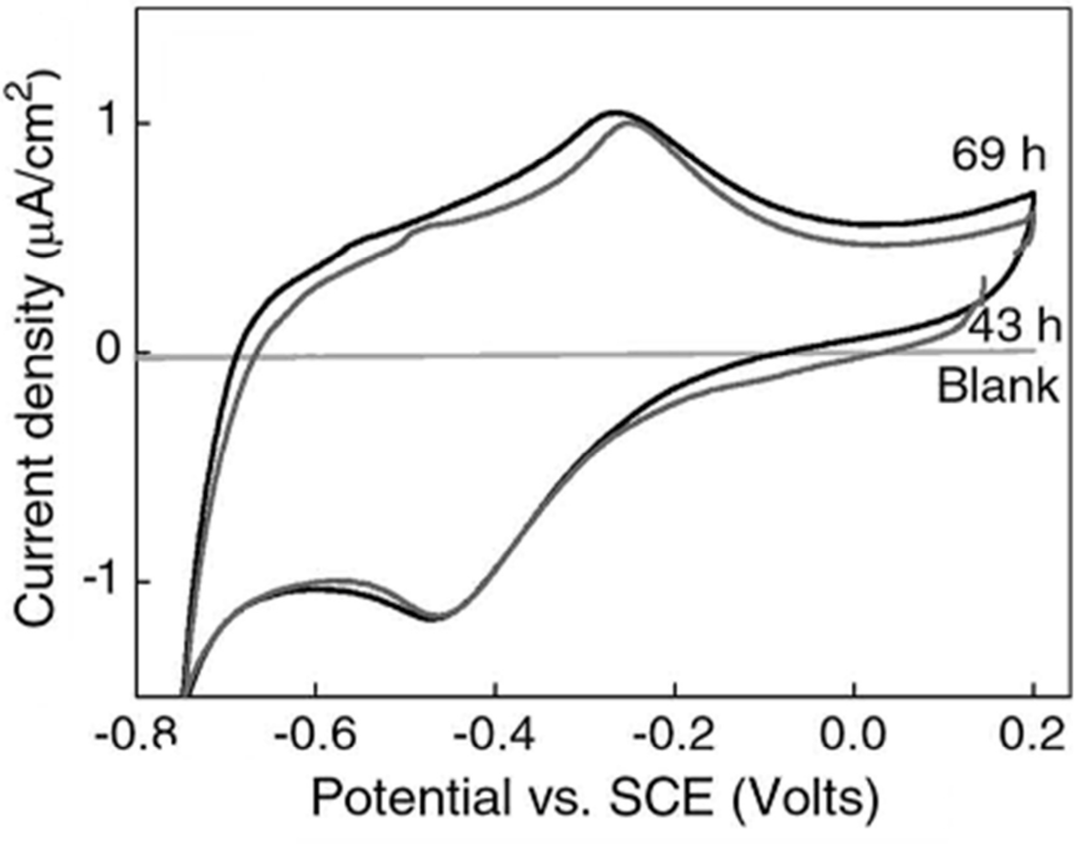

Figure 78: CV measurement of S.loihica on ZnO

Samples that were tested had been incubating for either 43 hours or 69 hours. The current density in both experiments did not deviate significantly from this pattern, with only small changes in current density values (0.1 µA/cm^2). The smaller current density measurements could again be attributed to the higher hydrophobicity and lower surface roughness when compared with ITO, which could inhibit the adsorption of the membrane cytochromes on the electrode, lowering the measured current density. The current density is measureable, however, and is of a level that would encourage further investigation into optimisation of film characteristics.

Chapter V: Conclusions and Outlook

V.1 Dielectric Barrier Discharge Experiment:

A prototype dielectric barrier discharge system was constructed, consisting of a 15 kV voltage source. This system was characterised using voltage, current and charge measurement to measure the plasma parameters over a large range of electrode separations. This revealed a microdischarge current pattern, characteristic of a dielectric barrier discharge in the filamentary regime. The change in the behaviour of the voltage, current and charge was observed through changes in these signals, and it was concluded that the plasma remained a DBD over this range of separations. The power coupled into the discharge, capacitance of the plasma, breakdown voltage, transferred charge and reduced field strength were obtained by electrical measurement. The effect of plasma treatment of the polyethylene material of the bag was investigated with water contact angle measurement. It was found that exposure to the plasma caused the surface to become more hydrophilic, with a reduction in contact angle from 96.3^o to 54.6^o. this was attributed to the material combining with oxygen in the presence of the plasma.

UV-vis Emission spectroscopy was used to create a thorough list of identified emission bands and their associated molecular species from. Intense emission bands from N_2 and N_2^+, and weak emissions from NO, OH, He, O, O_2 and O_2^+ were identified and their wavelength, transition and emission species catalogued. Using intensity calibrated emission spectroscopy; estimates were made of the electronic, rotational, vibrational and translational temperatures using the computer code SPECAIR. These estimates compared favourably with values reported in the literature. Estimates of vibrational temperature were also made via the Boltzmann plot method.

The work presented in this thesis was concerned with the optimisation of the atmospheric pressure dielectric barrier discharge as a novel method of in-situ decontamination of fresh produce. In collaboration with our colleagues in the DIT School of Food Science, experiments were performed with a view to establish the main physical/chemical mechanisms responsible for microbial inactivation. Samples of *E. coli* and its isogenic mutants Δ*dnaK*, Δ*soxR*, Δ*soxS*, Δ*oxyR* and Δ*rpoS* were placed inside the bag, outside the plasma stream and exposed for five minutes. A 1.5 log reduction was observed for bacterial samples placed outside the plasma stream. Microbial recovery post treatment was also assessed. This is of importance, since most produce will be stored after decontamination. Post-treatment storage studies showed the parent strain to recover faster than the Δ*oxyR*, Δ*rpoS* mutants, indicating that some transcription regulators and specific genes related to oxidative stress, like DnaK, play an important role in the *E. coli* repair mechanism (Connolly, et al. 2013).

There are several avenues along which this work could be continued. Newer models of DBD behaviour that take into account stray capacitances, such as have been proposed by Falkenstein and Coogan (1997) could be implemented, lending further insight to the behaviour of the plasma. There are also interesting DBD models that treat the reactor as an equivalent dynamic capacitance, the value of which can change by several orders of magnitude over a period (Zhang, et al. 2010) (Valdivia-Barrientos, et al. 2006) (Flores-Fuentes, et al. 2009).

This work used a voltage source of 15 kV, which was higher than many systems reported in the literature. The effect of still higher voltages (> 30 kV) are not widely reported, but are crucial in order to form plasma in air at large electrode separations (>30 mm). It is suggested that there should be an investigation of the effects of higher voltage levels on plasma parameters, species concentrations and notably the expected increase in bacterial inactivation.

Emission spectroscopy proved to be a valuable tool in the characterisation of this plasma, revealing the excited radiating species present. The implementation of specific spectroscopic techniques such as absorption spectroscopy and LIFS could be useful to elucidate the structure and dynamics of the main oxidative species including ozone.

This system offers the promise of a novel method of decontamination that could be extremely versatile. For that reason, the effect on plasma parameters of changes in, for example input power, electrode surface area, electrode separation and constituent gas could be examined. The effect of different gas compositions should concentrate on those that are of interest to the packaged food industry i.e. Modified Atmosphere (MA). Finally, the effects of the plasma treatment of the appearance, taste and other food quality parameters should be investigated.

V.2 Thin Films Experiment:

Thin films of zinc oxide (ZnO) Magnesium doped zinc oxide (Mg ZnO) and Aluminium doped Zinc Oxide (ZnO: Al) were prepared by pulsed laser deposition at a range of temperatures from 1 mTorr to 300 mTorr. These films were then characterised using X-ray Diffraction (XRD), Water Contact Angle (WCA), Atomic Force Microscopy (AFM), surface profilometry and Van der Pauw resistivity measurements. XRD and AFM characterisation showed films did not exhibit crystal structure. Electrical properties and hydrophobicity were found to be comparable to those reported in the literature for doped and undoped ZnO films.

In collaboration with colleagues in the DCU School of Biotechnology, electroactive biofilms were grown upon them and the electrical output of the biofilms measured over several days, using cyclic voltammetry (CV) and the chronoamperometry (CA). The results were compared with the same strains of bacteria grown on commercially obtained ITO films, which represent the “state of the art” in optically transparent, electrically conductive oxide films. It was shown that certain strains of aerobic bacteria (*Geobacter sulfurreducens*) did not grow successfully on ZnO. It was hypothesised that this was due to the formation of oxygen radicals at the EAB interface. However, other more robust strains (*Escheria coli*) were found to grow successfully on ZnO and generate a measureable current output. *E. coli* biofilms achieved a peak current density of 1.36 $\mu A/cm^2$. Growth of *Shewanella loihica* on ZnO films also successfully generated a measurable current density of 0.25 $\mu A/cm^2$.

This work showed that ZnO deposited on plastic substrates using pulsed laser deposition are suitable for electrochemical characterization of facultative EAB forming strains. ZnO thin films with increased hydrophobicity and lower resistivity may result in higher EET at the interface biofilm/electrode. Improvements in film resistivity can be achieved by higher temperatures during deposition, which would be possible with certain kinds of glass or transparent crystal materials i.e. sapphire. However, the use of plastic substrates places an upper limit on deposition temperature. Since thicker films exhibit a decrease in resistivity, and the beginnings of a crystal structure. It may be possible to produce more conductive films at greater thicknesses.

References:

Allende, A, and Francisco Artés. “UV-C radiation as a novel technique for keeping quality of fresh processed "lollo rosso" lettuce.” *Food Research International* 36, no. 7 (2003): 739-746.

Amoruso, S, R Bruzzese, N Spinelli, and R Velotta. “Characterisation of Laser Ablation Plasmas.” *Journal of OHysics B: Atomic Molecular and Optical PHysics* 32 (1999): 131-172.

Artés, Francisco, Perla Gómez, Encarna Aguayo, Victor Escalona, and Francisco Artés-Hernandez. “Sustainable Sanitation Techniques for keeping quality and safety of fresh-cut plant commodities.” *Postharvest Biology and Technology* 51, no. 3 (2009): 287-296.

Avci, Ercan. “An electrochemical Study of the Deposition of Copper and Silver on Thymine Modifed Au (111).” PhD Thesis, Biology, Chemistry and Pharmacy, Freie Universitat Berlin, Berlin, 2007, 30-32.

Baba, T, et al. “Construction of Escherichia coli K-12 in-frame, single-gene knockout mutants: the Keio collection.” *Molecular Systems Biology*, 2006: E1 - E11.

Bancroft, Eric E, James S Sidwell, and Henry N Blount. “Derivative Linear Sweep and Derivative Cyclic Voltabsorptometry.” *Analytical Chemistry* 53 (1981): 1390-1394.

Bellan, Paul M. *Fundamentals of Plasma Physics.* Cambridge University Press, 2006.

Beuchet, L R. “Survival of entero hemorragic escherichia coli O157:H7 in bovine feces applied to lettuce and the effectiveness of chlorinated water as a disinfectant.” *Journal of Food Protection* 62, no. 8 (August 1999): 845-849.

Borloo, Jimmy, et al. “A Kinetic approach to the dependence of dissimilartory metal reduction by Shawanella oneidensis MR-1 on the outer membrane cytochromes c OmcA and OmcB.” *FEBS* 274, no. 14 (2007): 3728-3739.

Boyd, TJ M, and JJ Sanderson. *The Physics of Plasmas.* Cambridge University Press, 2003.

Burm, K.T.A.L. “Caclulation of the Townsend coefficients and the Paschen curve coefficients.” *Plasma Physics* 47, no. 3 (2007): 177-182.

Carlin, F, and C Nguyen-the. “Proceedings of the International conference on fresh-cut produce.” Chipping Camden: Campden and Chorleywood Food Research Association, 1999.

Chaudhuri, S K, and D R Lovley. “Electricity generation by direct oxidation of glucose in mediatorless microbial fuel cells.” *National Biotechnology* 21 (2003): 1229-1232.

Chen, Francis F. *Introduction to Plasma Physics and Controlled Fusion.* New York: Plenum Press, 1984.

Cheruthazhekatt, S, M Cernak, P Slavicek, and et al. “Gas Plasmas and plasma modified materials in medicine.” *Journal of Applied Biomedicicne* 8, no. 2 (June 2010): 55-56.

Chiang, M H, J Y Wu, Y H Li, J S Wu, S H Chen, and C L Chang. “Inactivation of E. coli and B. subtilis by a parallel plate dielectric barrier discharge jet.” *Surface & Coatings Technology*, no. 204 (2010): 3729-3737.

Chiper, A S, A V Nastuta, G B Rusu, and G Popa. “On Surface Elementary processes and polymer surface surface modifications induced by double pulsed dielecric barrier discharge.” *Nuclear Instruments and Methods in Physics Research B* 267 (2009): 313-316.

Chiper, A S, W Chen, O Mejiholm, P Dalgaard, and E Stamate. “Atmospheric pressure plasma produced inside a closed plackage by a dielectric barrier discharge in Ar/ CO2 for bacterial inactivation of biological samples.” *Plasma Souces Science and technology* 20 (2011): 025008.

Chiper, Alina S, Anita Viorel, Catalin Agheorghiesei, Valentin Pohoat, Maria Anit, and Gheorge Popa. “Diagnostics of a DBD Plasma in He/Air and He/N2 Gas Mixtures.” *Plasma Process Polymers* 1 (2004): 57-62.

Chrisey, Douglas B, and G K Hubler. *Pulsed Laser Deposition of Thin Films.* 1994.

Christman, M F, G Storz, and B N Ames. “OxyR, a positive regulator of hydrogen peroxide-inducible genes in Escherichia coli and Salmonella typhimurium, is homologous to a family of bacterial regulatory proteins.” *Proceedings of the National Academy of Sciences of the United States of America* 86, no. 10 (1989): 3484-3488.

Christoulakis, S, M Suchea, E Koudoumas, M Katharakis, N Katsarakis, and G Kiriakidis. “Thickness Influence on Surface Morphology and ozone sensing properties of nanostructured ZnO transparent thin films grown by PLD.” *Applied Surface Science*, no. 252 (2006): 5351-5354.

Connolly, Jack, Anand Jain, Gabriele Pastorella, Satheesh Krishnamurthy, Jean-Paul Mosnier, and Enrico Marsili. “Zinc Oxide and indium tin oxide thin films for the growth and characterisations of Shewanella lohica PV-4 electroactive biofilms.” *Virulence* 1, no. 2 (2011): 479-482.

Crawford, G P. *Wiley Series in Display Technology - Flexible Flat Panel Display Technology.* Edited by G P Crawford. Chichester: John Wiley & Sons, 2005.

Crookes, William. “On Radiant Matter.” *A Lecture Delivered to the British Association for the Advancement of Science*, August 1879: 28.

Cvelbar, U, M Mozetic, N Hauptman, and N Klanjsek-Gunde. “Degradation of Staphylococcus Aureus bacteria by Neutral Oxygen Atoms.” *Journal of Applied Physics N* 106 (2009): 103303-1 - 103303-5.

Davis, F, and S P. J Higson. “Biofuel Cells - Recent Advances and Applications.” *Biosensors and Bioelectronics* 22 (2007): 1224-1235.

de Geyter, N, R Morent, and C Lays. “Surface characterization of plasma-modified polyehtylene by contact angle experiments and ATR-FTIR spectroscopy.” *Surface and Interface Analysis* 40, no. 3-4 (2007): 608-612.

Donovan, Conrad, Alim Dewan, Deukhyoun Heo, and Haluk Beyenal. “Batteryless, wireless sensor powered by a sediment microbial fuel cell.” *Environ. Sci. Technol.* 42 (2008): 8591-8596.

Du, Zhuwei, Haoran Li, and Tingyue Gu. “A state of the art review of microbial fuel cells: A promising technology for wastewater treatment and bioenergy.” *Biotechnology advances* 25 (2007): 464-482.

Duley, W W. *CO2 Lasers: Effects and Applications.* New York: Academic Press, 1976.

Eliasson, Baldur, Ulrich Kogelschatz, and M Hirth. “Ozone synthesis from oxygen in dielectric barrier discharges.” *Journal of PHysics D: Applied Physics* 20 (1987): 1421.

Falkenstein, Zoran, and John J Coogan. “Microdischarge Behaviour in the Silent Discharge of Nitrogen - Oxygen and Water - Air mixtures.” *Journal of PHysics D: Applied Physics* 30 (1997): 817-825.

Flores-Fuentes, A, et al. “Electrical Model of an Atmospheric Pressure Dielectric Barrier Discharge Cell .” *IEEE Transactions on Plasma Science* 37 (2009): 128-134.

Fridman, Gregory, Gary Friedman, Alexander Gutsol, Anatoly B Shekter, Victor N Vasilets, and Alexander Fridman. “Applied Plasma Medicine.” *Plasma Processes and Polymers* 5, no. 6 (2008): 503-533.

Geissib, Franz J. “Advances in atomic force microscopy.” *Reviews of Modern PHysics*, 2003: 1-86.

Geuset, G E, H M Marcos, and L G Van Uitert. “Laser Oscillations in Nd Doped Yttrium, Yttrium Gallium and Gadolinium Garnets.” *Applied PHysics Letters* 4, no. 10 (May 1964): 182-184.

Goldston, R J, and P H Rutherford. *Introduction to Plasma Physics.* IOP Publishing, 1995.

Goodfellow.com. n.d. (accessed September 20, 2012).

Grasso, E M, R M Uribe-Rendon, and K Lee. “Inactivation of Escherichia coli inoculated onto fresh-cut chopped cabbage using electron beam processing.” *Journal of Food Protection* 74 (2011): 115.

Greenberg, J T, P Monach, J H Chou, P D Josephy, and B Demple. “Positive control of a global antioxidant defense regulon activated by superoxide-generating agents in Escherichia coli.” *Proceedings of the National Academy of Science of the United States of America* 87, no. 16 (1990): 6181-.

Gulec, A, L Okuz, and N Hershkowitz. “Optical studies of dielectric barrier plasma aerodynamic actuators.” *Plasma Sources Science and Technology* 20 (2011): 045019.

Hegenbart, Scott. “Ozone - Another Layer of Food Safety.” *Food Product Design* 76 (2002).

Holzman, D C. “Microbe Power.” *Environmental Health Perpective*, no. 113 (2005): 754-757.

Horcas, I, R Fernández, J M Gómez-Rodríguez, J Colchero, J Goméz-Herrero, and A M Baro. “WSXM: A software for scanning probe microscopy and a tool for nanotechnology.” *Review of Scientific Instruments* 78, no. 1 (2007): 013705.

Huba, J D. *NRL Plasma Formulary.* Washington DC 20375: The Office Of Naval Research, 2011.

Issa-Zacharia, Abdulsudi, Yoshinori Kamitani, Nami Miwa, Happiness Muhimbula, and Koichi Iwasaki. “Application of slightly acidic electrolyzed water as a potential non-thermal food sanitizer for decontamination of fresh ready-to-eat vegetables and sprouts.” *Food Control* 22, no. 3-4 (2011): 601-607.

Izumi, Hirokazu, Tsuguo Ishihara, Hideki Yoshioka, and Muneyuki Motoyama. “Electrical properties of crystalline ITO films prepared at room temperature by pulsed laser deposition on plastic substrates.” *Thin Solid Films* 411, no. 1 (2002).

Jain, Anand, et al. “Electron transfer mechanism in shewanella lohica PV-4 biofilms formed at graphite electrode.” *Bioelectrochemistry (in press)*, 2012.

Jain, Anand, Giulio Gazzola, Aurora Panzera, Michele Zanoni, and Enrico Marsili. “Visible spectroelectrochemical characterisation of geobacter sulfurreducens biofilms on optically transparent indium tin oxide electrode." *Electrochimica Acta* 56 (2011): 10776-10785.

Keener, Kevin M, et al. "Decontamination of Bacillus subtilis spores in a sealed package using a non-thermal plasma system." *NATO Advanced Research Workshop: Plasma for Bio-decontamination, Medicine and Food security.* Demanovska dolina, Slovakia, 2011.

Khadre, M A, A E Yousef, and J -G Kim. "Microbiological Aspects of Ozone Applications: A Review." *Journal of Food Science* 66, no. 9 (2006): 1242-1253.

Kim, Doyoung, Hyemin Kang, Jae-Min Kim, and Hyoungjun Kim. "The properties of plasma-enhanced atomic layer deposition (ALD) ZnO thin films and comparison with thermal ALD." *Applied Surface Science* 257, no. 8 (February 2011): 3776-3779.

Kim, H J, M S Hyun, I S Chang, and B H Kim. "A microbial fuel cell type lactate biosensor using a metal-reducing becterium, Shewanella putrefaciencs." *Journal of Microbiology Biotechnology*, 1999: 365-367.

Kim, H, J S Horwitz, G P Kushto, Z H Kafafi, and D B Chrisey. "Indium Tin Oxide thin films grown on flexible plastic substrates by pulsed laser deposition for organic light emitting diodes." *Applied Physics Letters* 79, no. 3 (2001): 284-287.

Kim, Jong-Pil, Sang-A Lee, Jong Seong Bae, Sunk-Kyun Park, Ung-Chan Choi, and Chae-Ryong Cho. "Electric Properties and Surface Characterisation of transparent Al-doped ZnO thin films prepared by pulsed laser deposition." *Thin Solid Films* 516 (2008): 5223-5226.

Kim, Se Jin. *Pulsed Laser Deposited Metal Oxide Thin Films Mediated Controlled Adsorption of Proteins.* PhD Thesis, University Of Florida, 2008.

Klockow, Paul A, and Kevin M Keener. "Safety and quality assessment of packaged spinach treated with a novel ozone-generation system." *LWT-Food Science and technology* 42, no. 6 (2009): 1047-1053.

Koechner, Walter, and Michael Bass. *Solid State Lasers: A Graduate Text.* New York: Springer, 2003.

Kogelschatz, Ulrich. "Dielectric Barrier Discharges - Principles and Applications." *J. Phys IV France*, 1997: C4.47 - C4.67.

Kogelschatz, Ulrich. "Dielectric Barrier Discharges: Their History, Discharge Physics and Industrial Applications." *Plasma Chemistry and Plasma Processing* 23, no. 1 (March 2003): 1-46.

—. “Fundamentals and Applications of Dielectric Barrier Discharge.” *7th International Symposium on High Pressure, Low Temperature Plasma Chemistry.* Greifswald, Germany, 2000.

Kogelschatz, Ulrich, and Baldur Eliasson. “From ozone generators to flat television screens: the history and future potential fo dielectric barrier discharges.” *Pure Applied Chemistry* 71, no. 10 (1999): 1819-1828.

Kogelschatz, Ulrich, and Baldur Eliasson. “Ozone Generation from Oxygen and Air: Discharge Physics and Reaction Mechanisms.” *Ozone Science and Engineering* 10 (1988): 367-378.

Kong, Michael. “About Plasmas: Destroying Biological Hazards.” *Plasma Coalition.* 2003. http://www.plasmacoalition.org/plasma_writeups/destroying-biohazards.pdf (accessed August 2010).

Kong, Michael G, et al. “Plasma Medicine: An Introductory Review.” *New Journal of Physics* 11 (2009).

Laroussi, Mounir. “Nonthermal decontamination of biological media by atmospheric-pressure plasmas: review, analysis, and prospects.” *IEEE Transactions on Plasma Science* 30, no. 4 (2002): 1409-1415.

Laroussi, Mounir, Claire Tendero, Xinpei Lu, Sudhakar Alla, and Wayne L Hynes. “Inactivation of Bacteria by the Plasma Pencil.” *Plasma Processes and Polymers* 3 (2006): 470-473.

Laroussi, Mounir, D A Mendis, and M Rosenberg. “Plasma Interaction with Microbes.” *New Journal of Physics* 5 (2003).

Laux, Christophe O, and Charles H Kruger. “Arrays of Radiative Transition Probabilities for the N2 First and Second Positive, NO Beta and Gamma, N2+ First Negative and O2 Schuman-Runge Band systems.” *J. Quat. Spectrosc. Radiat. Transfer.* 48, no. 1 (1992): 9-24.

Laux, Christophe O, T G Spence, C H Kruger, and R N Zare. “Optical Diagnostics of atmospheric pressure air plasmas.” *Plasma Sources Cience and TEchnology* 12 (2003): 125-138.

Laux, Christophe. “Radiation and Nonequilibreum Collisional-Radiative Models.” *VKI Special Course on Physico-Chemical Models for High Enthalpy and Plasma Flows Modeling June 4-7.* 2002. 1-55.

Lee, Yong-Hyuk, Chang-Heon Yi, Min-Jae Chung, and Geun-Yon Yeom. “Characteristics of He/O2 atmospheric pressure glow discharge and its dry etching properties of organic materials.” *Surface and Coatings Technology* 146-147 (2001): 474-479.

Leipold, F, N Schultz-Jensen, Y Kus a no, and T Jacobsen. “Decontamination of objects in a sealed container by means of atmospheric pressure plasmas.” *Food Control* 22, no. 8 (August 2011): 1296-1301.

Li, Y, R E Brackett, J Chen, and L R Beuchat. “Survival andgrowth of escherichia coli O157:H7 inoculated onto cut lettuce before or aftr heatingin chlorinated water followed vy storage at 5 or 15 degrees celsius.” *Journal of Food Protection* 64, no. 3 (2001): 305-309.

Liu, Yaodong, and Jianshe Lian. “Optical and electrical properties of aluminium-doped ZnO thin films grown by pulsed laser deposition.” *Applied Surface Science* 253 (2007): 3727-3730.

Liu, Yaodong, Lei Zhao, and Jianshe Lian. “Al-doped ZnO films by pulsed laser deposition at room temperature.” *Vacuum* 81 (2006): 18-21.

Loewen, Peter C, Bei Hu, Jeanna Strutinski, and Richard Sparling. “Regulation in the rpoS regulon of Escherichia coli.” *Canadian Journal of Microbiology* 44, no. 8 (1998): 707-717.

Logan, Bruce E. *Microbial Fuel Cells.* Hoboken, NJ: Wiley, 2008.

Lorenzo-Lorenzo, M J, M E Ares-Mazas, I Villacorta-Martinez de Maturana, and D Duran-Oreiro. “Effect of Ultraviolet disinfection of Drinking Water on the Viability of Cryptosporidium parvun Oocysts.” *The Journal of Parasitology* 79, no. 1 (1993): 67-70.

Lu, X, F Leipold, and Mounir Laroussi. “Optical and electrical diagnostics of a non-equilibrium air plasma.” *J Phys D: Appl Phys* 36 (2003): 2662-2666.

Luo, Siqi, C Mark Denning, and John E Scharer. “Laser RF Creation and Diagnostics of Seeded atmospheric pressure air and nitrogen plasmas.” *Journal of Applied Physics* 104 (2008): 013301.

Manley, T C. “The Electric Characteristics of the Ozonator Discharge.” *Transactions of the Electrochemical Society.* New York, 1943. 83-97.

Marsili, Enrico, Janet R Rollefson, Daniel B Baron, Raymond M Hozalski, and Daniel R Bond. “Micobial Biofilm Voltammetry: Direct Electrochemical Characterisation of Catalytic

Electrode-Attatched Biofilms." *Applied and Environmental Microbiology* 74, no. 23 (2008): -7329-7337.

Mass, J, P Bhattacharya, and R S Katiyar. "Effect of high substrate temperature on Al-doped ZnO thin films grown by pulsed laser deposition." *Materials Science and Engineering* B103 (2003): 9-15.

Materials Research Laboratory at University of California, Santa Barbara. n.d. http://www.mrl.ucsb.edu/mrl/centralfacilities/xray/xray-basics/index.html#x0 (accessed May 22, 2012).

Mehta, V K. *Principles of Electronics 7th edition.* S Chand and Co Ltd, 2005.

Mendis, D A, M Rosenberg, and F Azam. "A note on the possible electrostatic disruption of bacteria." *IEEE Transactions on Plasma Science* 28, no. 4 (2000): 1304-1306.

Menzer, R E, and J O Nelson. *Casserett and Doull's Toxicology: The Basic Science of Poisons, 6th Edition.* Columbus, Ohio: McGraw-Hill, 2001.

Moisan, M, Barbeau, J, Moreau, S, Pelletier, J, Tabrizian, M, Yahia, L. "Low-temperature sterilization using gas plasmas: a review of the experiments and an analysis of the inactivation mechanisms." *International Journal of Pharmaceutics* 226, no. 1-2 (2001): 1-21.

Moisan, Michel, Jean Barbeau, Marie Charlotte Crevier, Jacques Pelletier, Nicolas Philip, and Bachir Saoudi. "Plasma Sterilization: Methods and Mechanisms." *Pure Applied Chemistry* 74, no. 3 (2002): 349-358.

Moon, Se Youn, and W Choe. "A Comparative Study of Rotational Temperatures using Diatomic OH, O2 and N2 molecular spectra emitted from atmospheric plasmas." *Specrochemica Acta* 58 (2003): 249-257.

Narasimhan, K L, S P Pai, V R Palkar, and R Pinto. "High Quality zinc oxide films by pulsed laser deposition." *Thin Solid Films* 295 (1997): 104-106.

Nersisyan, G, and W G Graham. "Characterisation of a dielectric barrier discharge operating in an open ractor with flowing helium." *Plasma Sources Science and Technology* 13 (2004): 582.

Ngom, B D, et al. "Structural and Optical Properties of nano-structured tungsten doped ZnO thin films grown by pulsed laser deposition." *Applied Surface Science*, no. 255 (2009): 4153-4158.

Nomura, Kenji, Hiromichi Ohta, Akihiro Takagi, toshio Kamiya, Masahiro Hirano, and Hideo Hosono. “Room-temperature fabrication of transparent flexible thin-film transistors using amorphous oxide semicondictors.” *Nature* 432 (November 2004): 488-492.

O 'Connor, Niall. “Electrical, Optical and Acoustic Diagnostics of Atmospheric Pressure Gas Discharges.” PhD thesis Dublin City University, 2011.

O Haire, Richard. “Growth by Pulsed Laser Deposition and Characterisation of Zinc Oxide Thin Films and Nanostructures.” PhD Thesis Dublin City University, 2009.

Palmer, A Jay. “A Physical Model on the Initiation of Atmospheric Pressure Glow Discharges.” *Applied Physics Letters* 25 (1974): 138.

Papadopoulou, Evie L, Alexios Pagkozidis, Marios Barberolgou, Costas Fotakis, and Emmanuel Stratakis. “Electrowetting properties of ZnO and TiO2 Nanostructured Thin Films.” *J. Phys. Chem. C*, no. 114 (2010): 10249-10253.

Papadopoulou, Evie L, et al. “Reversible Photoinduced Wettability Transition of Hierarchical ZnO Structures.” *J. Phys. Chem C*, no. 113 (2009): 2891-2895.

Park, Sang Moo, Tomoaki Ikegami, and enji Ebihara. “Investigation of Transparent Conductive Oxide Al-Doped ZnO Films Produced by Pulsed Laser Deposition.” *Japanese Journal of Applied Physics* 44, no. 11 (2005): 8027-8031.

Pearse, R W.B., and A G Gaydon. *The Identification of Molecular Spectra.* Chapman and Hall, 1976.

Perni, S, et al. “Probing Bacteriecidal mechanisms induced by cold atmospheric plasmas with escherichia coli mutants.” *Applied PHysics Letters* 90, no. 7 (2007): 073902 - 073902-3.

Perutz, M F. *University of Cambridge Department of Physics - Sir Lawrence Bragg.* 2012. http://www.phy.cam.ac.uk/history/years/bragg.php (accessed May 23, 2012).

Poiata, Antoniea, Iuliana Motrescu, A Nastuta, D E Creanga, and G Popa. “Microorganism response to atmospheric pressure helium plasma DBD treatment.” *Journal of Electrostatics* 68, no. 2 (2010): 128-131.

Pomposiello, Pablo J, and Bruce Demple. “Redox-operated genetic switches: the SoxR and OxyR transcription factors.” *Trends in Biotechnology* 19, no. 3 (2001): 109-115.

Potter, M C. “Electrical Effects Accompanying the decomposition of Organic Compunds.” *Proceedings of the Royal Society of London, Series B, Containing Papers of a Biological Character.* 1911. 260-276.

Rabaey, K, G Lissens, S Siciliano, and W Verstraete. "A Microbial fuell cell capable of converting glucose to electricity at high rate and efficiency." *Biotechonology Letters* 25 (2003): 1531-1535.

Ragni, Luigi, et al. "Non-thermal atmospheric gas plasma device for surface decontamination of shell eggs." *Journal of Food Engineering* 100, no. 1 (2010): 125-132.

Ren, C S, K Wang, Q Y Nie, D Z Wang, and S H Guo. "Surface modification of PE film by DBD plasma in air." *Applied Surface Science* 255 (2008): 3421-3425.

Richardson, S D, A D Thruston, T V Caughran, T W Collette, K S Patterson, and B W Lykins. "Chemical by-products of chlorine and alternative disinfectants." *Food Technology* 52, no. 4 (1998): 58-61.

Rico, D, A B Martin-Diana, J M Barat, and C Barry_Ryan. "Extending and measuring the quality of fresh-cut fruit and vegetables: A review." *Trends in Food Science and Technology* 18, no. 7 (2007): 373-386.

Ries, Delphine, Eric Robert, Sébasien Dozias, Marc Vandamme, Vanessa Sarron, and Jean Michel Pouvesle. "Characterisation of Plasma Sources for Biomedical Applications." *International Plasma Chemistry Society.* Philadelphia, 2011.

Roth, J R. *Industrial Plasma Engineering.* Vol. 1. Bristol: Institute of Physics Press, 1995.

Salinero, O, J J Garrido, F Wandosell, F Nigro, A Ippolito, and G Lima. "Use of UV-C light to reduce Botrytis storage rot of table grapes." *Postharvest Biology and Technology* 13, no. 3 (June 1998): 171-181.

Schwabedissen, A, P Lacinski, X Chen, and J Engemann. "PlasmaLabel - A New Method to Disinfect Goods inside a Closed Package using Dielectric Barrier Discharge." *Contributions to Plasma Physics* 47, no. 7 (2007): 551-558.

Singh, A V, and R M Mehra. "Highly conductive and transparent aluminium doped zinc oxide thin films prepared by pulsed laser deposition in oxygen ambient." *Journal of Applied Physics* 90, no. 11 (December 2001): 5661-5666.

Smirnov, Boris M. *Physics of Ionised Gases.* 2001.

Stoffels, Eva, Yukinori Sakiyama, and David B Graves. "Cold Atmospheric Plasmas: Charged Species and their Interactions with Cells and Tissues." *IEEE Transactions on Plasma Science* 36, no. 4 (2008): 1441-1458.

Valdivia-Barrientos, R, J Pacheco-Sotelo, M Pacheco-Pacheoc-, J S Benitez-Read, and R Lopez-Callejas. "Analysis and Electrical Modelling of a Cylindrical DBD configuration at different operating frequencies,." *Plasma Sources Science and Technology* 15 (2006): 237-245.

Van der Pauw, Leo J. "A Method of Measureing Specific Resistivity and Hall Effect of Discs of Arbitrary Shape." *Philips Research Reports* 13, no. 1 (1958): 1-9.

Villanueva, Yolanda Y, Da-Ren Liu, and Pei Tzu Cheng. "Pulsed Laser Deposition of Zinc Oxide." *Thin Solid FIlms* 501 (2006): 366-369.

Wagner, H E, R Brandenburg, K V Kozlov, A Sonnenfeld, P Michel, and J F Behnke. "The Barrier Discharge: Basic PRoperties and Applications to Surface Treatment." *Vacuum* 71 (2003): 417-436.

Walsh, J L, D X Liu, F Iza, M Z Rong, and Michael G Kong. "Contrasting characteristics of sub-microsecond pulsed atmospheric air and atmospheric pressure helium-oxygen glow discharges." *Journal of PHysics D: Applied Physics* 43 (2010): 032001.

Wang, Kun, Jian Li, Ren Chunsheng, Wang Dezhen, and Wang Younian. "Surface Modification o fpolyehtylene (PE) films Using Dielectric Barrier Discharge Plasma at Atmospheric Pressure." *Plasma Science and Technology* 10, no. 4 (August 2008): 433-439.

Weltmann, Kalus D, Ekhard Kindel, Thomas von Woedtke, Marcel Haenel, Manfred Stieber, and Ronny Brandenburg. "Atmospheric Pressure Plasma Sources: Prospective tools for Plasma Medicine." *Pure and Applied Chemistry* 82, no. 6 (June 2010): 1223-1237.

Wikipedia - AFM Cantilever image. 2009. http://en.wikipedia.org/wiki/File:AFM_%28used%29_cantilever_in_Scanning_Electron_Microscope,_magnification_1000x.JPG.

Xie, Y, W Zhai, J Chang, and C Ding. "Preparation and in vitro evaluation of plasma-sprayed Mg2 Si O4 coating on Titanium alloy." *Acta Biomateriala* 5, no. 6 (July 2009): 1221-2337.

Yamada, Akira, Baosheng Sang, and Makoto Konagi. "Atomic Layer Deposition of ZnO transparent conducting oxides." *Applied Surface Science* 112 (March 1997): 216-222.

Yehia, A, and A Mizuno. "Calculation of the electrical power dissipated in silent discharge reactors." *Journal of Applied Physics* 98 (2005): 043305.

Yooq, Hyuk Sang, Taek Gyong Kim, and Tae Gwan Park. "Surface-functionalised electrospun nanofibres for tissue engineering and drug delivery." *Advanced Drug Delivery Reviews* 61 (2009): 1033-1042.

Zhang, Cheng, Tao Shai, Yang Yu, Ping Yan, and Yuanxiang Zhou. “Comparison of Experiment and Simulation on dielectric barrier discharge driven by 50 Hz power in atmospheric air.” *Journal of Electrostatics* 68 (2010): 445-452.

Zhang, S, and J M Farber. “The effects of various disinfectants against listeria monocytogenes on fresh cut vegetables.” *Food Microbiology* 13, no. 4 (1996): 311-321.

Zhang, Tian, Chengzheng Cui, Shengli Chen, Hanxi Yang, and Ping Shen. “Thedirect electrocatalysis of Escherichia coli through electroactivated excretion in microbial fuel cell.” *Electrochemistry Communications* 10, no. 2 (2008): 293-297.